

DISS. ETH NO. 25766

Magnetic Resonance Intravoxel Incoherent Motion Mapping in Heart and Brain

A thesis submitted to attain the degree of
DOCTOR OF SCIENCES of ETH Zurich
(Dr. sc. ETH)

presented by

Georg Ralph Spinner
MSc ETH Physics
ETH Zurich, Switzerland

born on 30.11.1986
citizen of Germany

Accepted on the recommendation of
Examiner: Prof. Dr. Sebastian Kozerke
Co-examiner: Prof. Dr. Gustav Strijkers

2019

Abstract

Cardiovascular diseases (CVDs) are the leading cause of death worldwide. Frequent manifestations of CVDs are ischemic heart disease, myocardial infarction and stroke. In ischemic heart disease, tissue viability of the heart muscle is compromised in response to reduced perfusion. Prolonged ischemia may lead to myocardial infarction and subsequent heart failure. Ischemic strokes, on the other hand, are the consequence of reduced perfusion in the brain. Strokes are likewise a major cause of death and disability.

Beyond myocardial infarction and stroke, there is wide range of diseases which are associated with changes in tissue perfusion. For example, in cancerous tissue, perfusion is upregulated and hence perfusion measurements play an important role in determining malignancy, risk stratification and treatment control. Another field of application of perfusion measurements concerns the vascular subtype of dementia, a disease of increasing prevalence in the aging population.

Magnetic resonance imaging (MRI) is the key non-invasive, radiation-free modality to diagnose and monitor a wide range of pathologies. Dedicated pulse sequences have been developed for cardiac magnetic resonance (CMR) perfusion measurements including dynamic contrast enhancement (DCE) imaging. The DCE method, however, requires the administration of an exogenous Gadolinium-based contrast agent. In patients, especially in individuals with renal insufficiency, adverse events such as nephrogenic systemic fibrosis (NSF) may occur upon contrast agent injection. Moreover, recent findings indicate cases of long-term deposition of Gadolinium contrast agents in the central nervous system. Therefore, alternative, contrast agent free methods to map perfusion are highly desired.

The intravoxel incoherent motion (IVIM) model describes the modulation of the MRI signal in the presence of blood flow while diffusion encoding gradients are applied. The IVIM approach can be considered an extension of diffusion weighted imaging (DWI) or diffusion tensor imaging (DTI), where, instead of a single diffusion encoding point, multiple encodings per spatial axis are acquired. Accordingly, the signal modulation due to perfusion and water self-diffusion can be disentangled.

The objectives of the present thesis are to develop, assess and validate tissue perfusion encoding in the heart and brain using the IVIM principle. To this end, several challenges are addressed ranging from perfusion signal modeling, to

accelerated image acquisition and subsequent reconstruction to advanced data post-processing strategies.

The first project of this thesis proposes an improved data acquisition strategy for IVIM imaging in the brain through data undersampling. Since IVIM in the brain requires sufficiently high coverage and resolution, long readouts result which in turn produce image artifacts. To overcome this limitation, an undersampled sheared grid data acquisition scheme was implemented with subsequent constrained image reconstruction. It is demonstrated, using retro- and prospectively undersampled data that the proposed method allows for artifact-free IVIM mapping up to an undersampling factor of six. Using data acquired on a clinical MRI system, a clear advantage of this novel approach over previous parallel imaging methods is shown.

Given the data, IVIM parameter estimation suffers from a low signal-to-noise ratio (SNR) and the inherent non-linearity of the data fitting problem. Consequently, IVIM parameter maps may exhibit biases and uncertainty due to noise-dependent parameter estimation errors. In the second project of this thesis, this problem was addressed for IVIM imaging of the heart. To this end, the myocardial perfusion and diffusion properties were assumed to vary only moderately across the tissue of interest at a macroscopic scale. This prior knowledge was exploited in a hierarchical Bayesian approach to parameter estimation. A dedicated Markov chain Monte Carlo method was implemented and applied to simulated and in-vivo cardiac IVIM data. The method was found to compare favorably with standard least-squares (LSQ) methods both in simulations and in-vivo, improving accuracy, precision and reproducibility.

In the third project, the influence of capillary blood flow onto the MRI signal under the presence of diffusion encoding gradients was investigated. Extensive modeling of the specific capillary structure of the myocardium and dedicated pulse sequences was performed. In simulations, it could be shown that the standard IVIM model is indeed insufficient to accurately capture signal modulations due to perfusion influence. Moreover, it could be shown that gradient moment compensation reduces the perfusion sensitivity in spin-echo sequences. In contrast, stimulated echo acquisition provided sufficient perfusion sensitivity. These simulations were validated by ex-vivo data acquired in perfused porcine hearts.

To conclude, contrast agent free perfusion imaging using IVIM imaging has significantly been advanced in both the heart and brain with the present body of work. Several limitations and modeling issues have been addressed now fostering the utility of this perfusion imaging modality for clinical applications.

Zusammenfassung

Herz-Kreislauf-Erkrankungen sind weltweit die häufigste Todesursache. Häufige Manifestationen von Herz-Kreislauf-Erkrankungen sind die ischämische Herzkrankheit, Herzinfarkt und Schlaganfall. Bei einer ischämischen Herzkrankheit wird die Viabilität des Herzmuskels als Reaktion auf eine verringerte Durchblutung beeinträchtigt. Anhaltende Ischämie kann zu Herzinfarkt und -insuffizienz führen. Im Gegensatz dazu sind ischämische Schlaganfälle die Folge einer verminderten Durchblutung des Gehirns. Schlaganfälle sind ebenfalls eine der Hauptursachen für Tod und Invalidität.

Neben Herzinfarkt und Schlaganfall gibt es eine Vielzahl von Krankheiten, die mit Veränderungen der Gewebepfusion zusammenhängen. In Krebsgewebe zum Beispiel wird die Perfusion hochreguliert, sodass Perfusionsmessungen eine wichtige Rolle bei der Bestimmung von Malignität, Risikostratifizierung und Behandlungskontrolle spielen. Ein weiteres Anwendungsgebiet von Perfusionsmessungen betrifft den vaskulären Subtyp der Demenz, eine Krankheit mit zunehmender Prävalenz in der alternden Bevölkerung.

Die Magnetresonanztomographie (MRT) ist die wichtigste nichtinvasive, strahlungsfreie Modalität für die Diagnose und Überwachung einer Vielzahl von Pathologien. Dedizierte Pulssequenzen wurden für die Diagnose mittels der «cardiovascular magnetic resonance» (CMR) einschliesslich der «dynamic contrast enhancement» (DCE) Bildgebung entwickelt. Die DCE-Methode erfordert jedoch die Verabreichung eines exogenen Kontrastmittels auf Gadolinium-Basis. Bei Patienten, besonders solche mit Niereninsuffizienz können bei Kontrastmittelinjektion unerwünschte Nebenwirkungen wie nephrogene systemische Fibrose (NSF) auftreten. Neuere Erkenntnisse beschreiben zudem Fälle einer langfristigen Ablagerung von Gadolinium-Kontrastmitteln im Zentralnervensystem. Daher sind alternative, kontrastmittelfreie Verfahren zur Bestimmung der Perfusion gesucht.

Das «intravoxel incoherent motion» (IVIM) Modell beschreibt die Modulation des MRI-Signals verursacht durch Blutfluss unter dem Anlegen von Magnetfeldgradienten zur Diffusionsgewichtung. Der IVIM-Ansatz kann als Erweiterung von «diffusion weighted imaging» (DWI) oder des «diffusion tensor imaging» (DTI) Modells betrachtet werden, bei dem anstelle eines einzelnen diffusionskodierten Bildes mehrere Kodierungen pro Raumachse erfasst werden. Dementsprechend können die Signalmodulationen aufgrund von Perfusion und Selbstdiffusion von Wasser separat bestimmt werden.

Ziel der vorliegenden Arbeit ist es, Perfusionsgewichtung in Herz und Gehirn nach dem IVIM-Prinzip zu entwickeln, zu untersuchen und zu validieren. Zu diesem Zweck werden verschiedene Probleme bearbeitet, die von der Perfusionssignalmodellierung über die beschleunigte Bildgebung und zugehöriger -rekonstruktion bis hin zu fortgeschrittenen Methoden der Datenauswertung reichen.

Das erste Projekt dieser Arbeit behandelt eine verbesserte Datenakquisition für die IVIM-Bildgebung im Gehirn durch Datenunterabtastung. Da IVIM im Gehirn eine hohe Abdeckung und Auflösung erfordert, resultieren lange Sequenzen zur Bilderzeugung, die wiederum Bildartefakte produzieren. Um diese Einschränkung zu überwinden, wurde ein unterabgetastetes Datenerfassungsschema mit periodisch verschobenem Abtastmuster und nachfolgender regularisierter Bildrekonstruktion implementiert. Es wird anhand retrospektiv und prospektiv unterabgetasteter Daten gezeigt, dass das vorgeschlagene Verfahren artefaktfreie IVIM-Parameterkarten mit sechsfacher Unterabtastung ermöglicht. Anhand von Daten, die mit einem klinischen MRI-System erfasst wurden, wird ein klarer Fortschritt des neuen Ansatzes gegenüber bestehenden parallelen Bildgebungsverfahren demonstriert.

Die IVIM-Parameterschätzung wird durch ein niedriges Signal-Rausch-Verhältnis (SNR) und die inhärente Nichtlinearität des Regressionsproblems negativ beeinflusst. Folglich können IVIM-Parameterkarten aufgrund von Parameterschätzungsfehlern verursacht durch Rauschen systematische Abweichung und Streuung aufweisen. Im zweiten Projekt dieser Arbeit wurde dieses Problem für die IVIM-Bildgebung des Herzens bearbeitet. Zu diesem Zweck wurde die Annahme verwendet, dass die myokardialen Perfusions- und Diffusionseigenschaften in einem makroskopischen Massstab nur moderat im relevanten Gewebe variieren. Dieses Vorwissen wurde in einem hierarchischen Bayes'schen Ansatz zur Parameterschätzung genutzt. Ein spezielles Markov-Ketten-Monte-Carlo-Verfahren wurde implementiert und auf simulierte und in-vivo IVIM Herzdaten angewendet. Es wurde gezeigt, dass das Verfahren sowohl in Simulationen als auch in-vivo Vorteile gegenüber üblichen kleinste-Quadrate Verfahren besitzt, wodurch die Genauigkeit, Präzision und Reproduzierbarkeit verbessert werden.

Im dritten Projekt wurde der Einfluss des Kapillarblutflusses auf das MRI-Signal beim Anliegen von Diffusionsgewichtungsgradienten untersucht. Es wurde eine umfangreiche Modellierung der spezifischen Kapillarstruktur des Myokards und dedizierter Pulssequenzen durchgeführt. In Simulationen konnte gezeigt werden, dass das Standard-IVIM-Modell tatsächlich nicht ausreichend ist, um Signalmodulationen aufgrund von Perfusion richtig zu erfassen. Darüber hinaus konnte gezeigt werden, dass die Kompensation von höheren

Gradientenmomenten die Perfusionsempfindlichkeit in der Spin-Echo-Sequenz reduziert. Im Gegensatz dazu lieferten stimulierte Echo Sequenzen eine ausreichende Perfusionsempfindlichkeit. Diese Simulationen wurden durch ex-vivo-Daten validiert, die mit perfundierten Schweineherzen erhoben wurden.

Zusammenfassend lässt sich festhalten, dass die kontrastmittelfreie Perfusionsbildgebung unter Verwendung des IVIM-Modells sowohl im Herzen als auch im Gehirn mit der vorliegenden Arbeit signifikante Fortschritte gemacht hat. Es wurden verschiedene Limitationen und Probleme der Modellierung bearbeitet, um die Anwendbarkeit dieser Perfusionsbildgebungsmodalität für klinische Anwendungen zu erhöhen.

Contents

Abstract.....	3
Zusammenfassung.....	5
Chapter 1 Introduction	13
1.1 Motivation	14
1.2 Outline	15
1.3 Contribution of the thesis.....	15
Chapter 2 Principles of motion encoding	17
2.1 Diffusion imaging	17
2.1.1 Physical principles.....	17
2.1.2 Diffusion weighted imaging	18
2.1.3 Diffusion tensor imaging	21
2.2 Diffusion weighting sequences.....	23
2.2.1 Gradient moments	23
2.2.2 Stejskal-Tanner sequence	24
2.2.3 Stimulated echo acquisition mode	24
2.2.4 Motion compensation	25
2.3 Phase dispersion beyond diffusion	26
2.3.1 Intravoxel incoherent motion imaging	27
2.3.2 Phase gradients.....	29
2.4 General motion encoding	29
2.4.1 Displacement encoding	30
2.4.2 Velocity encoding	31
2.4.3 Diffusion spectrum imaging	32
2.4.4 Fourier velocity imaging	33
2.4.5 Implications for intravoxel incoherent motion imaging	33
Chapter 3 Principles of image encoding	34
3.1 Coil combination	35

3.1.1	Roemer combination	35
3.2	Parallel imaging.....	36
3.2.1	SENSE	36
3.3	Partial Fourier imaging	38
3.4	Compressed Sensing	40
3.5	Reconstruction of sheared grid k-space data	40
3.5.1	Sheared grid k-t undersampling	41
3.5.2	k-t BLAST & k-t SENSE	42
3.5.3	k-t PCA	43
3.5.4	Incoherent sampling and non-linear reconstruction	43
Chapter 4	Applied Bayesian statistics for MRI	44
4.1	Introduction to Bayesian statistics	44
4.1.1	Bayes' theorem	44
4.1.2	Data likelihood	45
4.1.3	Posterior distribution	45
4.1.4	Prior distribution	46
4.2	Bayesian inference	46
4.2.1	Analytic evaluation.....	47
4.2.2	Maximum a-posteriori point estimator	48
4.2.3	Markov chain Monte Carlo.....	49
4.2.4	Variational Bayes methods.....	50
4.3	Gaussian prior & k-t methods.....	50
4.4	Laplace prior & Compressed Sensing	51
4.5	Hierarchical priors and curve fitting.....	52
Chapter 5	Enhancing intravoxel incoherent motion parameter mapping in the brain using k-b PCA.....	54
5.1	Introduction	54
5.2	Methods.....	55
5.2.1	k-b PCA.....	55
5.2.2	CG-SENSE.....	58

5.2.3	In-vivo measurements.....	58
5.2.4	Data processing	59
5.2.5	Parameter mapping.....	60
5.2.6	Error estimation.....	61
5.3	Results.....	62
5.3.1	Reconstruction error	62
5.3.2	IVIM parameter estimation error	63
5.3.3	Prospectively undersampled data	65
5.3.4	IVIM parameter estimates	66
5.4	Discussion	67
5.5	Conclusion	69
5.6	Appendix.....	69
Chapter 6	Bayesian intravoxel incoherent motion parameter mapping in the human heart.....	71
6.1	Background.....	71
6.2	Theory.....	72
6.2.1	Intravoxel incoherent motion	72
6.2.2	Least-squares fitting	73
6.2.3	Bayesian shrinkage prior inference	73
6.3	Methods.....	74
6.3.1	Computer simulations	74
6.3.2	In-vivo measurements.....	74
6.3.3	Data post-processing.....	76
6.3.4	Reproducibility analysis.....	78
6.4	Results.....	78
6.4.1	Computer simulations	78
6.4.2	In-vivo measurements.....	79
6.5	Discussion	87
6.6	Conclusion	89
6.7	Appendix 1.....	90

6.7.1	Hierarchical Bayesian modelling	90
6.7.2	Markov chain Monte Carlo (MCMC) implementation	92
6.8	Appendix 2	92
6.8.1	Infarcted porcine heart.....	92
Chapter 7	On probing intravoxel incoherent motion in the heart – spin-echo versus stimulated-echo diffusion-weighted imaging.....	94
7.1	Introduction	94
7.2	Theory	96
7.2.1	IVIM model	96
7.2.2	Normalized phase distributions	97
7.2.3	Gaussian phase approximation	98
7.3	Methods.....	99
7.3.1	Cardiac capillary structure	99
7.3.2	Diffusion encoding gradients.....	100
7.3.3	Simulations	101
7.3.4	Ex-vivo data acquisition	102
7.3.5	Parameter mapping	103
7.4	Results	105
7.4.1	Simulations	105
7.4.2	Parameter mapping simulations	108
7.4.3	Ex-vivo data	109
7.5	Discussion	113
7.6	Conclusion.....	116
7.7	Appendix	116
Chapter 8	Summary.....	119
8.1	Discussion	119
8.2	Outlook.....	120
Bibliography.....		123
List of publications		140
Conference abstracts and proceedings		142

Acknowledgements 144
Curriculum Vitae 147

Chapter 1

Introduction

Cardiovascular diseases (CVD) are a major cause of death and disability worldwide (Mendis et al. 2011). A number of CVD pathologies are associated with changes in the vasculature leading to compromised tissue perfusion through various mechanisms (Ross 1986). More precisely, hemodynamic conditions are modified through structural and functional changes including vessel wall stiffening, the formation of atherosclerotic plaques and other vascular pathologies. The consequence of vascular remodeling can be a reduction of vessel lumen and hence reduced blood flow through the vessel at a given pressure gradient. Persistent blood flow reduction leads to reduced tissue perfusion and, if not timely treated, may progress to myocardial ischemic infarction. Resulting myocardial scar tissue following infarction consists of fibrous tissue, which is no longer physiologically functioning and shows decreased perfusion (Gibson et al. 1983; Altehoefer et al. 1992). Besides these localized perfusion defects, also diffuse changes of perfusion in the myocardium are known. Microvascular obstruction and reduced and/or delayed perfusion of the myocardium occur in hypertrophic cardiomyopathy and diabetes (Fang et al. 2004; Ismail et al. 2014) for example. In the brain, a stroke often involves reduced or suspended perfusion in the corresponding tissue territory. Early interventions after strokes require estimates of the volume of tissue-at-risk. Such tissue at risk of cell death can potentially be rescued by reestablishing perfusion using suitable interventions (Jauch et al. 2013).

Imaging modalities to assess tissue perfusion are of critical importance to diagnose CVD pathologies, monitor and optimize therapies. Nuclear imaging methods have been used early on for such purposes (Gibson et al. 1983; Altehoefer et al. 1992). Due to the high specificity of radioactive tracers used in nuclear imaging and the wealth of clinical data available, they are considered as a gold standard. Issues of nuclear imaging relate to the radioactive radiation the patient receives, limited availability of suitable tracers and limitations in spatiotemporal resolution.

Magnetic resonance imaging (MRI) allows the radiation-free assessment of tissue perfusion using Gadolinium-based contrast agents (Wilke et al. 1997; Al-Saadi et al. 2000; Wissmann et al. 2015) While the method offers high spatiotemporal resolution (Manka et al. 2012; Schmidt et al. 2014), it is restricted in patients with renal dysfunction (Schieda et al. 2018). Moreover,

recent reports also indicate a risk of Gadolinium deposition in brain tissue under certain circumstances (Gulani et al. 2017).

1.1 Motivation

Intravoxel incoherent motion (IVIM) is a non-invasive, contrast agent free MRI method that allows quantifying tissue perfusion surrogates in-vivo (Le Bihan et al. 1986; Le Bihan 2008). In IVIM, perfusion is encoded using diffusion weighting magnetic field gradients with varying strengths and directions. In the brain, several studies of IVIM have been presented including hypercapnia experiments (Federau et al. 2012), tumor investigation (Federau et al. 2017) and mapping of brain function (Federau et al. 2015). In contrast to IVIM in the brain, the application in the heart is considerably more challenging as it requires dedicated gradient shapes to compensate for myocardial strain effects (Frahm et al. 1985; von Deuster et al. 2016b; Stoeck et al. 2016). Using these dedicated motion-compensated diffusion sequences, IVIM can be applied to detect perfusion defects in hearts in an experimental setting (von Deuster et al. 2015). Several modifications and extensions to the IVIM model have been proposed, considering spatial anisotropy of perfusion (Karampinos et al. 2010; Mozumder et al. 2018) and a generalization of the IVIM model for perfusion regimes which violate the assumptions of the IVIM model (Wetscherek et al. 2015)..

Despite the availability of IVIM imaging on clinical scanners, three main limitations exist for IVIM parameter mapping in brain and heart. First, in brain IVIM imaging, long image readouts are necessary to cover the whole brain with an adequate resolution. The latter is required to reduce partial voluming in order to accurately capture small structures and tissue alterations. Long readouts cause prolonged data acquisition time and potential signal loss, especially in single-shot sequences. The longer the readout, the more artefact accumulation occurs due to magnetic field inhomogeneities at e.g. air-tissue interfaces. Second, IVIM parameter mapping requires the estimation of variables of a non-linear model. Since diffusion-weighted data are noisy, error-prone and biased parameter estimates of limited reproducibility may result. Third, in cardiac IVIM, the actual mechanisms of MRI signal modulation due to the unique capillary arrangement in the heart have not been fully understood in particular when using motion-compensated diffusion gradient waveforms.

The objectives of the present thesis are to develop, assess and validate tissue perfusion encoding in the heart and brain using the IVIM principle. To this end, several challenges are addressed ranging from perfusion signal modeling to accelerated data acquisition and advanced data post-processing strategies.

1.2 Outline

Chapter 2 introduces the basic principles of MR motion encoding, diffusion MRI and the IVIM model. Motion compensation strategies for cardiac diffusion-weighted MRI data acquisition are summarized.

In Chapter 3, MR image reconstruction principles are discussed and a review of parallel imaging and sheared-grid undersampling methods is provided.

Chapter 4 presents background on parameter estimation problems and MR image reconstruction from the perspective of Bayesian statistics.

Chapter 5 introduces an improved data acquisition strategy for IVIM imaging in the brain through sheared-grid data undersampling and subsequent constrained image reconstruction.

In Chapter 6, the application of a hierarchical Bayesian method for IVIM parameter estimation in healthy human hearts in-vivo is demonstrated.

Finally, Chapter 7 is concerned with a thorough investigation into the origin and nature of the IVIM effect in the heart for various diffusion weighting gradient shapes.

1.3 Contribution of the thesis

In this thesis, an undersampled Cartesian sheared-grid acquisition scheme with k-b PCA reconstruction is presented for brain IVIM imaging (Chapter 5). The proposed method allows for up to six-fold undersampling, well beyond the limits of parallel imaging which has been used so far. In terms of both image and IVIM parameter estimation error, the method compares favorably with existing parallel imaging applications.

To improve the error-prone and non-linear IVIM parameter estimation problem, a Bayesian approach for cardiac IVIM is presented and shown to outperform standard least-squares methods (Chapter 6). A two-level prior is used for regularization composed of a Gauss distribution of the log/logit transformed parameters of the voxels in the myocardium and a non-informative Jeffreys' prior. Numerical Monte Carlo simulations show the improved precision and accuracy for relevant parameter ranges. Resulting IVIM parameter estimates are found to be virtually free of outliers and the IVIM parameter reproducibility is improved.

To rationalize MRI signal modulation due to tissue perfusion in the heart, a novel modeling approach of the IVIM effect in the myocardium in response to various diffusion encoding gradient waveforms is proposed (Chapter 7). Specifically, the model considers the particular anisotropy and structure of the capillary bed in the left ventricle of the myocardium. Numerical simulations show that the resulting signal is more complex than predicted by the standard IVIM model. Investigation of ex-vivo data further elucidates and confirms the proposed modelling framework.

Chapter 2

Principles of motion encoding

2.1 Diffusion imaging

Diffusion imaging using MRI was described as early as 1965 by Stejskal and Tanner (Stejskal and Tanner 1965). Some ten years later, anisotropic diffusion was discovered (Cleveland et al. 1976) and a general framework of diffusion tensor MRI was described (Basser et al. 1994) about 30 years later. From then on, the field has flourished and diffusion MRI has become a ubiquitous MR method both in research as well as in clinical routine.

2.1.1 Physical principles

All biological tissues contain water and in many cases water is the major constituent with a predominant volume fraction. At temperatures above absolute zero, water self-diffusion is present due to thermal motion. Accordingly, water molecules are moving randomly and hence represent a “dynamic” equilibrium.

In general, Fick’s laws of diffusion govern diffusion processes. Fick’s first law states:

$$\mathbf{J}(\mathbf{x},t) = -D\nabla c(\mathbf{x},t) \quad (2.1)$$

and the second law:

$$\frac{\partial c(\mathbf{x},t)}{\partial t} = -\nabla \mathbf{J}(\mathbf{x},t) = \nabla \cdot (D\nabla c(\mathbf{x},t)) \quad (2.2)$$

with molecular flux density $\mathbf{J}(\mathbf{x},t)$ at the location \mathbf{x} and time t , diffusion coefficient D and molecular concentration $c(\mathbf{x},t)$.

Einstein has shown that in the case of water self-diffusion, the Brownian motion of the water molecules satisfy Equation (2.2) and the solution is a Normal distribution if N particles start from the origin at $t_0 = 0$ along n dimensions (Einstein 1905):

$$c(\mathbf{x},t) = \frac{N}{\sqrt{2\pi \cdot n2Dt}} \exp\left(-\frac{1}{2} \frac{\mathbf{x}^2}{n2Dt}\right) \quad (2.3)$$

The expected squared displacement is proportional to the time and diffusion constant. Hence, a typical diffusion radius can be defined:

$$r_{diff} = \sqrt{\langle (\mathbf{x}^2) \rangle} = \sqrt{n2DT} \quad (2.4)$$

Typical diffusion encoding times $t = T$ in MRI experiments are around 50 ms. Considering free-water, which has a diffusion coefficient of about $2.5 \cdot 10^{-3} \text{ mm}^2/\text{s}$ at room temperature, a diffusion displacement of about 27 μm results.

Deviations from Equation (2.4) occur in cases where diffusion is restricted, e.g. where cell membranes form boundaries to the diffusion process. Possible solutions have to account for those boundaries conditions and can therefore lead to different dependencies.

2.1.2 Diffusion weighted imaging

The diffusion process described above has an influence on the MRI signal and can therefore be measured. In the classical MRI description of water self-diffusion (Stejskal and Tanner 1965), the displacement of water molecules can be measured as follows: assume a short gradient pulse with duration δ after radio frequency (RF) excitation, the transverse magnetization accumulates phase according to

$$\varphi = \gamma \int_0^{\delta} G x_1 dt = \gamma G \delta x_1 \quad (2.5)$$

with diffusion weighting gradient magnitude G and x_1 the projection of the position \mathbf{x}_1 onto the gradient direction. After a waiting time $\Delta \gg \delta$, the water molecule has travelled to position \mathbf{x}_2 . If a second gradient with duration δ is applied, the phase difference becomes:

$$\varphi_2 - \varphi_1 = \gamma G \delta \cdot (x_2 - x_1) \quad (2.6)$$

Figure 2.1 illustrates two exemplary spins in such an experiment with total gradient/encoding duration T .

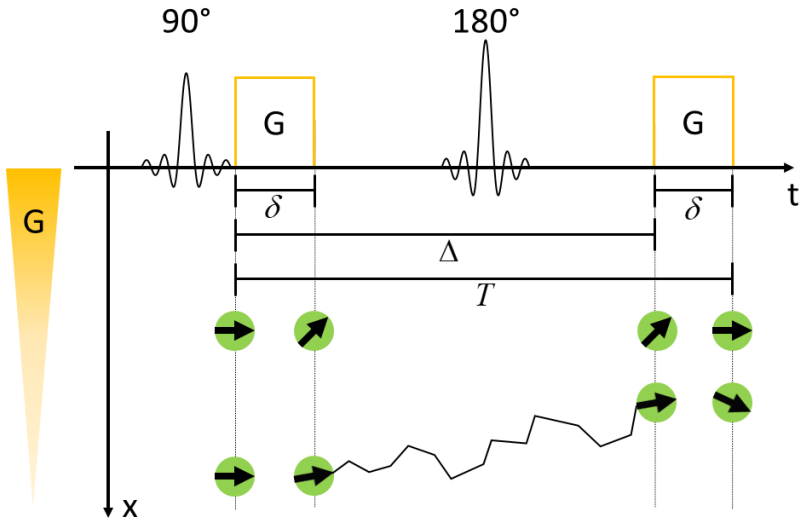


Figure 2.1: Illustration of phase evolution in a Stejskal-Tanner spin-echo diffusion experiment. The upper spin remains at a fixed position and hence acquires no net phase. In contrast, the lower spin undergoes a random walk, arrives at a different position when the second diffusion gradient is played out and hence acquires a net phase.

In general, MRI provides information on voxel level, i.e. the resulting signal is the average of the excited spins in a voxel. Imaging voxels are typically on the order of a few cubic millimeter and hence the number of water molecules contained within is several times the Avogadro constant. The total signal in a voxel is therefore the weighted average of all spins with their respective density and phase. If the spins undergo random walks, a net signal decay results due to phase dispersion. Consequently, the phases of the spins add up in the total signal and lead to a signal attenuation due to diffusion depending on the degree of dephasing, which can be stated as an expectation value:

$$F_D = \left| \langle \exp(i\varphi) \rangle \right| = \left| \int_{-\infty}^{\infty} \rho(\varphi) \exp(i\varphi) d\varphi \right| \quad (2.7)$$

Only one diffusion gradient strength and direction was used in the example above. Both can be varied however. The diffusion weighting strength is termed “b-value” (Le Bihan and Breton 1985) and is defined as follows:

$$b = \gamma^2 \int_0^T \left(\int_0^t \mathbf{G}(t') dt' \right)^2 dt \quad (2.8)$$

with total diffusion encoding time T .

The Bloch equations (Bloch 1946) which describe the magnetization undergoing relaxation effects were extended by Torrey (Torrey 1956) to account for the presence of diffusion. The Bloch-Torrey equations read:

$$\frac{\partial \mathbf{M}}{\partial t} = \gamma \mathbf{M} \times \mathbf{B} - \begin{pmatrix} 1/T_2 & 0 & 0 \\ 0 & 1/T_2 & 0 \\ 0 & 0 & 1/T_1 \end{pmatrix} \mathbf{M} + \begin{pmatrix} 0 \\ 0 \\ M_0/T_1 \end{pmatrix} + \nabla \cdot (D \nabla \mathbf{M}) \quad (2.9)$$

with magnetization vector $\mathbf{M} = (M_x, M_y, M_z)^T$ and steady state magnetization M_0 . The last term in Equation (2.9) captures the influence of diffusion and represents another relaxation term.

It can be shown that the magnitude signal in a DWI MRI experiment reads (assuming isotropic diffusion which leads to a Gaussian phase distribution $\rho(\varphi)$ within a voxel as used in Equation (2.7), see also Chapter 2.4):

$$S(b) = S_0 \exp(-bD) \quad (2.10)$$

In-vivo, however, diffusion is most often restricted by cell membranes, vessels or can be even facilitated through e.g. transporters in the cell membrane. Therefore, the apparent diffusion coefficient (ADC) is used to describe the measured diffusion coefficient.

If the motion of water molecules is coherent and aligned along with the diffusion weighting gradient, a net phase instead of signal attenuation results. The individual spins within a voxel have a very similar non-vanishing phase in this case; see Chapter 2.4 for a more detailed description.

DWI is routinely used for clinical diagnosis, such as edema detection and characterization. For example, stroke patients undergo rapid DWI exams with usually very few gradient directions and encoding strengths to assess the extension of edematous brain tissue (Warach et al. 1995). Example brain DWIs of a healthy volunteer with different gradient orientations are shown in Figure 2.2.

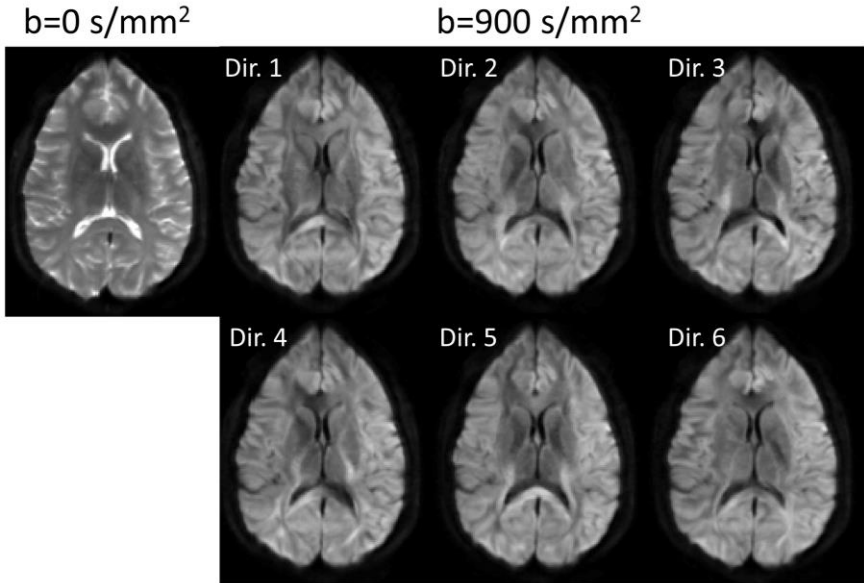


Figure 2.2: Brain DWI. Magnitude images of a healthy volunteer encoded with six different diffusion gradient directions are displayed. Note the different contrast in the central region of the brain where the magnitude is varying under different gradient directions, indicating diffusion anisotropy.

2.1.3 Diffusion tensor imaging

In-vivo, diffusion is anisotropic in most tissues. Diffusion tensor imaging (DTI) is a model describing anisotropic Gaussian diffusion. In this model, the diffusion coefficient is no longer a scalar but a 3x3 tensor:

$$\underline{D} = \begin{pmatrix} D_{xx} & D_{xy} & D_{xz} \\ D_{xy} & D_{yy} & D_{yz} \\ D_{xz} & D_{yz} & D_{zz} \end{pmatrix} \quad (2.11)$$

The tensor in Equation (2.11) is symmetric positive definite and therefore diagonalizable with three eigenvalues λ_1 , λ_2 and λ_3 and corresponding eigenvectors \mathbf{e}_1 , \mathbf{e}_2 and \mathbf{e}_3 , see Figure 2.3 for an illustration.

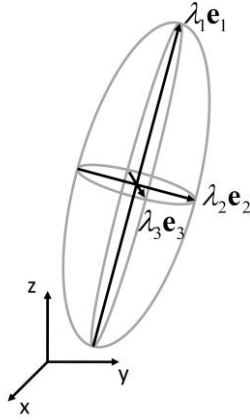


Figure 2.3: Illustration of diffusion tensor eigenvectors scaled with their respective eigenvalues.

The magnitude signal is then dependent on the respective gradient direction and reads:

$$S(\mathbf{b}_i) = S_0 \exp(-\mathbf{b}_i \mathbf{e}_{g_i}^T \underline{D} \mathbf{e}_{g_i}) \quad (2.12)$$

with the i -th \mathbf{b} -vector $\mathbf{b}_i = \mathbf{e}_{g_i} b_i$ where b_i is the i -th diffusion encoding strength as defined in Equation (2.8) and \mathbf{e}_{g_i} is the unit vector in the direction of the i -th diffusion weighting gradient.

The mean diffusivity (MD) is defined as the mean of the eigenvalues:

$$\text{MD} = \frac{1}{3} \text{tr}(\underline{D}) = \frac{1}{3} (\lambda_1 + \lambda_2 + \lambda_3) \quad (2.13)$$

The fractional anisotropy (FA) characterizes the deviation of the diffusion tensor from a sphere (FA=0) in the case of anisotropic diffusion:

$$\text{FA} = \sqrt{\frac{3}{2}} \frac{\sqrt{\sum_{i=1}^3 (\lambda_i - \text{MD})^2}}{\sqrt{\sum_{i=1}^3 \lambda_i^2}} \quad (2.14)$$

Note that these measures are invariant under basis change, i.e. different gradient orientations. However, conditioning of the inference of the diffusion tensor can change by applying different sets of gradient directions.

2.2 Diffusion weighting sequences

For diffusion imaging in most organs, the classical Stejskal-Tanner sequence remains the workhorse. As long as the scanned subject does not move, bulk motion effects (see also Chapter 2.3.2) are negligible and hence diffusion encoding can be performed as described. However, diffusion imaging in the heart poses additional challenges due to myocardial motion and strain.

2.2.1 Gradient moments

In general, the phase accumulation of transverse magnetization during the application of a magnetic field gradient $\mathbf{G}(t)$ depending on the magnetization motion trajectory $\mathbf{x}(t)$ can be expressed as:

$$\varphi(T) = \gamma \int_0^T \mathbf{G}(t) \mathbf{x}(t) dt \quad (2.15)$$

Using Taylor expansion of the motion about an expansion point $t=0$ leads to:

$$\mathbf{x}(t)|_{t=0} = \sum_{n=0}^{\infty} \left(\frac{\partial^n}{\partial t^n} \mathbf{x}(t) \Big|_{t=0} \right) \cdot \frac{1}{n!} t^n \quad (2.16)$$

The accumulated phase can then be approximated as:

$$\varphi(T) = \gamma \left(\int_0^T \mathbf{G}(t) \mathbf{x}|_{t=0} dt + \int_0^T \mathbf{G}(t) \dot{\mathbf{x}}|_{t=0} t dt + \frac{1}{2} \int_0^T \mathbf{G}(t) \ddot{\mathbf{x}}|_{t=0} t^2 dt + \dots \right) \quad (2.17)$$

From Equation (2.17) it can be noted that the accumulated phase depends on the original position of the spins and the gradient moments $\mathbf{m}_n(T)$, which are defined as follows:

$$\begin{aligned}
\mathbf{m}_0(T) &= \int_0^T \mathbf{G}(t) dt \\
\mathbf{m}_1(T) &= \int_0^T \mathbf{G}(t) \cdot t dt \\
\mathbf{m}_2(T) &= \int_0^T \mathbf{G}(t) \cdot t^2 dt \\
&\vdots \\
\mathbf{m}_n(T) &= \int_0^T \mathbf{G}(t) \cdot t^n dt
\end{aligned} \tag{2.18}$$

As shown in the following paragraphs, standard bipolar diffusion encoding gradient waveforms are compensating the 0-th moment, but not higher moments. Hence, myocardial motion and strain add to the phase accumulation in these cases.

2.2.2 Stejskal-Tanner sequence

The Stejskal-Tanner scheme (Stejskal and Tanner 1965) has been widely used in conjunction with spin-echo (SE) sequences. Due to the compensation of only the 0th gradient moment, it is hence termed SE-M0. It can be seen in Figure 2.4 that the first and second gradient moments are not vanishing at echo formation time which makes its application in the heart difficult given strain effects in-vivo, see Chapter 2.2.4 for a detailed discussion. However, application in stationary organs such as the brain is feasible.

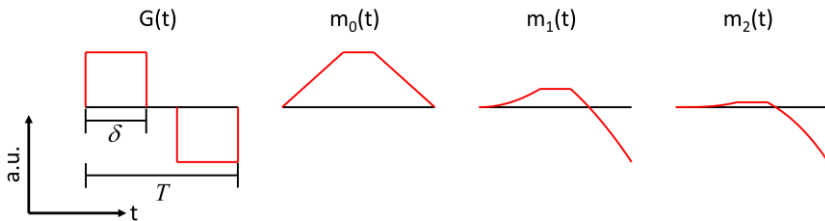


Figure 2.4: Effective Stejskal-Tanner (SE-M0) diffusion weighting gradients and the first three moments. Gradient ramp times are neglected. All plots are scaled to their respective maximum. The first and second moments are non-vanishing during image readout.

2.2.3 Stimulated echo acquisition mode

The application of standard Stejskal-Tanner gradient shapes suffers from strain effects when applied to the beating heart. To address this issue, the stimulated

echo acquisition mode (STEAM) (Frahm et al. 1985) has successfully been applied in-vivo (Edelman et al. 1994; Stoeck et al. 2014; Nielles-Vallespin et al. 2017). This technique distributes the two diffusion encoding gradient lobes across two consecutive heart beats while applying them in identical cardiac phases. Hence, STEAM takes advantage of the periodicity of myocardial motion. However, there are certain limitations such as lower SNR (Fischer et al. 1995; von Deuster et al. 2016b) relative to the SE sequence given that the stimulated echo has half the amplitude of a spin-echo and T_1 decay occurs during the mixing time. Figure 2.5 illustrates a STEAM sequence, which essentially has the same diffusion gradient shape as the SE sequence shown in Figure 2.4, but different timings: relatively short gradient duration δ but a long delay in-between, see also Figure 2.1.

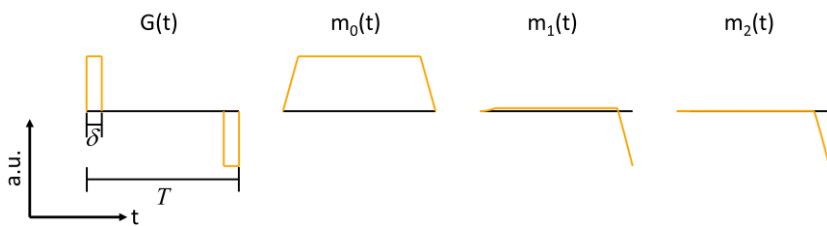


Figure 2.5: Effective STEAM diffusion weighting gradients. Gradient ramp times are neglected. All plots are scaled to their respective maximum. The first and second moments are non-vanishing during image readout. The gradients are played out over two consecutive heart beats in the same cardiac phase of each beat.

During the long diffusion time T (the time between the gradient lobes is also called “mixing time”), water molecules can hit boundaries. The latter and the different encoding in SE yield a lower ADC compared to SE (von Deuster et al. 2016b), see also Chapter 2.4.

2.2.4 Motion compensation

In order to address myocardial motion and strain in SE, higher-order gradient moments can be compensated. First moment compensation accounts for constant velocities of the spins and has improved cardiac SE diffusion imaging (Gamper et al. 2007). Such a gradient waveform is shown in Figure 2.6 and termed SE-M1, compensating both the 0th and 1st moment.

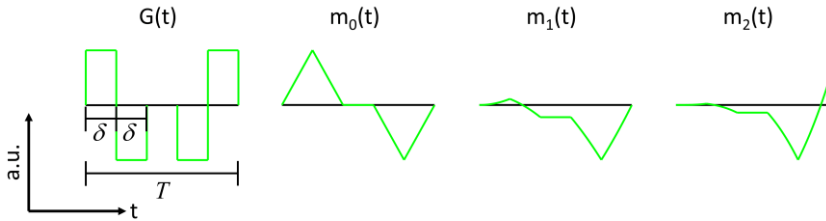


Figure 2.6: Effective SE-M1 diffusion weighting gradients and the first three moments. Gradient ramp times are neglected. All plots are scaled to their respective maximum. The first gradient moment vanishes during readout.

The SE-M1 was further extended to also compensate the second moment. Successful application of SE-M2 DTI has been shown (Stoeck et al. 2016; von Deuster et al. 2016a) (Figure 2.7).

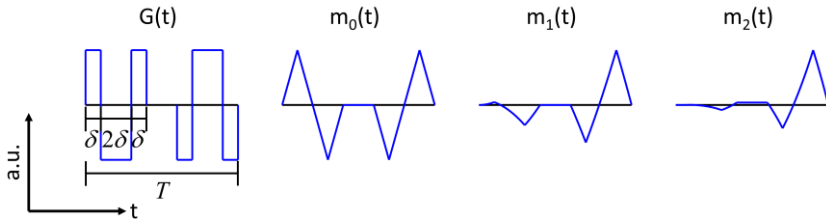


Figure 2.7: Effective SE-M2 diffusion weighting gradients and the first three moments. Gradient ramp times are neglected. All plots are scaled to their respective maximum. All shown gradient moments vanish during readout.

It should be noted that SE-M2 leaves higher order terms that are not compensated for. In addition, the additional gradient lobes prolong echo times and therefore reduce SNR. However, gradient waveform optimization can be performed numerically, in order to shorten echo time (Aliotta et al. 2017; Aliotta et al. 2018). In addition, a shortened version of the SE-M2 waveform exists and is presented in Chapter 7.

2.3 Phase dispersion beyond diffusion

From Equation (2.15) it is noted that any motion will lead to phase accrual in the presence of diffusion weighting gradients. Two relevant effects that often appear conjointly with water self-diffusion are presented in this section.

2.3.1 Intravoxel incoherent motion imaging

Besides water self-diffusion, tissue perfusion takes place in-vivo. The corresponding influence on DWI was noted already about 30 years ago and was modeled with the intravoxel incoherent motion (IVIM) model (Le Bihan et al. 1986; Le Bihan et al. 1988) in conjunction with the Stejskal-Tanner (SE-M0) diffusion weighting sequence. The IVIM model describes perfusion as a pseudo-diffusion process in which the spatial orientation of capillary segments (which are idealized as straight paths with a certain length) is isotropic. The flowing spins are hence thought to undergo a stochastic process similar to water self-diffusion as described in Chapter 2.1. It is hence assumed that spins change direction frequently enough by crossing several capillary segments during the encoding time. In the case where the moving spins mostly remain within one segment (e.g. short encoding time, slow flow and/or long segments), perfusion leads to sinc-like signal modulation depending on the flow velocity and applied first gradient moment. Figure 2.8 illustrates the two models.

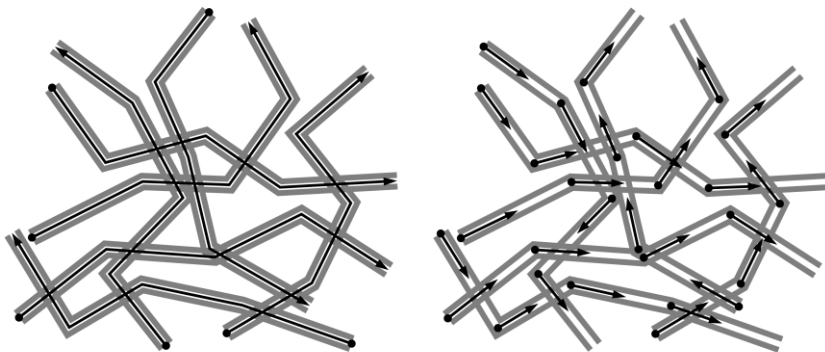


Figure 2.8: IVIM perfusion model. Capillaries (grey) are modeled as a chain of straight segments with a certain length. The spins (black) flow through them with a constant velocity: starting points are marked as dots; end points are denoted as arrows. Left: spins traverse several segments during the encoding time. Right: spins traverse only about half of the segment length in the given time.

The IVIM model therefore represents an additional signal attenuation term depending on the applied gradient strength. Considering both perfusion and diffusion to be isotropic, the model reads:

$$S(b) = S_0 \left[f \cdot F_p(b; l, \nu) + (1 - f) \cdot \exp(-bD) \right] \quad (2.19)$$

with segment length l , velocity ν and attenuation term $F_p(b; l, \nu)$ due to perfusion. The other perfusion related parameter f is called perfusion fraction. It is a number between zero and one, quantifying the relative weight of the perfusion compartment. Therefore, it is a measure of the volume within a voxel which undergoes perfusion. The diffusion term in Equation (2.19) is originally considered a scalar as in DWI described in Chapter 2.1.2. However, using a diffusion tensor as in DTI described in Chapter 2.1.3 can be a more accurate description in-vivo.

The attenuation term due to perfusion is again depending on the amount of dephasing in the voxel and can be expressed in a way similar to Equation (2.7):

$$F_p = \left| \langle \exp(i\varphi) \rangle \right| = \left| \int_{-\infty}^{\infty} \rho(\varphi) \exp(i\varphi) d\varphi \right| \quad (2.20)$$

The individual phases and spin distributions depend on the applied diffusion encoding strength b and the properties of the microcirculation and spatial distribution of the capillary bed.

If the spins are traversing four or more (Le Bihan et al. 1988) segments, the pseudo-diffusion limit can be used to approximate the signal attenuation assuming validity of the Gaussian phase approximation (GPA) of intra-voxel phase distributions. The perfusion attenuation can then be described as another diffusion-like process:

$$F_p(b; l, \nu) = \exp(-bD^*) \quad (2.21)$$

with the pseudo-diffusion coefficient $D^* = \tau \nu^2 / 6$ and characteristic time scale $\tau = l / \nu$. Note that, the additional diffusivity of the flowing blood itself also has to be considered in the pseudo-diffusion coefficient, but it is usually about one order of magnitude smaller than the pseudo-diffusivity of flowing blood (Funck et al. 2018).

If, however, the spins are traversing fewer than four segments, another model containing the first gradient moment has been proposed (Le Bihan et al. 1988):

$$F_p = \left| \frac{\sin(\gamma m_1(T, b) \nu)}{\gamma m_1(T, b) \nu} \right| \quad (2.22)$$

with $m_1(T, b) = |\mathbf{m}_1(T, b)|$ and $\nu = |\mathbf{v}|$ as defined in Equation (2.18).

The IVIM model was extended to capture perfusion anisotropy by considering a von Mises distribution of the zenith angle around a main perfusion direction (Karampinos et al. 2010) or by fitting a perfusion tensor (Abdullah et al. 2016) similar to DTI as described in Chapter 2.1.3. The IVIM signal has also been studied for general cases where the pseudo-diffusion limit is not an applicable description, but perfusion isotropy was assumed (Wetscherek et al. 2015).

Investigations of the exact nature of the perfusion signal in the myocardium considering different gradient waveforms, perfusion anisotropy and other cardiac-specific properties are presented in Chapter 7.

2.3.2 Phase gradients

Bulk motion due to patient movement and/or breathing is a frequent issue in MRI. This type of coherent motion during the application of gradients leads via Equation (2.15) to a net phase within a voxel. A total phase offset results if all of the tissue moves with the same speed. However, in reality velocity gradients occur, leading to phase gradients. Such phase “ramps” across voxels also lead to signal attenuation, similarly to diffusion or perfusion. It can be shown that the phase ramp $\nabla\varphi$ results in signal attenuation of the form

$$F_{\nabla\varphi} = \left| \text{sinc} \left(\frac{1}{2} \nabla\varphi \cdot \mathbf{x}_{res} \right) \right| \quad (2.23)$$

with image resolution \mathbf{x}_{res} .

Besides bulk motion, also eddy currents can induce such undesired phase gradients. If the phase gradients are known, they can be corrected for retrospectively by using Equation (2.23).

2.4 General motion encoding

In addition to the incoherent motion mentioned in Chapter 2.3.1 above, coherent motion also influences the signal. This occurs for example in large vessels where the majority of spins are undergoing a rather deterministic laminar flow. Another example, which occurs frequently in MRI is bulk motion due to patient motion or breathing. In both cases, a net phase and in certain cases magnitude alterations result. Here the analysis is restricted to the motion which occurs during the application of the relatively strong diffusion (and perfusion) weighting gradients, neglecting the influence during application of the relatively weak image encoding gradients.

Consider laminar blood flow through (larger) vessels. The inflowing blood carries fully relaxed longitudinal magnetization and hence enhances the signal magnitude in a partial saturation scenario. This co-called “inflow effect” therefore leads to a local signal increase depending on imaging parameters such as repetition time TR, echo time TE and excitation angle as well as tissue relaxation parameters T₁ and T₂ and the velocity of the inflowing blood (Gao et al. 1996). Besides this amplitude contrast, flow is typically encoded into the signal phase. Various methods of coherent motion encoding hence utilize the resulting phase contrast (Moran 1982; Binter et al. 2013; Knobloch et al. 2014).

Blood flow in vessels can exhibit both coherent and incoherent motion. The following section examines the various influences of coherent and incoherent motion during the application of diffusion-weighting gradients (Kiselev 2017).

2.4.1 Displacement encoding

First, consider a STEAM-like sequence as described in Chapter 2.2.3 with relatively short gradient pulse duration $\delta \ll T$. The net influence $F_{\delta \ll T}$ on the signal can be expressed by using Equation (2.15) and the definition of the 0th gradient moment in Equation (2.18):

$$\begin{aligned}
 F_{\delta \ll T} &= \langle \exp(i\varphi) \rangle \\
 &= \int_{-\infty}^{\infty} \rho(\varphi) \cdot \exp\left(i\gamma \int_0^T \mathbf{G}(t) \cdot \mathbf{x}(t) dt\right) d\varphi \\
 &\approx \int_{-\infty}^{\infty} \rho(\varphi) \cdot \exp(i\gamma \mathbf{m}_0(\delta) \cdot \Delta \mathbf{x}) d\varphi
 \end{aligned} \tag{2.24}$$

Here it is assumed that the spin movement during the gradient lobes is negligible compared to the one during the total diffusion encoding time (“narrow pulse limit” $\delta \ll T$). Therefore, the accrued phase over the total encoding time is proportional to the absolute value of the 0th gradient moment and the spatial displacement $\Delta \mathbf{x} = \mathbf{x}(T) - \mathbf{x}(0)$ in gradient direction. The expression in Equation (2.24) can be approximated by the Taylor expansion $\exp(a) = 1 + a + \frac{1}{2}a^2 + \dots$:

$$F_{\delta \ll T} \approx \int_{-\infty}^{\infty} \rho(\varphi) \cdot \left[1 + i\gamma \mathbf{m}_0(\delta) \Delta \mathbf{x} - \frac{1}{2} (\gamma \mathbf{m}_0(\delta) \Delta \mathbf{x})^2 \right] d\varphi \tag{2.25}$$

The summands in Equation (2.25) can again be expressed as expectation values:

$$F_{\delta \ll T} \approx 1 + i \langle \gamma \mathbf{m}_0(\delta) \Delta \mathbf{x} \rangle - \frac{1}{2} \langle (\gamma \mathbf{m}_0(\delta) \Delta \mathbf{x})^2 \rangle \quad (2.26)$$

It is noted from Equation (2.26) that the first non-constant term induces a phase modulation of the voxel signal. The phase encoding technique that uses this term is referred to as “displacement encoding with stimulated echoes” (DENSE (Aletras et al. 1999)). The second term in Equation (2.26) is proportional to the mean squared displacement and hence represents diffusion-related signal dephasing in a STEAM sequence, see also Chapter 2.1.1. Taking the logarithm of $F_{\delta \ll T}$, using the Taylor expansion $\log(1-a) = -a - \frac{1}{2}a^2 + \dots$ and taking advantage of $\langle \Delta \mathbf{x} \rangle = \mathbf{0}$ in water-self diffusion, the following equation can be retrieved:

$$\log(F_{\delta \ll T}) \approx -\frac{1}{2} \gamma^2 \mathbf{m}_0(\delta)^2 \langle (\Delta \mathbf{x})^2 \rangle \quad (2.27)$$

The definition of the b-value in Equation (2.8) combined with the 0th gradient moment in Equation (2.18) yields $b = \gamma^2 \mathbf{m}_0(\delta)^2 T$. Combining the latter with the expectation value of the squared displacement (see Equation (2.4)) of the Gaussian diffusion process in one dimension $\langle (\Delta \mathbf{x})^2 \rangle = 2DT$ and taking the exponential on both sides of Equation (2.27) leads to

$$F_{\delta \ll T} \approx \exp(-bD) \quad (2.28)$$

2.4.2 Velocity encoding

In this section, gradient waveforms with relatively long gradient lobe duration ($\delta \approx T$) such as the ones presented in Chapter 2.2.2 and 2.2.4 are considered. The narrow pulse limit as used in Chapter 2.4.1 is therefore not applicable. On the contrary, the applied gradients exert a constant influence onto the moving spins during the complete encoding period.

The net influence $F_{\delta \approx T}$ on the signal can be expressed by using Equation (2.15) and the definition of the 0th gradient moment in Equation (2.18):

$$F_{\delta \approx T} = \langle \exp(i\varphi) \rangle = \int_{-\infty}^{\infty} \rho(\varphi) \cdot \exp\left(i\gamma \int_0^T \mathbf{G}(t) \cdot \mathbf{x}(t) dt\right) d\varphi \quad (2.29)$$

Considering all the relevant diffusion weighting sequences shown in Chapter 2.2, it is noted that all of them compensate the 0th gradient moment and hence fulfill the “rephasing condition”, i.e.

$$\mathbf{m}_0(T) = \int_0^T \mathbf{G}(t) dt = \mathbf{0} \quad (2.30)$$

The individual spin trajectory expressed as $\mathbf{x}(t) = \mathbf{x}_0 + \int_0^t \mathbf{v}(\tau) d\tau$, application of integration by parts together with the rephasing condition above in Equation (2.30) leads to a velocity weighting:

$$\begin{aligned} F_{\delta \approx T} &= \int_{-\infty}^{\infty} \rho(\varphi) \cdot \exp\left(-i\gamma \int_0^T \mathbf{m}_0(t) \cdot \mathbf{v}(t) dt\right) d\varphi \\ &= \left\langle \exp\left(-i \int_0^T \mathbf{m}_0(t) \cdot \mathbf{v}(t) dt\right) \right\rangle \end{aligned} \quad (2.31)$$

The expansion of the exponential function as Taylor series $\exp(\mathbf{a}) = 1 + \mathbf{a} + \frac{1}{2}\mathbf{a}^2 + \dots$ in Equation (2.31) yields a sum of expectation values:

$$F_{\delta \approx T} \approx 1 - i \int_0^T \mathbf{m}_0(t) \cdot \langle \mathbf{v}(t) \rangle dt - \iint_{0,0}^{T,T} \mathbf{m}_0(t_1) \mathbf{m}_0(t_2) \cdot \langle \mathbf{v}(t_1) \mathbf{v}(t_2) \rangle dt_1 dt_2 \quad (2.32)$$

The first non-constant term can be considered the phase contrast term as used in flow measurements with constant velocity $\langle \mathbf{v}(t) \rangle = \mathbf{v}_0$.

The second term is the diffusion weighting term of a SE or STEAM sequence with short mixing time. A similar argument as for the derivation of Equation (2.28) holds with the expression of Equation (2.32) as

$$F_{\delta \approx T} \approx \exp(-bD) \quad (2.33)$$

where the coherence $\langle \mathbf{v}(t_1) \mathbf{v}(t_2) \rangle = 2D\Theta(t_2 - t_1)$ with Heaviside step function Θ was used. Note that the diffusion coefficient D in this case is not the same as D in the narrow pulse limit in Equation (2.28).

2.4.3 Diffusion spectrum imaging

As it was shown in the previous Chapter 2.4.1, diffusion leads to signal modulation. Considering only one spatial direction and the narrow pulse limit $\delta \ll T$, the acquired data can be expressed as (neglecting the phase modulating DENSE term) (Callaghan et al. 1979):

$$d_{\delta \ll T}(\mathbf{k}_x, \mathbf{k}_q) = \int \rho(\mathbf{x}) \exp(i\mathbf{k}_x \cdot \mathbf{x}) \exp\left(-\frac{1}{2} \mathbf{k}_q^2 \langle (\Delta \mathbf{x})^2 \rangle\right) d\mathbf{x} \quad (2.34)$$

with spin density ρ and $\mathbf{k}_q = \gamma \mathbf{m}_0(\delta)$. Hence, besides the image frequency spectrum, also the diffusion spectrum can be probed, which is referred to as diffusion spectrum imaging (DSI (Callaghan et al. 1979; Wedeen et al. 2005)). The acquisition with many different diffusion weighting gradients is also called “q-ball imaging” (Tuch 2004). Another terminology is high angular resolution diffusion imaging (HARDI) (Tuch et al. 2002).

2.4.4 Fourier velocity imaging

Also in the case of velocity encoding with $\delta \approx T$ as shown in Chapter 2.4.2, the Fourier encoding during imaging is accompanied by phase and magnitude modulating terms. The imaging signal can be expressed as (Moran 1982):

$$d_{\delta \approx T}(\mathbf{k}_x, \mathbf{k}_v) = \int \rho(\mathbf{x}) \exp(i\mathbf{k}_x \cdot \mathbf{x}) \exp(-i\mathbf{k}_v \cdot \langle \mathbf{v} \rangle) \exp\left(-\frac{1}{2} \mathbf{k}_v^2 \langle (\Delta \mathbf{v})^2 \rangle\right) d\mathbf{x} d\mathbf{v} \quad (2.35)$$

with $\mathbf{k}_v = \gamma \mathbf{m}_1(T)$ and $\mathbf{v} = \bar{\mathbf{v}} + \Delta \mathbf{v}$. Besides coherent flow and steady velocities, fluctuating velocities may be present which in turn lead to signal attenuation. The spectrum of the velocity distribution can hence be probed and this method is termed “Fourier velocity imaging” (Moran 1982).

2.4.5 Implications for intravoxel incoherent motion imaging

It is concluded that any coherent or incoherent motion of particles lead to signal modulation of phase and/or magnitude under the presence of gradients. The perfusion of organs is usually described as a pseudo-diffusion process in the IVIM model. However, if the assumptions of the IVIM model and the narrow pulse limit of encoding are violated, the approximate closed-form relations above might no longer hold. To this end, a detailed investigation of the perfusion induced signal modulation in the heart under various gradient waveforms is presented in Chapter 7.

Chapter 3

Principles of image encoding

In a single-coil MR imaging experiment, the Fourier transform of the object to be imaged is recorded. Various measurements are performed to populate the reciprocal Fourier space, called “k-space”. Assuming a uniform receiving sensitivity and ignoring relaxation effects, the signal $d(\mathbf{k}_\kappa)$ measured at the κ -th k-space point $\mathbf{k}_\kappa \in \mathbb{Z}^3$ is hence given by:

$$d(\mathbf{k}_\kappa) = \int \rho(\mathbf{x}) \exp(i\mathbf{x}\mathbf{k}_\kappa) d\mathbf{x}, \quad (3.1)$$

where $\rho(\mathbf{x})$ is the spin density at position \mathbf{x} .

By approximating the continuous integral in Equation (3.1) by a discrete sum, the expression is rewritten as matrix equation with E being the “encoding matrix” of the κ -th k-space point: $E_\kappa = \exp(i\mathbf{x}\mathbf{k}_\kappa)$. If discretized noisy data $\mathbf{d} \in \mathbb{C}^{n_{xyz}}$ is acquired in k-space and the corresponding discrete image $\mathbf{i} \in \mathbb{C}^{n_{xyz}}$ is to be reconstructed as an estimation of $\rho(\mathbf{x})$, their relation can hence be considered a linear mixed effects model with noise terms $\boldsymbol{\eta} \in \mathbb{C}^{n_{xyz}}$:

$$\mathbf{d} = E\mathbf{i} + \boldsymbol{\eta} \quad (3.2)$$

In case of fully sampled data, a (discrete) Fourier transform relates the measured data and the corresponding image. If data is not fully sampled, this linear system of equations can become rank-deficient. A solution can still be found using the Moore-Penrose pseudoinverse or normal equation respectively (H denotes the Hermitian conjugate):

$$E^H E \mathbf{i} = E^H \mathbf{d} \quad (3.3)$$

Iterative procedures can also be used to find solutions to this “data consistency” problem:

$$\|E\mathbf{i} - \mathbf{d}\|_2^2 < \varepsilon \quad (3.4)$$

where ε is a small real number, e.g. on the order of the measured noise. Such inverse problems are investigated in more detail from a statistics perspective in Chapter 4.1.2. Additional data from multiple receiver coils as explained below can improve the conditioning of the problem.

3.1 Coil combination

Modern MRI scanners use multiple receiver coils for image acquisition. The reconstruction problem in Equation (3.2) becomes overdetermined if the data matrix is (almost) fully sampled. The encoding matrix of Equation (3.2) is no longer square but rectangular in this case. The encoding matrix E hence contains the spatial sensitivity weighting S of the various receiving coils beside the Fourier transform $FT : E = FT \otimes S \in \mathbb{C}^{n_{xyz} \times n_{xyz} n_c}$. The Hermitian conjugate of the Fourier transform FT^H is its inverse FT^{-1} because of the orthogonality of the Fourier transform. Therefore, the coil-combined image of fully sampled data is found by weighting with the sum-of-squares of the coil sensitivities:

$$\mathbf{i} = (S^H S)^{-1} E^H \mathbf{d} \quad (3.5)$$

3.1.1 Roemer combination

The different receiving channels can exhibit noise coherence and/or different noise levels due to electromagnetic coupling and different distances from the object. The noise covariance Ψ can be expressed in matrix form as:

$$\Psi = \boldsymbol{\eta} \cdot \boldsymbol{\eta}^H = \begin{pmatrix} \eta_1 \\ \eta_2 \\ \vdots \\ \eta_c \end{pmatrix} \cdot \begin{pmatrix} \eta_1 \\ \eta_2 \\ \vdots \\ \eta_c \end{pmatrix}^H \quad (3.6)$$

The SNR optimal coil combined image of fully sampled data is then given by (Roemer et al. 1990):

$$\mathbf{i} = (E^H \Psi^{-1} E)^{-1} E^H \Psi^{-1} \mathbf{d} \quad (3.7)$$

The symmetric positive-definite noise matrix Ψ can be decomposed using a Cholesky decomposition $\Psi = LL^H$ (Pruessmann et al. 2001). The following lower triangular matrix L can be inverted and multiplied with the encoding matrix $E \rightarrow L^{-1}E$ and data vector $\mathbf{d} \rightarrow L^{-1}\mathbf{d}$. The incorporation of the noise matrix yields noise decorrelation of k-space data and coil sensitivities. The latter two quantities satisfy the normal equation as stated in Equation (3.3) and from now on, it is assumed that decorrelation has been performed beforehand and is no longer explicitly stated.

3.2 Parallel imaging

Data from multiple receiver coils lead to an overdetermined system of equations and hence data redundancy. This can be exploited to skip parts of the k-space data acquisition in order to accelerate the imaging process. This undersampling approach can be formalized by multiplying a k-space sampling matrix U to the encoding matrix $E \rightarrow UE$. If the data acquired by the various surface coils is linear independent, the achievable undersampling factor R (ratio of acquired k-space to acquisition matrix size) scales with the number of coils. In reality however, attainable undersampling factors for a single undersampling direction are typically between 2 and 4, given inherent electrodynamic limitations (Wiesinger et al. 2004).

3.2.1 SENSE

In sensitivity encoding (SENSE) (Pruessmann et al. 1999), predetermined sensitivity maps S of several surface coils are used for image reconstruction. In the case of regular Cartesian undersampling of k-space, i.e. lines in k-space are sampled with a constant distance larger than required by the Nyquist theorem

$$\Delta k \geq 2k_{\max} \quad (3.8)$$

folding artefacts occur in a regular pattern along this sampling direction. The folded image \mathbf{i}_f can be represented as $\mathbf{i}_f = FT^H UFTS\mathbf{i}$ and hence the unfolded image \mathbf{i} can be found by left multiplying with the Moore-Penrose pseudoinverse (denoted †) of $S' = FT^H UFTS$:

$$\mathbf{i} = S'^{\dagger} \mathbf{i}_f \quad (3.9)$$

An exemplary in-vivo brain data set of a single slice illustrating the SENSE imaging can be found in Figure 3.1.

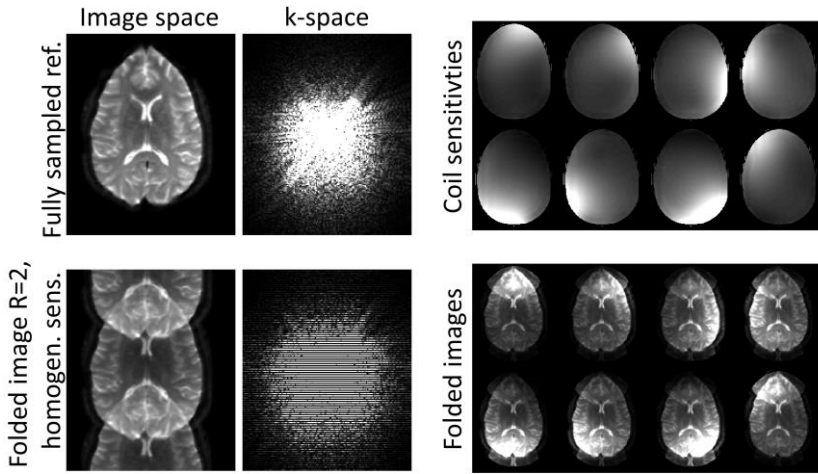


Figure 3.1: SENSE imaging. Regular two-fold Cartesian undersampling in k -space leads to Nyquist replicas in image space. Eight surface coils were used here, which contain additional information aiding the reconstruction process.

In SENSE, two effects compromise image quality. First, SNR scales with $1/\sqrt{R}$. Second, the problem conditioning becomes worse and leads to noise amplification in the image estimate. The conditioning can be expressed as geometric factor (or “g-factor”) (Pruessmann et al. 1999) at voxel position $\mathbf{p} \in \mathbb{Z}^3$:

$$g_{\mathbf{p}} = \sqrt{\left[(S'^H S')^{-1} \right]_{\mathbf{p},\mathbf{p}}} (S'^H S')_{\mathbf{p},\mathbf{p}} \geq 1 \quad (3.10)$$

Considering both effects, the SNR at position \mathbf{p} of the reduced data acquisition with undersampling factor R is

$$SNR_{\mathbf{p}}^R = \frac{SNR_{\mathbf{p}}^{full}}{\sqrt{R} g_{\mathbf{p}}} \quad (3.11)$$

where $SNR_{\mathbf{p}}^{full}$ is the SNR of the fully sampled acquisition. However, if the echo time TE is simultaneously reduced, signal can be partly regained according to $\exp(\Delta TE/T_2)$ in a SE experiment for example, where ΔTE is the echo time reduction due to SENSE and T_2 the transversal relaxation constant.

For practical purposes an approximate calculation with relative error on the order of $1/SNR_p^{full}$ is given in (Nordmeyer-Massner et al. 2009):

$$SNR_p^{full} \approx \sqrt{\mathbf{d}_p^H \cdot \mathbf{d}_p} \quad (3.12)$$

Note that \mathbf{d}_p is the noise decorrelated complex vector containing the signal of all coils of the fully sampled acquisition.

While a solution to the SENSE problem in Equation (3.9) can be found via direct inversion, this approach can be computationally expensive. As stated in (Pruessmann et al. 2001), iterative methods such as conjugate gradients (CG) yield a solution with considerable fewer operations relative to direct inversion. Moreover, in many cases where the problem is reasonably conditioned, fewer iterations than theoretically predicted yield sufficient results. An optimization problem can be formulated (by identifying the encoding matrix as $E' = UFTS$):

$$\underset{\mathbf{i}}{\operatorname{argmin}} \|\mathbf{E}'\mathbf{i} - \mathbf{d}\|_2^2 \quad (3.13)$$

In poorly conditioned cases, further regularization $R(\mathbf{i})$ such as Tikhonov regularization of the data or its variation in image space (“total variation”) can aid the reconstruction process:

$$\underset{\mathbf{i}}{\operatorname{argmin}} \|\mathbf{E}'\mathbf{i} - \mathbf{d}\|_2^2 + R(\mathbf{i}) \quad (3.14)$$

Please also see Chapter 4.2 for a statistical view on this topic.

Besides the SENSE approach to parallel imaging, alternative procedures exist including SMASH (Sodickson and Manning 1997) and autocalibration methods such as GRAPPA (Griswold et al. 2002), SPIRiT (Lustig and Pauly 2010) and ESPIRiT (Uecker et al. 2014). Note that autocalibration methods need a fully sampled k-space center, but are not affected by motion of the object relative to the acquired sensitivity maps as in SENSE. The ESPIRiT method provides estimates of the sensitivity maps, which can be used for a SENSE-like reconstruction.

3.3 Partial Fourier imaging

If an object is real-valued, its representation in the conjugate Fourier k-space possesses Hermitian symmetry, i.e.

$$d(\mathbf{k}_x) = \int \rho(\mathbf{x}) \exp(i\mathbf{x}\mathbf{k}_x) d\mathbf{x} = \bar{d}(-\mathbf{k}_x) \quad (3.15)$$

Data acquisition of static organs such as the brain for example can hence be accelerated by skipping data acquisition of one half of the k-space in theory. If no spatial phase variation is present, direct conjugate replacement of the non-acquired part of k-space is possible (Feinberg et al. 1986). In reality, however, additional phase variation is present caused by inhomogeneity of the main magnetic field, susceptibility induced field gradients and eddy currents due to gradient switching. If more than half of k-space is acquired, local phase variations can be accommodated. Therefore, only a part of the second half of k-space is skipped in typical MRI experiments. The remaining part of the second half of k-space together with the corresponding part in the other part of k-space serves as low resolution phase estimation in the one-step homodyne filtering method (Noll et al. 1991) as illustrated in Figure 3.2 or in iterative methods (Haacke et al. 1991).

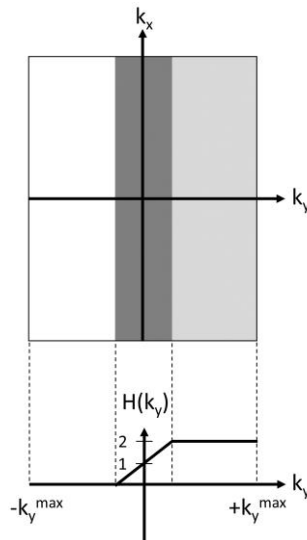


Figure 3.2: 2D partial Fourier acquisition in y-direction. The white part in the 2D k-space above is not sampled, while samples are acquired in the dark gray area in the k-space center and in the light gray area. During homodyne reconstruction, the central part is weighted with a filter function H , which contains a linear ramp for the central part. The acquired outer k-space is weighted twice to compensate the missing signal power from the non-acquired part.

If only a part of k-space is sampled, SNR is decreased by $1/\sqrt{R}$ but the shortening of echo time can lead to a signal increase as described also for SENSE in Chapter 3.2.1.

Note, however, that object movement translates to additional motion-induced phase via the Fourier shift theorem. Depending on the movement amplitude, partial Fourier acquisition can be applied with a low reduction factor only or might be unsuitable in fast moving organs such as the heart.

3.4 Compressed Sensing

Another approach to MR data undersampling is Compressed Sensing (Candes et al. 2006), where sparsity in a transform domain of the images is exploited. Incoherent (under-)sampling introduces noise-like artifacts into the images which are then reconstructed by non-linear denoising in the transform domain. This approach requires sufficient sparsity of the original object or a transformed representation thereof to retrieve the object signal. Image reconstruction for Compressed Sensing (Lustig et al. 2007) is formulated as an optimization problem which is solved iteratively:

$$\operatorname{argmin}_i \|\mathbf{E}\mathbf{i} - \mathbf{d}\|_2^2 + \lambda \|\Phi\mathbf{i}\|_1 \quad (3.16)$$

Here, Φ is a sparsifying transform such as Wavelets (Daubechies 1988) and λ is a regularization parameter. Non-linear solvers are required due to the L_1 -norm regularization. A statistical motivation for this approach is given in Chapter 4.4.

3.5 Reconstruction of sheared grid k-space data

In many MRI data acquisition protocols, data is acquired along an additional dimension besides the spatial ones: time in dynamic imaging (cine, flow imaging, first-pass perfusion etc.) and diffusion weighting in DWI/DTI. The acquired images typically share many features and hence exhibit correlations among space and the additional dimension. These can be used for higher undersampling factors compared to parallel imaging alone. Data undersampling may either be performed in a regular fashion as explained further in the next sections or in an incoherent way.

3.5.1 Sheared grid k-t undersampling

Regular undersampling as presented for SENSE reconstruction in Chapter 3.2.1 can be modified by a shift of the sampling pattern from one frame to the other. This results in a “sheared grid”-like k-t sampling pattern with resultant aliases in image space. The aliases at the temporal band edge may be suppressed using a low-pass filter (Madore et al. 1999). More general, a Fourier transform along the additional dimension serves as a sparsifying transform. In addition, the Fourier transform leads to better separation of the undersampling aliases: the linear shift of the sampling pattern in k-space causes a phase offset in image space, which again leads to separation of the object aliases in the frequency spectrum space via the Fourier shift theorem.

Shear grid or k-t undersampling (Tsao et al. 2003) was first applied for dynamic/temporal imaging. The resulting space of the acquired data after a Fourier transform along the image dimensions and the additional dimension is called x-f space. The point spread function (PSF) in the x-f space is hence not a column but a diagonal as shown in Figure 3.3.

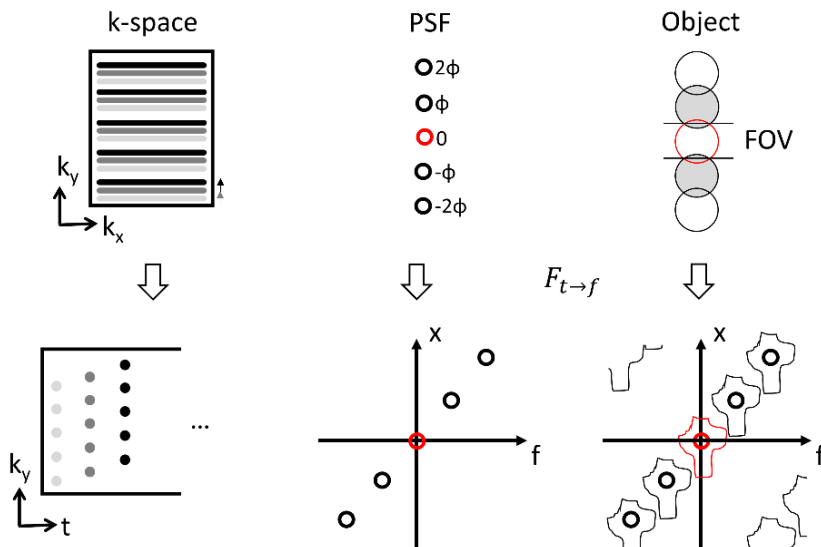


Figure 3.3: k-t undersampling. A sheared grid results if a regular grid is shifted along the additional temporal dimension (left). This translates into an additional phase ϕ and hence a diagonal point spread function in x-f space (center). The aliases in image space are separated in x-f space (right).

3.5.2 k-t BLAST & k-t SENSE

In k-t BLAST and k-t SENSE (Tsao et al. 2003) a few central lines which serve as low-resolution image information are acquired alongside the sheared-grid undersampled data. This “training data” is used as weights in the x-f space and allow unfolding of overlapping signal aliases in this domain. The first method (k-t BLAST) uses only one coil, while k-t SENSE uses additional information from multiple coils, as explained in Chapter 3.2.1. The encoding matrix contains a Fourier transform $F_{t \rightarrow f}$ along the additional (e.g. temporal) dimension for the reasons explained above:

$$E'' = E' F_{t \rightarrow f} \quad (3.17)$$

Likewise, this can be considered a SENSE reconstruction as in Equation (3.14) with Tikhonov regularization. Similar to the normal equation of the image reconstruction problem in Equation (3.3), an equation for the imaging problem can be derived:

$$\left[E''^H E'' + \lambda \left({}^{x-f}M \right)^{-2} \right] \mathbf{i} = E''^H \mathbf{d} \quad (3.18)$$

with regularization parameter λ and training matrix ${}^{x-f}M$, which represents prior knowledge from low resolution images, see also Chapter 4.2 for further statistical explanations. Note that as stated above, it is assumed that noise decorrelation as explained in Chapter 3.1.1 has been performed beforehand. A direct solution can be found if the matrices are invertible:

$$\mathbf{i} = \left[E''^H E'' + \lambda \left({}^{x-f}M \right)^{-2} \right]^{-1} E''^H \mathbf{d} \quad (3.19)$$

As explained above, iterative solutions can often be faster to calculate compared to direct solutions. It is numerically favorable for the solver to operate in the x-t space compared to the x-f space because of the preference of similar finite differences and variations. Hence, an iterative solution to Equation (3.18) can be formulated in x-t space as follows:

$$\underset{\mathbf{i}}{\operatorname{argmin}} \left\| E' \mathbf{i} - \mathbf{d} \right\|_2^2 + \lambda \left\| \left({}^{x-f}M \right)^{-1} F_{t \rightarrow f} \mathbf{i} \right\|_2^2 \quad (3.20)$$

Note that that the encoding matrix E' in Equation (3.20) is the same as for the SENSE problem in Equation (3.13) or the regularized version in Equation (3.14).

3.5.3 k-t PCA

The aforementioned k-t methods are well suited for the reconstruction of periodic signals due to the used Fourier transform. However, if fast changes in-between images occur, higher Fourier components become relevant and lead to a broadening and increased overlap of the signal aliases in x-f space. In order to further sparsify data, a principal component analysis (PCA) can be employed. This orthogonal linear transformation produces decorrelated data in the new basis (principal components). The procedure is optimal for Normal distributed input in terms of data compressibility, but does not pose a restriction on data distribution. The principal components need to be calculated for every data set and are ordered in descending order in terms of explained data variance. The basis functions of the PCA decomposition are determined using the low-resolution training data. The amended version of k-t SENSE which takes advantage of a PCA transform is hence called k-t PCA (Pedersen et al. 2009). Unlike the former method, k-t PCA performs unfolding of undersampled images in the x-pc instead of x-f space. The encoding matrix reads:

$$E''' = E'' B_{f \rightarrow pc} \quad (3.21)$$

with E'' as defined in Equation (3.17). A direct solution to the k-t PCA reconstruction problem is available (Pedersen et al. 2009) besides the iterative procedure:

$$\underset{\mathbf{i}}{\operatorname{argmin}} \left\| E' \mathbf{i} - \mathbf{d} \right\|_2^2 + \lambda \left\| \left({}^{x-pc} \mathbf{M} \right)^{-1} B_{f \rightarrow pc} F_{t \rightarrow f} \mathbf{i} \right\|_2^2 \quad (3.22)$$

Note that the training matrix ${}^{x-pc} \mathbf{M}$ is now in x-pc space. Again, we assume prior noise decorrelation.

3.5.4 Incoherent sampling and non-linear reconstruction

All of the above-mentioned methods employ regular sampling and find an image estimate using Tikhonov regularization of the parallel imaging problem. Along the lines of Chapter 3.4, reconstruction with the usage of incoherent sampling, a sparsifying transform along the additional data dimension and a L_1 regularization is also possible as for example shown in k-t SPARSE (Lustig et al. 2006) and k-t FOCUSS (Jung et al. 2009). These methods require non-linear solvers in contrast to the presented k-t methods, which are linear LSQ problems.

Chapter 4

Applied Bayesian statistics for MRI

4.1 Introduction to Bayesian statistics

In probability theory, three axioms must hold for any probability measure according to Kolmogorov. They can be described in a collegial manner as: a probability is a number between zero and one, sure events have a probability of one and the probability of a countable number of pairwise disjoint events is the sum of their probabilities (“sigma-additivity”). These theoretical requirements leave room for interpretation of probability itself. Probably the most popular one is the so-called “frequentist” approach to statistics. There, it is assumed that the frequency of events corresponds to their probabilities. One of the most proliferate and widely known representative of this branch of statistics was Ronald Fisher. Another alternative approach is the so-called “Bayesian” interpretation where probability is considered as a quantification of personal belief and probabilities are therefore assigned to hypotheses. Pierre-Simon Laplace and Thomas Bayes pioneered this approach. Both methods are widely used in all branches of science wherever empirical data is statistically analyzed. Typically, frequentist methods are fast to calculate and require (almost) no prior knowledge, but they can be unintuitive to interpret. In contrast, Bayesian methods often require computers, but they are well suited to take into account prior knowledge in a rigorous way and provide a framework for multi-hierarchical models. In this chapter, a Bayesian view on MRI reconstruction and IVIM parameter estimation is given.

4.1.1 Bayes’ theorem

Bayes’ theorem allows for the calculation of conditional probabilities, i.e. that one event A occurs, given another event B :

$$P(A|B) = \frac{P(B|A) \cdot P(A)}{P(B)} \quad (4.1)$$

with $P(B) > 0$. This theorem is particularly useful to draw inference about $P(A|B)$ where $P(B|A)$ is given. Note that both frequentists and Bayesians make wide use of the theorem, albeit with slightly different interpretations.

4.1.2 Data likelihood

The (data) likelihood function $p(\mathbf{y}|\theta)$ contains the statistical model of the forward data generating process and is hence a function of the model parameters θ and the given data \mathbf{y} . The former can be for example IVIM parameters or MR image estimates, while the latter would be magnitude image data or k-space data, respectively. Here we interpret the likelihood from the Bayesian perspective, i.e. the likelihood function is considered the probability of the measured data conditioned on the model parameters.

If several data points are available, the total likelihood is the product of the individual likelihoods if “exchangeability” of the samples is assumed (corresponds to independence and identical distribution of the samples in frequentist statistics). Typically, the error terms in MRI signals are assumed to be Gaussian. This is, however, only true in a strict way for the real and imaginary parts of the signal. Other quantities such as the magnitude follow a Rician distribution, but can adequately be described as Gaussian distributed for SNR factors larger than 2 (Gudbjartsson and Patz 1995), which is usually achieved in typical MRI experiments. To conclude, in many MRI inversion problems, the data likelihood takes the following form:

$$p(\mathbf{y}|\theta=(\mu,\sigma))=\prod_{n=1}^N\frac{1}{\sqrt{2\pi\sigma^2}}\exp\left[-\frac{(y_n-\mu)^2}{2\sigma^2}\right] \quad (4.2)$$

with N data points concatenated in the data vector $\mathbf{y}\in\mathbb{R}^N$, mean value μ and standard deviation σ of the Gauss distribution. The last quantities are hence unknown parameters.

4.1.3 Posterior distribution

According to the Bayes’ theorem in Equation (4.1), we can identify a posterior distribution $p(\theta|\mathbf{y})$ which depends on the data likelihood $p(\mathbf{y}|\theta)$, the prior distribution $p(\theta)$ (see Chapter 4.1.4) and the data normalization factor $p(\mathbf{y})$ in the following way:

$$p(\theta|\mathbf{y})=\frac{p(\mathbf{y}|\theta)p(\theta)}{p(\mathbf{y})} \quad (4.3)$$

Parameter inference is typically performed via the posterior mean by calculating the expectation value:

$$\hat{\theta} = \langle \theta \rangle = \int \theta \cdot p(\theta | y) d\theta = \frac{1}{p(y)} \int \theta \cdot p(y | \theta) \cdot p(\theta) d\theta \quad (4.4)$$

See Chapter 4.2 for more details on parameter inference.

4.1.4 Prior distribution

The prior distribution $p(\theta)$ describes the a-priori knowledge of the parameters to infer. In principle this could be any function with the only restriction that it should be integratable (or at least locally numerically tractable). An example for such a prior is for example Jeffreys' prior (Jeffreys 1946)

$$p(\theta) \propto \sqrt{\det(I(\theta))} \quad (4.5)$$

which uses the Fisher Information matrix $I(\theta)$. This prior belongs to the class of “reference priors” (Berger et al. 2009). With such priors, inferential statements depend only on the assumed statistical model and the data available and do not require parameter tuning. Jeffreys' prior yields inference that is also invariant upon re-parametrization.

Another popular class of priors are the “conjugate” priors. Such a prior is in the same probability distribution family as the posterior and hence leads to a closed-form expression of the product of prior and data likelihood. They depend on the parametrization of the shape and scale parameters of the distribution used in the data likelihood, see Chapter 4.5 for an example. Note that multi-hierarchical priors can be constructed: the distribution parameters (called hyperparameters) of a prior can follow another prior distribution. This allows the formalization of complex prior knowledge on multiple levels.

From a theoretical perspective it is worthwhile to note that according to the Bernstein-von Mises theorem (van der Vaart 1998), the posterior distribution becomes asymptotically (i.e. if the amount of data points gathered approaches infinity) independent of the chosen prior under some weak conditions. This means that Bayesian estimates are asymptotically equal to the ones from frequentist inference.

4.2 Bayesian inference

In this section, the inference of model parameters is elucidated from a Bayesian perspective, various computational methods are presented together with technical details.

4.2.1 Analytic evaluation

The posterior hyperparameters depend on both the likelihood parameters and prior hyperparameters. They can be expressed in closed-form for conjugate priors.

Here, an example of MRI magnitude data is considered, which was acquired during an IVIM experiment. The measured IVIM magnitude signal y_i at the i -th datum contains a Gaussian error distribution with standard deviation σ_s and mean $S_0 g_i$. The first factor of the latter expression is the magnitude of images without diffusion weighting, the second factor describes the IVIM signal at the i -th b-value with IVIM parameters $\boldsymbol{\theta} = (D, f, D^*)$. Therefore, the data likelihood is a Normal distribution:

$$p(\mathbf{y} | \boldsymbol{\theta}, S_0, \sigma_s^2) = (2\pi\sigma_s^2)^{-N/2} \exp\left[-\frac{1}{2\sigma_s^2} \sum_{n=1}^N (y_n - S_0 g_n(\boldsymbol{\theta}))^2\right] \quad (4.6)$$

with magnitude data vector $\mathbf{y} = (y_1 \dots y_N)^T$. Since the standard deviation (representing measured noise) and the normalization factor are of no interest, they are “nuisance” parameters which can be dealt with in a Bayesian fashion: their influence is retained, but their explicit dependence can be overcome by “marginalizing” them out. This means that conjugate priors for both parameters are chosen: a Normal prior for S_0 and an inverse-Gamma distribution for the variance σ_s^2 . The product then reads:

$$p(S_0, \sigma_s^2) = p(S_0) \cdot p(\sigma_s^2) = N(S_0 | 0, \delta^2) \cdot IG(\sigma_s^2 | \alpha, \beta) \quad (4.7)$$

The product of data likelihood and prior is then again a product of a Normal (N) and inverse-Gamma (IG) distribution (Murphy 2007) with mean μ' , standard deviation σ' and the inverse-Gamma shape α' and scale parameters β' :

$$\begin{aligned} \mu' &= \frac{N\bar{y}}{\delta^2 + N} \\ \sigma'^2 &= \delta^2 + N \\ \alpha' &= \alpha + \frac{N}{2} \\ \beta' &= \beta + \frac{1}{2} \sum_{n=1}^N (y_n - \bar{y})^2 + \frac{N\delta^2}{N + \delta^2} \frac{\bar{y}^2}{2} \end{aligned} \quad (4.8)$$

with sample mean value \bar{y} . By integrating over the nuisance parameters S_0 and σ_s^2 , a marginal distribution without their explicit dependence can be found: in this case, a (scaled and shifted) Student's t- distribution follows with mean μ' , $2\alpha'$ degrees of freedom and scale parameter $\frac{\beta'(\sigma'^2 + 1)}{\sigma'^2 \alpha'}$.

Inference of desired quantities such as mean, median, mode etc. can then be derived analytically from this marginal distribution.

4.2.2 Maximum a-posteriori point estimator

The maximum a-posteriori (MAP) estimator is a point estimator, which provides point estimates of model parameters via maximization of the posterior distribution. Hence, the method makes use of the mode of the posterior distribution. The approach is therefore similar to the frequentist maximum likelihood estimate (MLE), in which only the likelihood function is used without a prior. Problems that cannot be handled analytically as outlined in the section before can still be investigated.

Here the reconstruction problem in Equation (3.2) is considered, which has a closed-form expression of the MLE. Gaussian error terms with covariance matrix Ψ are considered in the data likelihood:

$$p(\mathbf{d}|\mathbf{i}) \propto \exp\left[-\frac{1}{2}(\mathbf{d}-\mathbf{E}\mathbf{i})^H \Psi^{-1}(\mathbf{d}-\mathbf{E}\mathbf{i})\right] \quad (4.9)$$

Both for MLE and MAP estimation, the logarithm can be taken for a more convenient optimization of sums instead of products.

First, consider the MLE of Equation (4.9) which can then be found via

$$\begin{aligned} \hat{\mathbf{i}}_{MLE} &= \underset{\mathbf{i}}{\operatorname{argmax}} \log[p(\mathbf{d}|\mathbf{i})] \\ &= \underset{\mathbf{i}}{\operatorname{argmax}} \left[-\frac{1}{2}(\mathbf{d}-\mathbf{E}\mathbf{i})^H \Psi^{-1}(\mathbf{d}-\mathbf{E}\mathbf{i})\right] \end{aligned} \quad (4.10)$$

The closed form solution if no noise correlation is present ($\Psi = \mathbf{I}\mathbf{d}$) can be shown to be the ordinary least-squares (OLS) estimator by differentiating and setting to zero:

$$\hat{\mathbf{i}}_{MLE}^{OLS} = (\mathbf{E}^H \mathbf{E})^{-1} \mathbf{E}^H \mathbf{d} \quad (4.11)$$

If the noise matrix is not the identity matrix, the MLE is the generalized least-squares (GLS) estimator, which is also used in Chapter 3.1.1:

$$\hat{\mathbf{i}}_{MLE}^{GLS} = (\mathbf{E}^H \Psi^{-1} \mathbf{E})^{-1} \mathbf{E}^H \Psi^{-1} \mathbf{d} \quad (4.12)$$

Second, the MAP is considered for the data likelihood of the reconstruction problem above together with a Gaussian prior with zero mean and covariance matrix Γ . The posterior therefore reads:

$$p(\mathbf{i} | \mathbf{d}) \propto \exp\left[-\frac{1}{2}(\mathbf{d} - \mathbf{E}\mathbf{i})^H \Psi^{-1} (\mathbf{d} - \mathbf{E}\mathbf{i})\right] \cdot \exp\left(-\frac{1}{2}\mathbf{i}^H \Gamma^{-1} \mathbf{i}\right) \quad (4.13)$$

After taking the logarithm and neglecting some constants, the logarithm of the posterior is for this choice of prior covariance matrix $\Gamma = \lambda^{-1} \mathbf{Id}$:

$$\log(p(\mathbf{i} | \mathbf{d})) \propto (\mathbf{d} - \mathbf{E}\mathbf{i})^H \Psi^{-1} (\mathbf{d} - \mathbf{E}\mathbf{i}) + \lambda \mathbf{i}^H \mathbf{i} \quad (4.14)$$

The noise covariance matrix can be decomposed and multiplied with the encoding matrix and k-space data as described in Chapter 3.1.1. The logarithm of the posterior can then be expressed as:

$$\log(p(\mathbf{i} | \mathbf{d})) \propto \|\mathbf{d} - \mathbf{E}\mathbf{i}\|_2^2 + \lambda \|\mathbf{i}\|_2^2 \quad (4.15)$$

From Equation (4.15) it can be inferred that a Gaussian prior corresponds to a Tikhonov regularization. Furthermore, the right side of Equation (4.15) can be minimized with respect to \mathbf{i} in order to find the MAP point estimate, which leads to an analytical solution in this case. The resulting regularized least-squares (RLS) point estimator reads in closed form:

$$\hat{\mathbf{i}}_{MAP}^{RLS} = (\mathbf{E}^H \Psi^{-1} \mathbf{E} + \Gamma^{-1})^{-1} \mathbf{E}^H \Psi^{-1} \mathbf{d} \quad (4.16)$$

This regression method is also called Ridge regression. Note that the matrix Γ is not restricted to the presented (scaled) identity matrix. Numerical solutions are also available from iterative optimization procedures as discussed in Chapter 3.5.2.

The MAP has certain drawbacks in general: first, it is not invariant under re-parametrization. Second, in pathological datasets where the mode is not representing the actual data (e.g. an additional spike in the histogram), results can be confounded. The MAP is hence less robust compared to other estimates such as the posterior mean or median.

4.2.3 Markov chain Monte Carlo

To overcome the limitations of the MAP estimator, the posterior mean or median can be used for inference. This can be done analytically as shown in Chapter 4.2.1 in the case of conjugate distributions. In general, however, (high-

dimensional) integrals of the product of likelihood and prior distribution are intractable analytically, especially in the case of multi-level hierarchical models. The Markov chain Monte Carlo (MCMC) method can still provide numerical results via sampling from a Markov chain, which contains the desired posterior as stationary distribution. Desired quantities such as the expectation value of a variable can be easily inferred via a Monte Carlo approach of replacing the integral by an approximating sum of N_s samples, applying the law of large numbers:

$$\hat{\theta} \approx \frac{1}{N_s} \sum_{j=1}^{N_s} \theta^{(j)} \quad (4.17)$$

This method hence provides samples from the posterior and not only a point estimate as the MAP. However, this comes at a computational cost, because typically tens of thousands or more samples need to be drawn.

MCMC sampling techniques are a vast and active research field in the computational statistics community. Many software packages are available: BUGS variations (WinBUGS (Lunn et al. 2000) for Windows, the open-source cross-platform variant OpenBUGS (Lunn et al. 2009) and the C++ implementation JAGS (Plummer 2003)), STAN (Carpenter et al. 2017) and Google’s TensorFlow Probability (Dillon et al. 2017) for example.

4.2.4 Variational Bayes methods

Besides the MCMC approach, variational approaches are available (Bishop 2006). The idea here is to find an analytic approximation to the posterior distribution, which for example minimizes the Kullback-Leibler divergence of the posterior from its approximation via calculus of variations. These methods are typically faster than MCMC but require the derivation of many equations for each problem. In addition, they do not yield asymptotically correct approximations in general, unlike MCMC. A software implementation of variational Bayes can be found for example in STAN (Carpenter et al. 2017) and Google’s TensorFlow Probability (Dillon et al. 2017).

4.3 Gaussian prior & k-t methods

Returning to MAP estimators, a statistical motivation for the k-t reconstruction problems as described in Chapter 3.5 is given in this section as an extension to Chapter 4.2.2.

In the case of k-t BLAST/SENSE problems, the reconstruction operates in the x-f space, which means that the encoding matrix also contains a Fourier

transform along the additional dimension as stated in Equation (3.17). Furthermore, the covariance matrix of the data in x-f space is no longer a scaled identity matrix but is instead estimated from training data: $\Gamma = {}^{x-f}M = \frac{{}^{x-f}\mathbf{i}_{train} {}^{x-f}\mathbf{i}_{train}^H}{}$. The prior is therefore a Normal distribution with zero mean and covariance matrix Γ . Typically, this prior is relaxed by multiplying the aforementioned covariance matrix with a regularization parameter, because the training data typically has a limited spatial resolution that can lead to loss in spatial details due to prior influence. In a similar fashion as outlined in Chapter 4.2.2, the logarithm of the posterior can be derived:

$$\log(p(\mathbf{i}|\mathbf{d})) \propto \|\mathbf{d} - E\mathbf{F}_{f \rightarrow t} {}^{x-f}\mathbf{i}\|_2^2 + \left\| \left({}^{x-f}\Gamma \right)^{-1} {}^{x-f}\mathbf{i} \right\|_2^2 \quad (4.18)$$

Setting $\Gamma = \lambda^{-1} \cdot {}^{x-f}M$ in order to control (usually dampen) the prior influence, it can be expressed as:

$$\log(p(\mathbf{i}|\mathbf{d})) \propto \|\mathbf{d} - E\mathbf{F}_{f \rightarrow t} {}^{x-f}\mathbf{i}\|_2^2 + \lambda \left\| \left({}^{x-f}M \right)^{-1} {}^{x-f}\mathbf{i} \right\|_2^2 \quad (4.19)$$

Using $\mathbf{i} = \mathbf{F}_{f \rightarrow t} {}^{x-f}\mathbf{i}$, a solution in x-t space (instead of x-f space) can be found and the reconstruction functional in Equation (3.20) is retrieved.

The reconstruction formula for k-t PCA in Equation (3.22) can be derived from this statistical perspective in an analogous way as described above. In addition to k-t BLAST/SENSE, a PCA decomposition is added such that the solution to the reconstruction problem is in x-pc space: $\mathbf{i} = \mathbf{F}_{f \rightarrow t} \mathbf{B}_{pc \rightarrow f} {}^{x-pc}\mathbf{i}$. Therefore, also the training data is in x-pc space. Equation (3.22) can be found if the solution is searched in x-t space.

4.4 Laplace prior & Compressed Sensing

A similar argument holds to derive Equation (3.16), which describes the Compressed Sensing problem. Here, the prior is chosen to be a Laplace distribution and reconstruction is performed in the sparse (e.g. Wavelet) domain. Applying the same procedure as above of taking the logarithm of the resulting posterior, differentiating and setting to zero, the L_1 -regularized problem in Equation (3.16) follows. This estimator corresponds to the so-called LASSO (least absolute shrinkage and selection operator) estimator (Tibshirani 1996).

It is worth noting that the Laplace distribution concentrates more weight around its mean compared to a Gauss distribution, hence the regularization is

more “aggressive” in weighting lower-order components of the new basis (e.g. Wavelets); see also Figure 4.1 for an illustration.

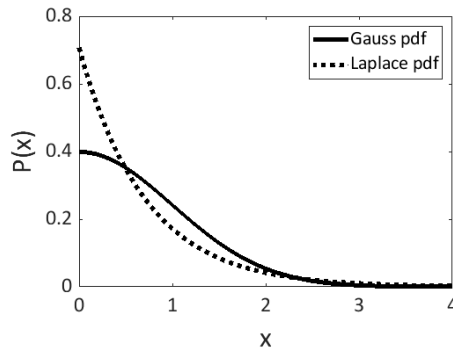


Figure 4.1: Probability distribution functions (pdf) of both a univariate Gauss and Laplace distribution. Both distributions have a variance of one and zero mean. Note the relatively large probability weight of small x of the Laplace distribution.

4.5 Hierarchical priors and curve fitting

So far, only one-level priors were used in which the prior hyperparameters were set to a single value. However, as stated in the Chapter 4.1, multiple levels are possible, i.e. prior hyperparameters can follow other distributions themselves. Here, the statistical model used in Chapter 6 for IVIM parameter estimation (“curve fitting”) is presented in more detail.

The marginalized data likelihood from Chapter 4.2.1 that contains the IVIM model and Gaussian noise is combined with a multivariate Normal distribution of all the N log/logit transformed IVIM parameter estimates considered in the ROI as prior. On top of this prior level, Jeffreys’ prior (see Chapter 4.1.4) is put on the prior hyperparameters of the multivariate Gaussian distribution, namely mean and covariance matrix. Figure 4.2 illustrates this multi-level hierarchical model in full detail.

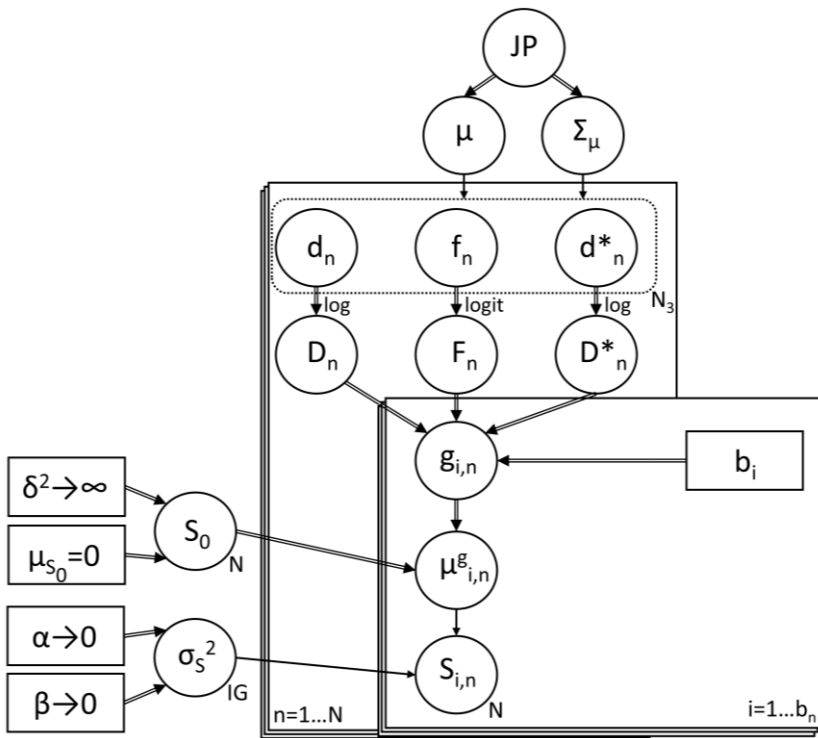


Figure 4.2: Directed acyclic graph representing the Bayesian network used for IVIM parameter estimation. Circles are stochastic nodes, rectangles are constant values, stacked rectangles represent data vectors. Single arrows represent stochastic relations, double arrows represent analytic relations. If the distribution of a variable is given, it is noted as follows: N/N_3 stands for uni-/tri-variate Normal distribution, IG for inverse-Gamma and JP for Jeffreys' prior. A text arrow informally notes the limit that a variable is approaching.

Chapter 5

Enhancing intravoxel incoherent motion parameter mapping in the brain using k-b PCA¹

5.1 Introduction

In the brain, IVIM parameters have been shown to be increased during a hypercapnia challenge, a well-known method to increase cerebral perfusion (Federau et al. 2012) and to identify clinically relevant lesions (cysts, necrosis, tumors, ischemia (Federau et al. 2014)). Moreover, the IVIM perfusion fraction was shown to be prognostic for survival of patients with glioblastomas (Puig et al. 2016; Federau et al. 2017).

In spite of recent progress, IVIM imaging in the brain remains challenging. In-plane spatial resolutions of $1 \times 1 \text{ mm}^2$ or better are desirable to reduce partial voluming, especially from cerebro-spinal fluid, which in turn requires large acquisition matrices and correspondingly long readouts. In the presence of B_0 -induced inhomogeneities, signal dephasing and geometrical distortions occur (Farzaneh et al. 1990), which prompt for the use of techniques which reduce readout times. Although segmented methods such as SPLICE (Schick 1997) for example allow readout duration shortening per echo, they are not as time efficient as single-shot echo planar imaging (EPI). Moreover, spatial resolution and signal-to-noise ratio (SNR) is limited with SPLICE (Schick 1997). Since diffusion imaging in the brain requires time and SNR efficient image acquisition for full brain coverage and numerous diffusion-weighted images, parallel imaging in conjunction with single-shot EPI acquisition (Bammer et al. 2001) is preferred.

So far, parallel imaging with undersampling factors of 2 has been applied to shorten readout durations (Federau et al. 2012; Federau et al. 2014; Federau et al. 2017). Parallel imaging, however, leads to spatially-dependent noise amplification, which increases exponentially beyond a critical g-factor limit (Ohliger et al. 2003; Wiesinger et al. 2004). The g-factor penalty and the low base SNR of diffusion-weighted imaging data at high b-values have hence

¹ Published in: Spinner GR, Schmidt JFM, von Deuster C, Federau C, Stoeck CT, Kozerke S (2018) *Enhancing intravoxel incoherent motion parameter mapping in the brain using k-b PCA*. NMR in Biomedicine 31(12):e4008. doi:10.1002/nbm.4008.

compromised the use of parallel imaging with undersampling factors greater than 2.

Spatiotemporal regularization for MRI image reconstruction was presented with the k-t BLAST/k-t SENSE framework (Tsao et al. 2003) and treated more generally in (Liang 2007). The method presented in the first reference was later modified by employing a principal component analysis (PCA) (Pedersen et al. 2009). The proposed k-t PCA approach was also applied for parameter mapping applications (Petzschner et al. 2011). Other acceleration approaches which employ Compressed Sensing (Huang et al. 2012) or low-rank and sparsity constraints (Zhang et al. 2015; Zhao et al. 2015) were presented for parameter mapping approaches more recently. Model-based methods for reconstruction of undersampled diffusion-weighted imaging data have been proposed (Zhu et al. 2012; Welsh et al. 2013), however excluding the IVIM model.

The objective of the present work is to exploit signal correlations in space and along the diffusion encoding dimension jointly as part of a constrained image reconstruction approach. To this end, the k-t PCA framework (Pedersen et al. 2009) is adopted. In-vivo brain images and IVIM parameter maps of apparent diffusion, perfusion fraction and pseudo-diffusion are compared relative to parallel imaging and to fully sampled data in the case of retrospectively undersampled data. In addition, reconstruction results and IVIM parameter estimates are presented from prospectively undersampled data.

5.2 Methods

5.2.1 k-b PCA

In k-b PCA, the acquisition of a set of diffusion-weighted images is undersampled using a sheared grid in k-b space in analogy to k-t undersampling (Tsao et al. 2003; Pedersen et al. 2009) as illustrated in Figure 5.1: each k-space is acquired using a Cartesian grid with regular undersampling in phase encoding direction of the outer k-space and fully acquired “training data” profiles around the center of k-space. While the latter remain at the same position in k-space for all images, the outer profiles are shifted by a certain number of lines as a function of diffusion weighting index “b” (corresponding to a certain diffusion weighting strength and direction). As a result of the undersampling approach, a “sheared” grid in k-b space is prescribed. The resulting net undersampling factor R depends on the nominal undersampling factor R_{nominal} of the regularly undersampled outer k-space and the training matrix size.

During reconstruction, the image estimates are first Fourier transformed along the b-dimension into the Fourier reciprocal spatial-frequency (x - f_b) space: together with the shift in k-space of the sheared grid, this results in separation of the object aliases. Then, principal component analysis (PCA) of the reciprocal x - f_b space is performed to reduce data dimensionality by decomposing the signals into the product of spatially dependent weights and b-value dependent basis functions. The most relevant components which explain most of the data variance can then be retained, while additional ones which contain mainly noise can be attenuated as done here via a Tikhonov regularization (which corresponds to a Gaussian prior on the pc coefficients).

Regularization of the inverse problem is based on low-resolution, fully sampled training data. Since k-b PCA is a least-squares problem, a closed form of the regularized ordinary least-squares estimator exists (Pedersen et al. 2009). Here the problem is rewritten as an optimization problem of a regularized system of linear equations as in (Schmidt et al. 2014):

$$\underset{\mathbf{i}}{\operatorname{argmin}} \|\mathbf{E}\mathbf{i} - \mathbf{d}\|_2^2 + \lambda \left\| \left({}^{x-PC}\mathbf{M} \right)^{-1} \mathbf{B}_{f_b \rightarrow PC} \mathbf{F}_{b \rightarrow f_b} \mathbf{i} \right\|_2^2 \quad (5.1)$$

where \mathbf{E} is the forward encoding operator including coil sensitivities, spatial Fourier transform and k-space undersampling, \mathbf{i} is the image estimate and \mathbf{d} captures the measured data. Coil sensitivities are acquired prior to IVIM imaging using a standard vendor-specific gradient echo sequence using the body coil and surface coils. The L_2 regularization uses the covariance matrix of the low-resolution training data in spatio-principal component space ${}^{x-PC}\mathbf{M}$. The off-diagonal elements of ${}^{x-PC}\mathbf{M}$ are set to zero for numerical stability and to prevent noise enhancement (Schmidt et al. 2014). Accordingly, the image estimate is first Fourier transformed along the b-dimension ($\mathbf{F}_{b \rightarrow f_b}$), then undergoes a pc decomposition ($\mathbf{B}_{f_b \rightarrow PC}$) along the same dimension before multiplying with the weighting matrix. All principal components were used for reconstruction. The regularization strength is controlled via the regularization parameter λ . Note that the LSQ ridge regression estimate corresponds to the maximum-a-posteriori estimate of a posterior distribution combining data likelihood with Gaussian error terms and a Gaussian prior using the low-resolution training data.

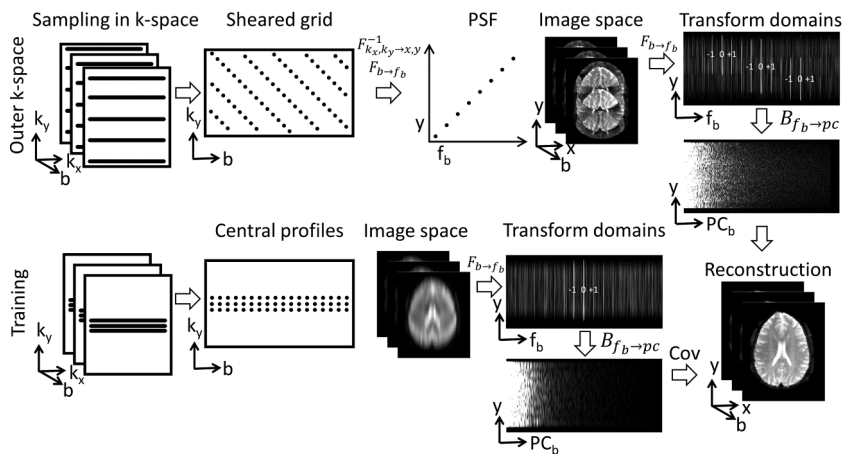


Figure 5.1: *k-b* PCA reconstruction scheme. Top row: outer *k*-space is sampled in a regularly undersampled Cartesian pattern. In addition, the sampling grid is shifted by some lines from one image to the next one. This results in a “sheared grid” along the *b*-dimension. After (inverse) Fourier transformation in *k*-space and along *b*-dimension a sheared point spread function (PSF) results. This leads to a separation of the object aliases of the undersampled data after Fourier transformation into the reciprocal spatio-frequential space: the DC peaks (marked as “0”) and the closest prominent positive and negative Fourier coefficients (marked as “+1” and “-1” respectively) are separated in the Fourier transform domain. The image reconstruction then uses principal component analysis (PCA) of the undersampled data for data dimensionality reduction. Bottom row: the central *k*-space profiles are acquired in every acquired image. This low-resolution estimate of the image is then also transformed into the Fourier reciprocal space (note the non-aliased representation) and subsequently transformed using PCA into spatial-principal component space. The corresponding covariance (“Cov”) matrix is used as weighting matrix in the regularization of the reconstruction. The central training lines are also used in the data consistency part of the reconstruction.

In *k-b* PCA, all acquired data including the diffusion encoding directions, *b*-values and signal averages was concatenated in acquisition order to populate the “*b*” dimension. Following previous work (Schmidt et al. 2014), *k-b* PCA was implemented using a diagonal pre-conditioner. The measured data was normalized by dividing data by the maximum magnitude of the image

magnitudes averaged along the b-dimension to allow for a fixed regularization parameter $\lambda=10^{-4}$ across different acquired data sets.

5.2.2 CG-SENSE

For comparison, parallel imaging reconstruction as employed so far in IVIM parameter mapping (Federau et al. 2012; Federau et al. 2014; Federau et al. 2017) is performed using the standard conjugate-gradient (CG) method (Pruessmann et al. 2001):

$$\underset{\mathbf{i}}{\operatorname{argmin}} \|\mathbf{E}\mathbf{i} - \mathbf{d}\|_2^2 \quad (5.2)$$

with encoding matrix \mathbf{E} , acquired k-space data \mathbf{d} and image estimate \mathbf{i} . For SENSE parallel imaging as in Equation (5.2), only the data consistency part of Equation (5.1) is used.

Both methods (k-b PCA and CG-SENSE) were deployed in Matlab (Mathworks, Natick, USA). A fixed number of 60 iterations was used on standard PC hardware (2.9 GHz, 16 GB RAM).

5.2.3 In-vivo measurements

Fully sampled data from 11 healthy volunteers (3 males, 8 females, age: 27 ± 4 years) without prior history of neurological or vascular disorders was obtained using a 3T Philips Achieva scanner (Philips Healthcare, Best, the Netherlands) equipped with an 8-channel head coil. Written informed consent was obtained from all subjects prior to imaging. The study protocol was approved by the ethics committee of the Canton of Zurich. Consent included imaging as well as publication of anonymized data. Imaging parameters were: single-shot 2D EPI readout with 181 phase-encodes, field-of-view $218 \times 180 \times 65 \text{ mm}^3$, partial Fourier factor 0.65, 9 slices, slice gap 2.5 mm, voxel size $1.2 \times 1.2 \times 5 \text{ mm}^3$, echo time $TE=81 \text{ ms}$, repetition time $TR=4 \text{ s}$. For diffusion weighting, a standard unipolar diffusion weighting sequence was used (Stejskal and Tanner 1965). Spectral pre-saturation with inversion recovery for fat suppression was employed. Diffusion encoding b-values were (Federau et al. 2012; Federau et al. 2014): 0, 10, 20, 40, 80, 110, 140, 170 and 200 to 900 in steps of 100 s/mm^2 . 4 signal averages for each diffusion weighting strength and direction were acquired equally distributed across the measurement time. Total scan time was 24 min 24 s for the fully sampled data. In order to estimate SNR in-vivo as presented in (Nordmeyer-Massner et al. 2009), noise samples were acquired by performing an additional scan without gradients and RF excitation.

Prospectively undersampled data (5 volunteers: 2 males, 3 females, age: 28 ± 8 years) was acquired with 33 phase encodes, field-of-view $235 \times 180 \times 65 \text{ mm}^3$, no partial Fourier acquisition, echo time $TE=61 \text{ ms}$, while the other parameters remained the same as for retrospective undersampling. The effective undersampling factor across all acquired images was 6.08, also using 9 training profiles. An additional IVIM dataset with the same geometry but partial Fourier acquisition (partial Fourier factor 0.62) of a fully sampled k-space with 199 phase encodes and an echo time $TE=74 \text{ ms}$ was acquired for comparison.

5.2.4 Data processing

Pre-processing of the raw data was performed using MRRecon (GyroTools, Winterthur, Switzerland) and encompassed a ringing filter, removal of oversampling and a homodyne filter to account for partial Fourier acquisition used in the fully sampled images. The same software was also used for the processing (reconstruction, smoothing and masking) of the sensitivity maps.

Sheared grid undersampling in k-b space was applied onto data to extract undersampled data for net reduction factors R ranging between 2 and 6 followed by k-b PCA and CG-SENSE reconstruction. The 9 central profiles were retained and served as training data in k-b PCA, while the outer k-space was undersampled 2- to 8-fold (R_{nominal}). The influence onto reconstruction accuracy was investigated by varying the regularization parameter, the number of training lines, the number of principal components and the number of signal averages, while the outer k-space was 8-fold undersampled. In the case of prospective data undersampling, gradient blips with varying strengths were used along phase encoding direction to acquire the k-space in the described sheared grid trajectory in a single-shot readout. Identical sampling patterns were used for both k-b PCA and CG-SENSE. Images were registered using a dedicated group-wise image registration method (Vishnevskiy et al. 2017) employing total variation displacement regularization and a PCA based image similarity metric (Huizinga et al. 2016) to correct for in-plane residual geometric inconsistencies due to volunteer motion and eddy current induced distortions either before reconstruction (retrospective undersampling) or thereafter (prospective undersampling). For error analysis, the brain was automatically segmented using active contours (Chan and Vese 2001). The ventricles, sulci and other CSF-rich areas were cut out from the region-of-interest (ROI) by performing an IVIM fit to the fully sampled reference or k-b PCA reconstructed images in the case of prospective undersampling. Voxels with $D \geq 2 \cdot 10^{-3} \text{ mm}^2/\text{s}$ and $f \geq 30\%$ were excluded as illustrated in Figure 5.2.

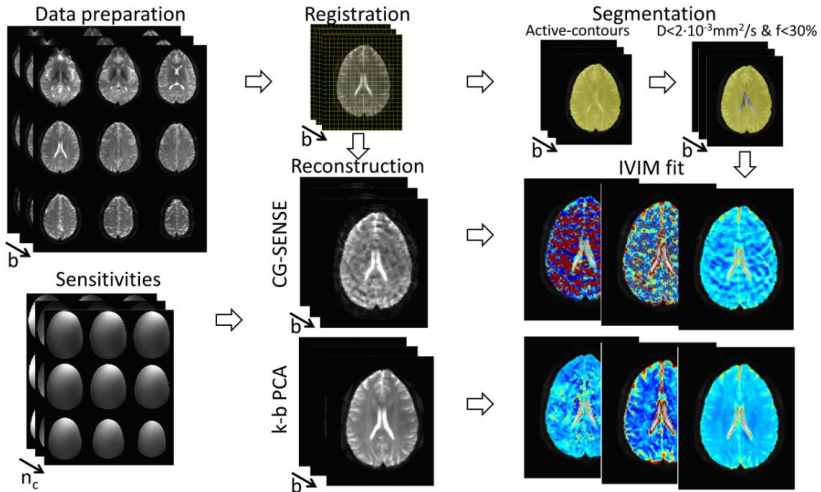


Figure 5.2: Post-processing workflow. After signal corrections (offset corrections, oversampling removal) and homodyne filtering (if fully sampled data using partial Fourier acquisition is processed), data is registered and passed on to the reconstruction algorithms together with sensitivities of the n_c surface coils measured in an additional scan. Prospectively undersampled data was first reconstructed and then registered. Error analysis of the reconstruction is performed on the segmented brain. Segmentation is achieved using active contours and an IVIM fit with threshold parameters to segment the brain without CSF-rich areas such as the ventricles.

5.2.5 Parameter mapping

For IVIM parameter mapping, the two-compartment IVIM model (Le Bihan 1988) was used:

$$S(b) = S_0 \left[f \cdot \exp(-bD^*) + (1-f) \cdot \exp(-bD) \right], \quad (5.3)$$

where $S(b)$ denotes the measured signal as a function of b-value, S_0 the signal without diffusion weighting ($b=0$ s/mm²), D the diffusion constant, f the perfusion fraction and D^* the pseudo-diffusion constant. A segmented least-squares fitting approach (Notohamiprodjo et al. 2015; Spinner et al. 2017) was used assuming the contribution of the perfusion to reach a maximum of $f/(1-f)$ at $b=0$ s/mm² and to drop to negligible values for b-values $b \gg b_{\text{split}}$.

Accordingly, high b -values ($b \geq b_{\text{split}} = 300 \text{ s/mm}^2$) were fitted to a mono-exponential diffusion-only model according to:

$$S(b) \approx S_0 \cdot (1 - f) \cdot \exp(-bD) = S_{\text{int}} \cdot \exp(-bD) \quad (5.4)$$

In the second step of the segmented regression, the perfusion related parameters f and D^* were estimated using the predetermined diffusion coefficient D and the mono-exponential intercept S_{int} while taking into account data from all b -values: by substituting $S_0 = S_{\text{int}} / (1 - f)$ in Equation (5.3), the signal model reads accordingly:

$$\begin{aligned} S(b) &= S_0 \left[f \cdot \exp(-bD^*) + (1 - f) \cdot \exp(-bD) \right] \\ &= S_{\text{int}} \left[\frac{f}{1 - f} \cdot \exp(-bD^*) + \exp(-bD) \right] \end{aligned} \quad (5.5)$$

This approach avoids the usage of images without diffusion weighting ($b=0 \text{ s/mm}^2$) which have a slightly different contrast due to spoiler gradients instead of diffusion gradients. The non-linear regression was implemented using a quasi-Newton (BFGS) algorithm in Matlab (Mathworks, Natick, MA) and constrained with box constraints as in (Orton et al. 2014; Spinner et al. 2017):

$$\begin{aligned} 0 &\leq D \leq 2.5 \cdot 10^{-3} \text{ mm}^2/\text{s} \\ 0 &\leq f \leq 1 \\ 0 &\leq D^* \leq 25 \cdot 10^{-3} \text{ mm}^2/\text{s} \end{aligned} \quad (5.6)$$

Start values for the optimization were found by considering the logarithm of the magnitude data in a two-step approach as above and solving the linearized problems with a proprietary linear solver in Matlab.

5.2.6 Error estimation

A voxel-wise normalized root-mean-square error (nRMSE) was considered for both the reconstructed data and IVIM parameter estimates (\mathbf{x}):

$\text{nRMSE}(\mathbf{x}) = \sqrt{\|\mathbf{x} - \mathbf{x}_{\text{Ref}}\|^2 / \|\mathbf{x}_{\text{Ref}}\|^2}$. The fully sampled data or the derived IVIM parameters served as reference (\mathbf{x}_{Ref}). The median and interquartile ranges (difference between percentile 75 and 25; covering 50% of the data of a Normal distribution) were evaluated across all segmented voxels considering all acquired slices of all volunteers. These percentile-based measures are used as

descriptive statistics in the following because of their robustness against outliers.

5.3 Results

5.3.1 Reconstruction error

Reconstructed magnitude images using CG-SENSE exhibit visible undersampling artifacts and noise amplification for $R \geq 2.73$, while k-b PCA shows no visible artifacts (Figure 5.3) as highlighted in the corresponding difference images. The influence of various settings onto the reconstruction error for the highest undersampling factor is displayed in Figure 5.4: the regularization parameter λ exhibits a local error minimum of $3.48 \pm 3.69\%$ at $\lambda = 10^{-4}$; reduction of the number of training profiles causes the error to increase moderately from $3.23 \pm 3.42\%$ (13 profiles) to $4.75 \pm 4.99\%$ (5 profiles); the error increases noticeably if the number of principle components (pc) is reduced below 16 from $4.70 \pm 5.41\%$ to $18.68 \pm 26.84\%$ (1 pc) and the error remains below 5% if only the first signal average is used for reconstruction ($4.25 \pm 4.83\%$ error using the first average only; $3.68 \pm 3.89\%$ error using all 4 averages).

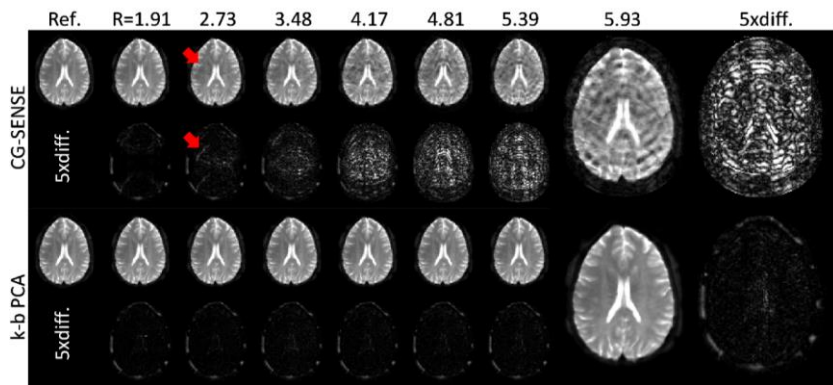


Figure 5.3: Retrospectively undersampled and reconstructed $b=0$ s/mm² magnitude images. Comparison of reconstruction results from retrospectively undersampled $b=0$ s/mm² data for CG-SENSE and k-b PCA and corresponding difference maps (5-fold amplified) relative to the fully sampled reference. Undersampling artifacts are readily apparent for CG-SENSE starting at $R=2.73$ (red arrows) and become more prominent with increasing undersampling factor. In contrast, in the proposed k-b PCA method artifacts are well attenuated up to the highest undersampling factor investigated, which is shown magnified on the right.

The nRMSE relative to the fully sampled references across all volunteers and slices is shown in Figure 5.4: $1.76 \pm 2.43\%$ ($R=1.91$) up to $25.28 \pm 25.83\%$ ($R=5.93$) for CG-SENSE and 2.45 ± 2.52 ($R=1.91$) up to $3.48 \pm 3.69\%$ ($R=5.93$) for k-b PCA.

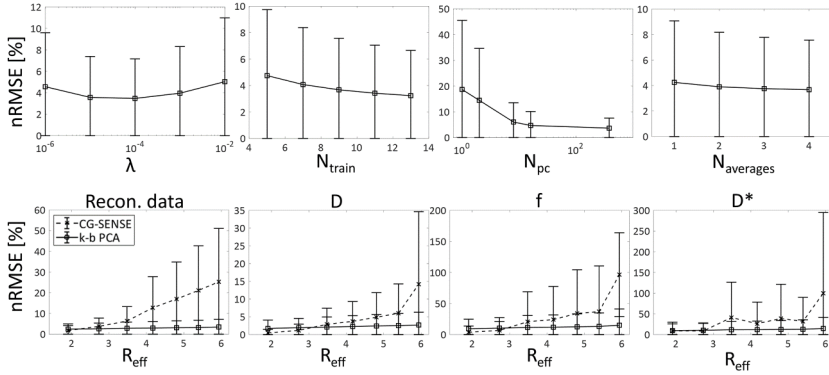


Figure 5.4: Reconstruction error. Reconstruction error (boxes/crosses: median, error bars: interquartile range) of retrospectively undersampled data across all segmented voxels as normalized root-mean-square error (nRMSE), relative to the fully sampled data. The top row shows the reconstruction error depending on various reconstruction settings at the highest undersampling factor investigated (8-fold undersampling of the outer k -space, corresponding to a net undersampling factor of 5.93 using 9 training profiles). Irrespective of the chosen parameters, the error remains below or equal 5% as long as at least 16 principal components are used. The lower row shows the error versus net undersampling factor of the reconstructed data and the IVIM parameter estimates. The reconstruction error of CG-SENSE increases rapidly while the k-b PCA method remains below 5%. A similar performance is observed for the diffusion coefficient D . The perfusion parameters (f and D^*) show a higher error for undersampling factors $R \geq 3$ if CG-SENSE is used compared to k-b PCA, which yields errors remaining below or equal 15% even at the highest investigated undersampling factor.

The average SNR across all acquired voxels of the 11 volunteers was 24.45 ± 15.74 for a single-shot image of the fully sampled data.

5.3.2 IVIM parameter estimation error

The IVIM parameter estimation errors versus net undersampling factor are provided in Figure 5.4. For undersampling factors $R \leq 3$, CG-SENSE yields lower or comparable errors relative to the proposed method ($0.49 \pm 0.96/1.74 \pm 2.37\%$

for D , $3.80 \pm 9.92 / 9.42 \pm 15.39\%$ for f and $9.07 \pm 20.94 / 9.64 \pm 16.34$ for D^* at $R=1.91$ for CG-SENSE/k-b PCA), but is outperformed at undersampling factors $R > 3$. At the highest undersampling factor investigated ($R=5.93$) the corresponding nRMSEs of the IVIM parameters are: $14.21 \pm 20.44 / 2.71 \pm 3.60\%$ for D , $96.56 \pm 67.44 / 15.14 \pm 26.13\%$ for f and $99.99 \pm 195.11 / 14.76 \pm 26.55\%$ for D^* at $R=5.93$ for CG-SENSE/k-b PCA.

The IVIM parameter estimates derived from CG-SENSE reconstruction in Figure 5.5 show artifacts and noise amplification for $R \geq 3.48$ in all IVIM parameters, while k-b PCA derived parameters remain nearly artifact free up to $R=5.93$. With k-b PCA, parameters D and f do not exhibit visible artifacts up to the highest examined effective undersampling factor of $R=5.93$. Considering the perfusion fraction f , undersampling factors equal or greater than 3.48 exhibit increasing artifact and noise levels when using CG-SENSE. In contrast, with the proposed method, noise amplification is minimal even at the highest undersampling factor tested. The pseudo-diffusion coefficient D^* shows increasing artifacts and noise with CG-SENSE for $R \geq 2.73$, while the proposed method reduces the artifact levels to a noise-like level.

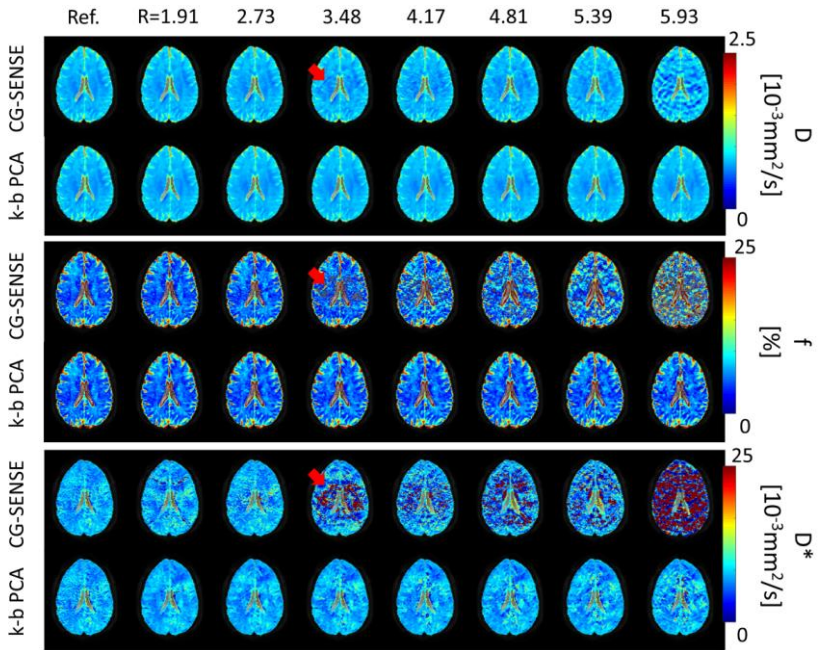


Figure 5.5: IVIM parameter maps. IVIM parameter maps for the fully sampled reference (Ref.) and all investigated net undersampling factors of CG-SENSE and k-b PCA using retrospectively undersampled data. Noise amplification of CG-SENSE is readily visible for $R \geq 3.48$ in all IVIM parameters (red arrows) with severe undersampling artifacts at the highest undersampling factor tested. The proposed reconstruction technique (k-b PCA) does not exhibit visible noise amplification or artifacts for the diffusion coefficient D and perfusion fraction f . The pseudo-diffusion coefficient D^* shows artifacts for the highest undersampling factor investigated.

5.3.3 Prospectively undersampled data

An example magnitude image of the prospectively 6-fold undersampled non diffusion-weighted ($b=0 \text{ s/mm}^2$) single-shot k-b PCA reconstructed image is shown together with a corresponding fully sampled acquisition in Figure 5.6. This particular axial brain slice geometry at the level of the basal ganglia exhibits typical B_0 -induced off-resonance effects due to air-tissue interfaces. The relatively long EPI readout of the fully sampled acquisition hence shows several visible geometric distortions and signal smearing. These artifacts are reduced in the k-b PCA acquisition due to the shorter readout. Additional reconstructed

$b=0$ s/mm² single-shot magnitude images of prospectively 6-fold (net) undersampled data can be found in Figure 5.7 of the Appendix, displaying k-b PCA reconstructed results of all acquired slices in a volunteer.

Example IVIM maps are qualitatively similar to the fully sampled reference data as demonstrated in Figure 5.6.

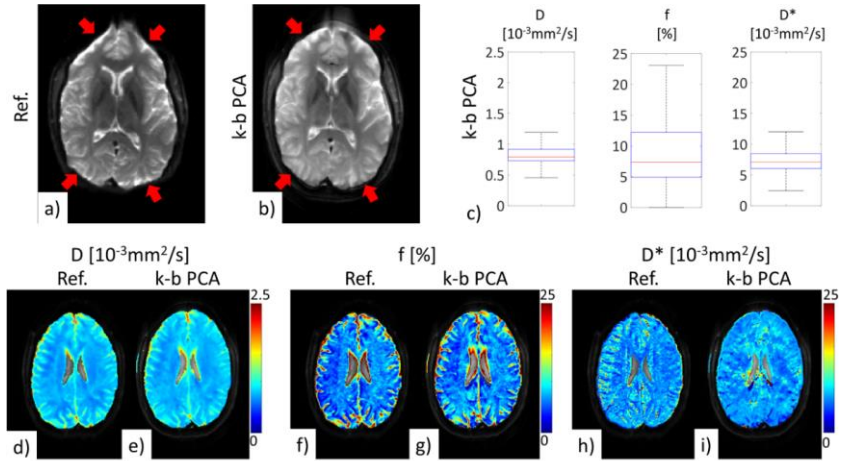


Figure 5.6: Prospectively undersampled data. The magnitude image ($b=0$ s/mm²) of the fully sampled (Ref., 199 phase encodes, $TE=74$ ms) acquisition (a) exhibits severe susceptibility artifacts due to a long EPI readout (red arrows), while the undersampled (net undersampling factor $R=6.08$, 33 phase encodes, $TE=61$ ms) and reconstructed magnitude using k-b PCA (b) shows drastically reduced artifacts (red arrows). The boxplot (red line=median, blue box=percentile 75 and 25, whiskers=1.5x interquartile range) shows the IVIM parameter ranges of the prospectively undersampled ($R=6.08$) data (c). Example IVIM parameter maps of the fully sampled reference (Ref.) and k-b PCA reconstructed images display the diffusion coefficient D (d, e), the perfusion fraction f (f, g) and pseudo-diffusion coefficient D^* (h, i).

5.3.4 IVIM parameter estimates

The averages across all acquired voxels of the IVIM parameters are: $0.79\pm 0.20/0.79\pm 0.18\cdot 10^{-3}$ mm²/s for D , $8.46\pm 10.16/7.35\pm 7.27\%$ for f and $6.90\pm 6.53/7.11\pm 2.39$ for D^* of the fully sampled data (11 volunteers) /prospectively 6-fold undersampled and k-b PCA reconstructed data (additional 5 volunteers).

IVIM parameter estimates of the fully sampled reference data (11 volunteers), CG-SENSE and k-b PCA reconstructed images can be found in Table 5.1 in the Appendix. For increasing undersampling factor, all IVIM parameter estimates are increasing, especially with CG-SENSE.

5.4 Discussion

In this study, k-b PCA was proposed and applied to IVIM data acquisition in the brain. It has been shown that reconstruction errors are reduced with the proposed method compared to CG-SENSE parallel imaging for $R > 3$. Accordingly, IVIM parameter estimation was notably improved with the proposed technique permitting a maximum net undersampling factor of 6 and hence reduced image distortions in single-shot imaging.

At $R < 3$, the better performance of CG-SENSE relative to k-b PCA is attributed to the data-driven regularization used in k-b PCA. The regularization weight was kept constant for all undersampling factors tested in this work to simplify the approach and avoid data-specific tuning in practice. It is perceivable that a lower regularization weight at low undersampling factors would help to reduce errors, which, however, was not used here to keep the method simple. However, for higher undersampling factors $R \geq 3$, the regularization of the proposed approach can effectively reduce the variance of the image estimator and hence noise, leading to superior reconstruction relative to parallel imaging, i.e. CG-SENSE.

The presented reconstruction technique operates in the spatio-principal component space and benefits from the sparsity of the data in this Fourier and PCA transformed data representation. This type of ridge regression therefore exploits similarities present in the data along the diffusion weighting dimension. In general, however, an optimal experiment design of the IVIM model with regard to the set of b-values and/or diffusion weighting directions to be acquired based on Monte Carlo simulation (Lemke et al. 2011) or Fisher Information (Purvis et al. 2015) does not necessarily coincide with a sampling pattern which yields minimal sparsity in a k-b approach and hence optimal reconstruction quality.

The reference dataset for retrospective undersampling was generated with partial Fourier acquisition and a homodyne filter. This resulted in a Hermitian symmetric outer k-space where no data was acquired during readout, which is a limitation of the dataset used for prospective undersampling.

Along the lines of the present study, which takes advantage of the similarity along the diffusion encoding dimension, other alternative approaches are

possible. To this end, Compressed Sensing (Lustig et al. 2008) based approaches (Lustig et al. 2006; Huang et al. 2012; Zhang et al. 2015; Zhao et al. 2015) may be used. While these methods do not require fully sampled training data, they also rely on sparse representations of the data. However, these LASSO type regression (Tibshirani 1996) methods are non-linear and hence optimization is more challenging. In addition, a potential risk exists with more “aggressive” priors/regularizations to over-smooth small features which are near the noise level if the undersampling factor is too high (Knoll et al. 2015): the L_1 regularization in Compressed Sensing corresponds to a Laplace prior in a Bayesian framework. Compared to the Gaussian regularization employed in the proposed method, a Laplacian distribution promotes probability stronger around the center of the distribution and hence causes a stronger suppression of higher order components of the sparse basis, which can lead to over-smoothing.

The proposed k-b PCA method requires a certain number of training profiles to capture the relevant object features using the basis transform. The usage of 9 training profiles in this study did not result in any relevant loss of detail for the range of undersampling factors employed. If, however, acceleration factors beyond those reported in this work were used, the reconstructed images would start suffering from missing details. In this case, more training profiles are required to constrain the reconstruction problem further. Both aspects, the number of training profiles and the degree of k-space undersampling limit the proposed approach to about 10-fold nominal undersampling in dynamic imaging applications (Schmidt et al. 2014) and 8-fold nominal undersampling in parameter mapping (Petzschner et al. 2011) when using 9 to 11 training profiles typically.

Another alternative reconstruction approach casts MR signal relations into the forward model as proposed for parameter mapping, also in diffusion MRI (Zhu et al. 2012; Welsh et al. 2013; Knoll et al. 2015). However, since the IVIM model describes signal magnitudes only, the image phase needs also to be estimated or acquired from a low-resolution training set. Such an approach is permissible if the object phase can be represented using low-order spatial harmonics. If, however, the object phase varies locally as in or near vessels, for example, optimization needs to employ separate magnitude and phase regularization (Zhao et al. 2012; Santelli et al. 2016). The proposed k-b PCA method is able to resolve local phase variations, as shown for k-t PCA accelerated flow measurements in the neck for example (Knobloch et al. 2014). Moreover, the optimization procedure in model-based approaches suffers from the intrinsic non-linearity of the problem, the non-vanishing covariance among the variables and their different scaling. To this end, the linear quadratic approach

presented here provides robust optimization performance in an orthogonal principal component basis.

In practice, IVIM parameter estimation is error-prone and has resulted in various regularized regression methods (Orton et al. 2014; Spinner et al. 2017). These latter methods rely on homogeneous tissue in terms of diffusion and perfusion properties. In the brain, however, different types are present, such as gray matter, white matter and CSF-rich areas. Moreover, IVIM applications in the brain have so far relied on a voxel-wise least-squares fit (Federau et al. 2012; Federau et al. 2014; Federau et al. 2017) and hence this regression method is deemed applicable for the analysis of the presented image reconstruction method. The small deviation of the IVIM parameters of the prospectively undersampled data and the fully sampled reference can be attributed to the slightly different echo times.

5.5 Conclusion

Constrained reconstruction using k-b PCA improves IVIM parameter mapping from undersampled data when compared to CG-SENSE reconstruction. Accordingly, k-b PCA permits reduction of readout durations, associated EPI artifacts and echo time beyond the limits of parallel imaging. Alternatively, it potentially allows reducing partial voluming through increased spatial resolution in the brain.

5.6 Appendix

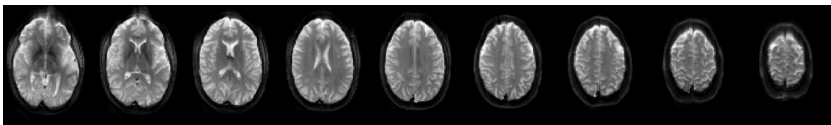


Figure 5.7: Magnitude images of all acquired slices. Single-shot $b=0$ s/mm² magnitude images reconstructed of prospectively undersampled ($R=6.08$) and k-b PCA reconstructed data, displaying all acquired slices in a volunteer. Note the relative absence of typical long readout EPI artifacts such as distortions, signal attenuation or build-up near air-tissue interfaces.

	Ref.		R=1.91	2.73	3.48	4.17	4.81	5.39	5.93
D [10 ³ mm ² /s]	0.77±0.18	CG-SENSE	0.77±0.18	0.77±0.18	0.78 ±0.19	0.77±0.19	0.78±0.19	0.78±0.20	0.81±0.31
		k-b PCA	0.77±0.16	0.77±0.16	0.78±0.16	0.78±0.16	0.78±0.16	0.78±0.16	0.78±0.16
f [%]	6.20±6.62	CG-SENSE	6.12±6.87	6.37±6.77	6.17±8.66	7.26±8.70	7.14±9.45	8.14±9.29	8.96±16.26
		k-b PCA	6.18±7.04	6.22±7.06	6.28±7.15	6.29±7.16	6.32±7.17	6.36±7.20	6.50±7.36
D* [10 ⁻³ mm ² /s]	6.96±1.98	CG-SENSE	7.00±2.62	7.00±2.35	7.32±7.29	7.03±4.32	7.23±6.68	7.08±4.93	11.33±22.15
		k-b PCA	6.91±1.55	6.93±1.62	6.95±1.74	6.95±1.76	6.96±1.8	6.96±1.86	7.00±2.05

Table 5.1: IVIM parameter estimates (median±interquartile range) of the fully sampled data from 11 volunteers together with IVIM estimates after reconstructing with CG-SENSE and k-b PCA for all investigated net undersampling factors

Chapter 6

Bayesian intravoxel incoherent motion parameter mapping in the human heart²

6.1 Background

Cardiac IVIM may allow to delineate infarcted and ischemic areas showing good agreement with late-gadolinium enhanced imaging (Deux et al. 2011; Laissy et al. 2013). Moreover, IVIM may enable the assessment of chronic and acute ischemia (von Deuster et al. 2015) as well as conditions related to microvascular obstruction of the myocardium (Ismail et al. 2014).

Despite recent progress, in-vivo cardiac diffusion weighted imaging still remains challenging due to cardiac and respiratory motion. Additionally, low signal-to-noise ratio (SNR) and long scan times are major impediments to a wider acceptance in a clinical setting. Motion induced signal loss in spin-echo (SE) based cardiac diffusion weighted imaging has been addressed by first-order motion compensated diffusion gradient designs in conjunction with careful cardiac trigger delay selection (Gamper et al. 2007) and more recently by second-order motion compensation (Nguyen et al. 2014; Welsh et al. 2015; Stoeck et al. 2016). Initial results of the application of second-order motion compensation for IVIM acquisitions during systole have previously been presented in a porcine model (von Deuster et al. 2015). For diastolic imaging, time-shifted triggering and dedicated post processing using principal component analysis (PCA) filtering in combination with temporal maximum intensity projection (PCATMIP) has been proposed (Pai et al. 2011; Rapacchi et al. 2011; Delattre et al. 2012; Moulin et al. 2016).

Experimentally, cardiac IVIM parameters were initially reported for the in-vivo canine heart (Callot et al. 2003). The measured diffusion weighted signal agreed well with the bi-exponential IVIM model with reduced signal decay in the absence of perfusion post-mortem (von Deuster et al. 2015).

IVIM parameter maps of various organs such as brain or heart (Federau et al. 2014; Moulin et al. 2016) are typically of noisy appearance. Due to the non-

² Published in: Spinner GR, von Deuster C, Tezcan KC, Stoeck CT, Kozerke S (2017) *Bayesian intravoxel incoherent motion parameter mapping in the human heart*. Journal of Cardiovascular Magnetic Resonance 19(1):85. doi: 10.1186/s12968-017-0391-1

linearity and bad conditioning of the regression problem, the perfusion related parameters are estimated with considerable error at typical SNR values as shown in (Federau et al. 2015; Wu et al. 2015). Besides modifying the data acquisition protocol to obtain higher SNR at the expense of lower spatial resolution and/or longer scan time, group analysis of longitudinal data of individuals incorporating both intra- and inter-subject variations (Huang et al. 2016) or regional smoothing (Rheinheimer et al. 2012) have been proposed. These approaches are, however, limited by the necessity of repeated measurements across multiple independent subjects or loss of spatial resolution and increased partial voluming, respectively.

To address the SNR limitation of IVIM analysis, a hierarchical Bayesian data analysis framework has been presented by Orton et al. (Orton et al. 2014) and demonstrated for liver application. Using this approach, information across the region-of-interest is taken into account for voxel-wise parameter inference. Parameter estimation is performed using a posterior distribution combining data likelihood and histogram prior. This combination enables effective denoising of parameter maps with reduced parameter estimation error.

The objective of the present work was to implement and assess Bayesian shrinkage prior (BSP) inference for IVIM parameter mapping of the in-vivo human heart and compare its performance to segmented least-squares (LSQ) fitting.

6.2 Theory

6.2.1 Intravoxel incoherent motion

The IVIM model (Le Bihan 1988) in Equation (6.1) describes signal magnitude of diffusion weighted images as bi-exponential decay. In addition to diffusion induced signal attenuation, a second compartment of perfusion induced pseudo-diffusion is taken into account:

$$S(b) = S_0 \left[F \cdot \exp(-bD^*) + (1-F) \cdot \exp(-bD) \right] \quad (6.1)$$

where $S(b)$ describes the measured signal as a function of b-value, S_0 the signal without diffusion weighting ($b=0$ s/mm²), D the diffusion constant, F the perfusion fraction and D^* the pseudo-diffusion constant. Note that capital F is used for the perfusion fraction to be consistent with the notation in (Orton et al. 2014).

6.2.2 Least-squares fitting

For least-squares fitting, a segmented approach (Notohamiprodo et al. 2015) is implemented assuming the contribution of the perfusion to reach a maximum of $F/(1-F)$ at $b = 0$ s/mm² and to drop to negligible values for b -values $b \gg b_{\text{split}}$. In practice, high b -values ($b \geq b_{\text{split}} = 200$ s/mm²) are fitted to a mono-exponential diffusion-only model:

$$S(b) \approx S_0 \cdot (1-F) \cdot \exp(-bD) = S_{\text{int}} \cdot \exp(-bD) \quad (6.2)$$

If a non-diffusion weighted image S_0 is not available, the intercept S_{int} does not allow for a direct calculation of the perfusion fraction F as described in (Notohamiprodo et al. 2015), but $S_{\text{int}} = S_0(1-f)$ enables to eliminate S_0 in the bi-exponential model. In the second step of the segmented regression, the perfusion related parameters F and D^* are estimated using the predetermined diffusion coefficient D and the mono-exponential intercept S_{int} while taking into account all considered b -values. By substituting S_0 in Equation (6.1), the signal model reads accordingly:

$$\begin{aligned} S(b) &= S_0 \left[F \cdot \exp(-bD^*) + (1-F) \cdot \exp(-bD) \right] \\ &= S_{\text{int}} \left[\frac{F}{1-F} \cdot \exp(-bD^*) + \exp(-bD) \right] \end{aligned} \quad (6.3)$$

The non-linear regression is implemented using an interior-point algorithm in Matlab (Mathworks, Natick, MA) and constrained by an inequality together with box constraints as in (Orton et al. 2014):

$$\begin{aligned} D &\leq D^* \\ 4.5 \cdot 10^{-5} &\leq D \leq 1.8 \cdot 10^{-2} \text{ mm}^2/\text{s} \\ 0.0005 &\leq F \leq 0.9995 \\ 3.4 \cdot 10^{-4} &\leq D^* \leq 1.0 \cdot 10^{-1} \text{ mm}^2/\text{s} \end{aligned} \quad (6.4)$$

6.2.3 Bayesian shrinkage prior inference

For Bayesian inference as presented in (Orton et al. 2014), a marginalized data likelihood is used along with a multivariate Gaussian histogram prior combined with Jeffrey's prior (Jeffreys 1946). The approach is implemented using a

Markov chain Monte Carlo (MCMC) method as described in the Appendix 1 (Chapter 6.7).

6.3 Methods

6.3.1 Computer simulations

IVIM parameter ranges were simulated according to values reported for the in-vivo heart (von Deuster et al. 2015; Moulin et al. 2016). The diffusion coefficient was set to $D = 1.5 \cdot 10^{-3}$ mm²/s, while three perfusion regimes (low, intermediate, high) were considered ($F/D^* = 10/10, 15/15, 20/20$ %/ 10^{-3} mm²/s). The simulated SNRs ranged from 10 to 100 in steps of 10 and from 100 to 200 in steps of 25. Gaussian distributed noise was added followed by magnitude detection to yield Rician distributed noise mimicking the noise distribution of MR magnitude images. A single Monte Carlo simulation run consisted of 1000 IVIM data sets with b-values as used in the in-vivo part of this study: 20 to 100 s/mm² in steps of 20 s/mm², 125 to 200 s/mm² in steps of 25 s/mm², 250 and 300 s/mm². Both bias $\left| \langle \hat{\mathbf{p}} \rangle - \mathbf{p}_{\text{Ref}} \right| / \mathbf{p}_{\text{Ref}}$ and variation $\hat{\sigma}_{\mathbf{p}} / \mathbf{p}_{\text{Ref}}$ with $\mathbf{p} = D, F$ and D^* , \mathbf{p}_{Ref} the simulated parameter, $\langle \hat{\mathbf{p}} \rangle$ the mean estimate and $\hat{\sigma}_{\mathbf{p}}$ the standard deviation of the estimated parameters were calculated and are reported as relative errors. The simulation was repeated and resulting parameter estimation errors were averaged 100 times.

6.3.2 In-vivo measurements

Second-order motion compensated spine-echo (SE) diffusion weighted imaging (Welsh et al. 2015; Stoeck et al. 2016) was implemented on a 1.5T Philips Achieva System (Philips Healthcare, Best, The Netherlands), see Figure 6.1. Signal was received with a 5 channel cardiac receiver array. Written informed consent was obtained from all subjects prior to imaging. The study protocol was approved by the ethics committee of the Canton of Zurich. Consent included imaging as well as publication of anonymized data.

Data were acquired in eight healthy subjects without history of cardiac disease (6 female, 2 male, weight 64±8 kg, age 26±4 years, heart rate 64±9 beats/min, min/max heart rates: 51/81 beats/min) on two separate occasions. Prior to diffusion imaging, cine data with a temporal resolution of 10 ms were acquired in two chamber and short axis view orientations. Using the cine images, systolic quiescent time points were determined visually on a per subject basis.

Diffusion weighted imaging was performed during free-breathing in short-axis view orientation using single-shot EPI readout with the reduced field-of-view

(FOV) technique Local-Look (LoLo) (Feinberg et al. 1985). Slice tracking to account for breathing motion was controlled by a respiratory 1D navigator pencil beam placed on the right hemi diaphragm, accepting all data. A 1-3-3-1 binomial spectral-spatial excitation pulse for fat suppression (Meyer et al. 1990) was employed. Images were acquired with in-plane resolution: $2.4 \times 2.4 \text{ mm}^2$, slice thickness: 10 mm, one mid-ventricular slice, field of view (FOV): $230 \times 105 \text{ mm}^2$, acquired k-space lines: 43, TR/TE: 2 R-R/73 ms, flip angle: $81 \pm 1^\circ$ (heart rate dependent Ernst angle (Ernst 1966)), 8 signal averages and 6 vendor gradient optimized diffusion encoding directions. The applied diffusion encoding strengths included the values described in the previous sections (20 to 100 s/mm^2 in steps of 20 s/mm^2 , 125 to 200 s/mm^2 in steps of 25 s/mm^2 , 250 and 300 s/mm^2) together with 0 s/mm^2 . The trigger delay for the SE sequence was set to 25% peak systolic contraction (Stoeck et al. 2016) with a mean trigger delay of $78 \pm 3 \text{ ms}$. Acquisition of the 8 signal averages for each diffusion encoding strength and direction was equally distributed along the measurement. Total scan time was about 18 min at a heart rate of 60 beats per minute.

In-vivo SNR measurements were performed in each volunteer. To measure noise, the scans were repeated with radio-frequency and gradient pulses switched off. Sufficient time ($>10 \text{ s}$) was allowed between image and noise acquisition to ensure complete signal decay. SNR was determined for each voxel as described in (Nordmeyer-Massner et al. 2009).

Imaging in each subject was repeated in consecutive sessions separated by one week to assess intra-subject reproducibility.

In addition, diffusion data in an animal model of myocardial infarction was evaluated; see Appendix 2 for further details.

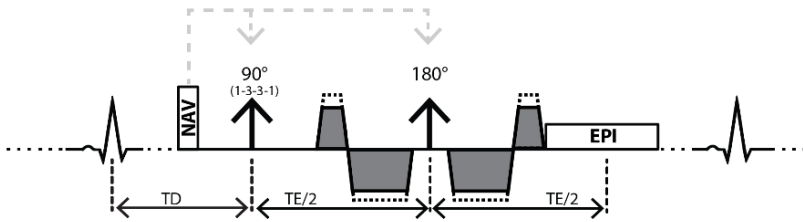


Figure 6.1: Sequence diagram. Spin-echo acquisition with second-order motion-compensated diffusion encoding gradients. Fat suppression is achieved by a 1–3–3–1 binomial spatial spectral excitation pulse. The excitation slab is tilted orthogonally with respect to the 180° pulse to allow for reduced field-of-view imaging. Prior to the diffusion weighting, a 1D–navigator pencil beam is used for automatic slice tracking by shifting the excitation and echo pulses. Various b -values are achieved by keeping timing constant while varying gradient strengths (dotted gradient trapezoids)

6.3.3 Data post-processing

For in-vivo IVIM parameter mapping, images were first registered using a dedicated group-wise image registration method (Vishnevskiy et al. 2017) employing total variation displacement regularization and a PCA-based image similarity metric (Huizinga et al. 2016) to correct for in-plane residual geometric inconsistencies. Afterwards, complex averaging (Scott et al. 2016) of the signal averages was performed. The IVIM parameters of both regression methods (LSQ and BSP) and SNR were determined upon manual masking the left ventricular myocardium. The same segmentation was used for both regression methods (LSQ and BSP). To avoid partial volume effects, voxels at the epi- and endocardial borders were excluded during the segmentation process and all voxels within the segmented ROI were used for further analysis. The image magnitudes were corrected for heart rate variations using recorded R-R intervals and published T_1 values of the myocardium (Messroghli et al. 2006). Figure 6.2 summarizes all post processing steps. IVIM analysis was performed on data with $b \geq 20 \text{ s/mm}^2$ to suppress artifacts from blood flow while mean SNR was determined on $b=0 \text{ s/mm}^2$ images.

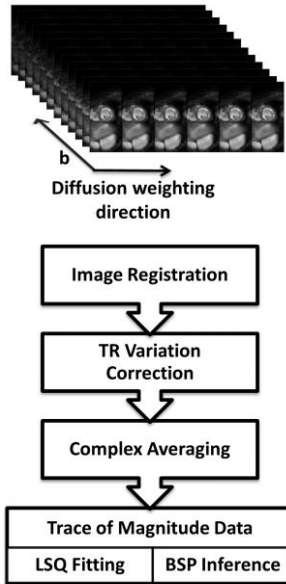


Figure 6.2: Post-processing workflow. Acquired data consists of six diffusion encoding directions, twelve diffusion encoding strengths (b -values) and eight averages. Example magnitudes are displayed at the top. The lower post-processing workflow diagram summarizes consecutive data handling steps in every volunteer. After image reconstruction, image registration is performed to compensate for residual geometric inconsistencies. Heart rate variations and hence signal fluctuations due to TR variations are compensated using recorded ECG signals. Trace data is generated after complex averaging. This data is used for IVIM parameter estimation employing both LSQ and BSP regression

For BSP inference, the total number of MCMC samples was set to $N_S=20000$. A “burn-in” period of 10000 (discarded) samples was used before actual sampling. The Markov chains were initialized with LSQ estimates of the IVIM parameters. Note that the Markov Chains can be started from arbitrary starting values, however a starting point close to the actual parameter estimates shortens the burn-in phase and hence saves computation time. Further details of the estimation method can be found in the Appendix of Orton et al. (Orton et al. 2014). A vectorized approach of the referenced procedure was implemented in Matlab (Mathworks, Natick) and run on standard PC hardware (2.9 GHz, 16 GB RAM).

6.3.4 Reproducibility analysis

In order to assess reproducibility of two consecutive scans, Bland-Altman analysis was performed and the coefficient of variability was calculated for both scan sessions.

6.4 Results

6.4.1 Computer simulations

In Figure 6.3, relative errors of D , F and D^* for BSP versus LSQ as a function of SNR are reported for a Monte Carlo simulation. Both methods show overall decreasing errors for increasing SNR.

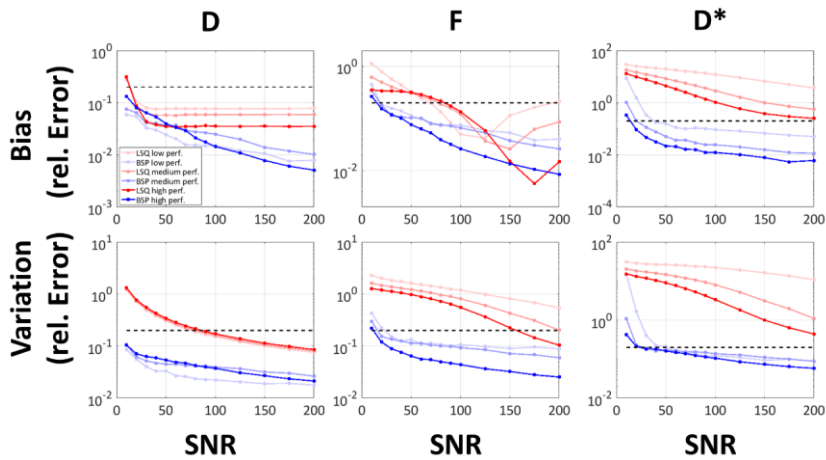


Figure 6.3: Simulation. Accuracy (bias) and precision (variation) errors of LSQ and BSP are determined from SNR 10 to 200 on simulated data for three perfusion regimes. Dashed black lines indicate 20% error

The bias of D with both LSQ and BSP is reduced to below 20% for all perfusion scenarios at $\text{SNR} \geq 20$, with the bias of LSQ remaining between 3% and 10% even at high SNRs. The variation of D with BSP is consistently lower over the entire SNR range compared to LSQ. It drops below 20% error at an SNR of approx. 90 for LSQ, but remains below 20% already for the lowest simulated SNR of 10 for BSP. Estimation of the perfusion fraction F yields lower bias with BSP relative to LSQ between an SNR of 20 to 90-150 depending on the perfusion regime tested. LSQ shows an increase in bias for $\text{SNR} \geq 125-175$. The variation of F with BSP is consistently lower compared to LSQ over the entire SNR range and

perfusion regimes. The relative error is below 20% for $\text{SNR} \geq 30$ if BSP is used for inference. Depending on the perfusion regime simulated, the error using LSQ remains above that threshold except for the high perfusion regime at a $\text{SNR} \geq 175$. The SNR dependency of D^* shows consistently lower bias and variation for BSP relative to LSQ for $\text{SNR} \geq 20$. For LSQ, bias remains above 20% error for an SNR of 200 for all perfusion regimes. Variation of D^* with LSQ remains also above 20% even at an SNR of 200 for all perfusion regimes while bias and variation with BSP are bound to below 20% for SNR values above 40 and 60, respectively. Based on the simulation, an overall minimum SNR of 30-60 depending on the perfusion regime is identified for BSP to determine D , F and D^* within 20% bias and variation. The LSQ method exhibits errors above the mentioned threshold even at an SNR of 200.

6.4.2 In-vivo measurements

The in-vivo SNR measured without diffusion weighting was 19 ± 3 for one signal average, resulting in an SNR of approximately 54 for averaged data. Figure 6.4 shows example in-vivo magnitude images for a selection of b-values. The bright blood pool signal in the center of the image is dephased with increasing diffusion weighting. Example trace magnitude signals averaged across the region-of-interest are displayed. In addition, trace signals from all volunteers and repetitions are plotted.

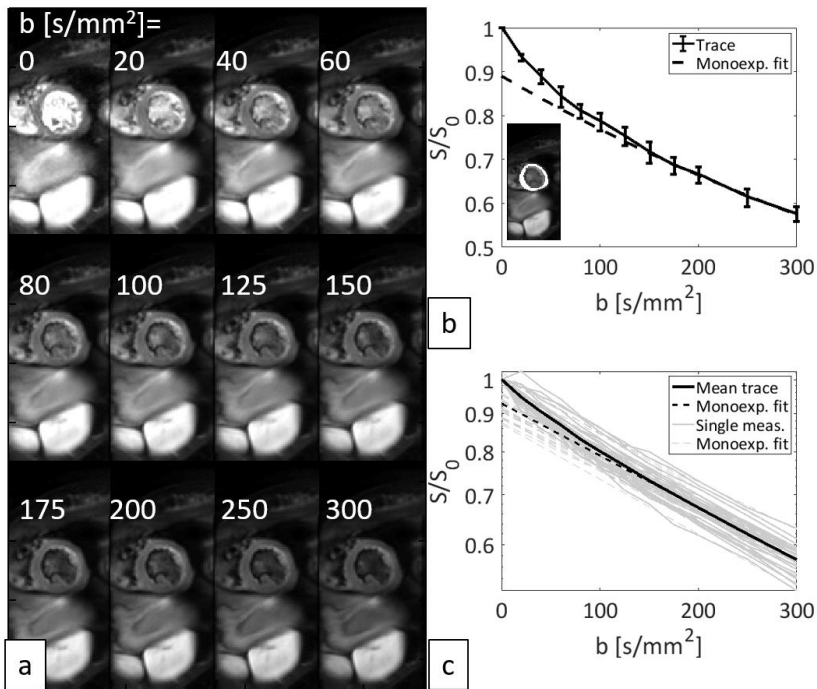


Figure 6.4: In-vivo data. Example averaged co-registered magnitude trace dataset showing all recorded b -values (a), averaged magnitude signal across the region-of-interest (highlighted in the small inset) of the same volunteer with error bars showing variations among diffusion encoding directions together with a mono-exponential fit for $b \geq 200 \text{ mm}^2/\text{s}$ to distinguish the perfusion contribution (b). Mean magnitude signals across all volunteers and repetitions together with the mean over all measurements and corresponding mono-exponential fits (c). Deviations from a purely mono-exponential model are discernable for small b -values ($b < 150 \text{ mm}^2/\text{s}$) in b and c. Note that the plots b and c have logarithmic y-axes

In Figure 6.5, example IVIM parameter maps computed with LSQ and BSP along with corresponding histograms are shown. While LSQ maps exhibit spatial noise and patch-like structures, BSP yields a more uniform distribution in the myocardium which is reflected in narrower distributions of D , F and D^* . Of note, LSQ resulted in a high number of voxels in which the estimated IVIM parameters reached or were close to the box constraints.

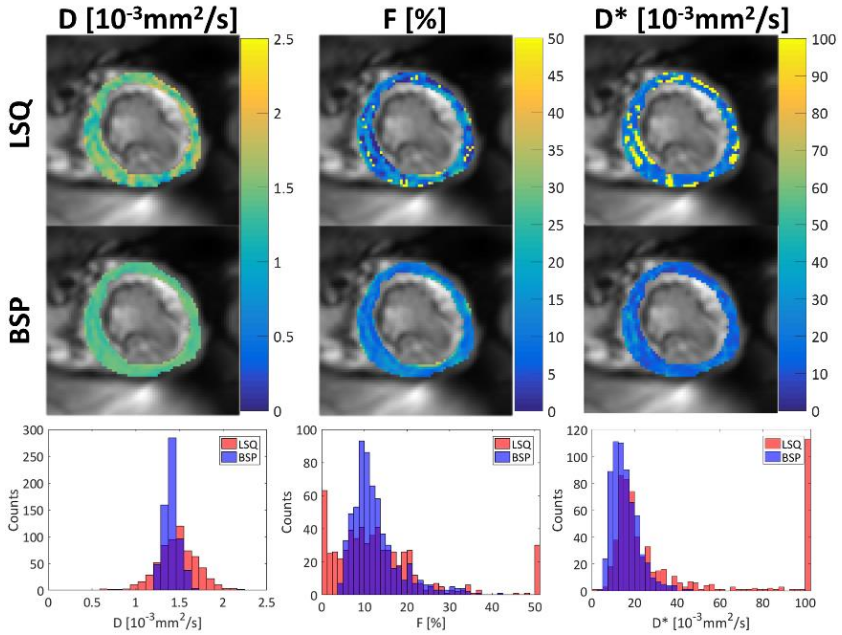


Figure 6.5: IVIM parameter maps with corresponding histograms. Spatial variation of the parameters is reduced for the Bayesian approach (BSP) relative to least-squares (LSQ). Histograms show corresponding narrower distributions for BSP versus LSQ. Note that local variations in F are preserved with the BSP method. Outliers are greatly reduced with BSP for F and D^* .

Figure 6.6 summarizes various parameter estimates together with regression quality measures (LSQ red boxes, BSP blue boxes) as in (Orton et al. 2014). The left column summarizes mean and median estimates across the corresponding regions-of-interest of all parameters. Both the LSQ mean and median estimates of D tend to relatively high values compared to BSP, while the prior mean of BSP is within the range of previously reported values (von Deuster et al. 2016b; Moulin et al. 2016). Considering the parameter F , there are notable differences among the mean and median estimates, indicating the presence of fitting outliers. Again, the prior mean of BSP is in the range of previously reported values (Moulin et al. 2016). The mean estimates of D^* are strongly influenced by (high valued) outliers in the region-of-interest, explaining the difference in mean and median LSQ estimates. The BSP prior means take values close to the LSQ median values. The variability measures within the region-of-

interest in the middle column show reduced variability for BSP versus LSQ in all parameters both considering standard deviation and percentile based measures. The fit quality in terms of median estimated standard deviation under the posterior (for example σ_p) is displayed in the right column. The BSP based deviations are consistently lower compared to the LSQ based values.

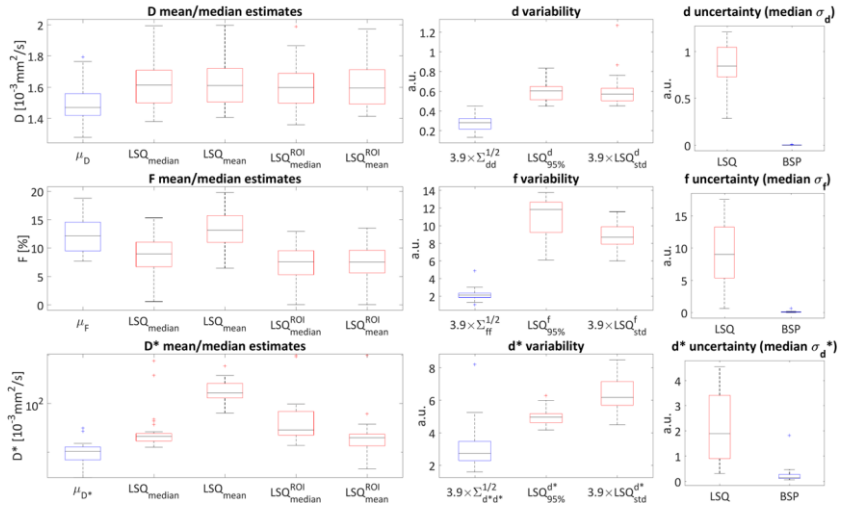


Figure 6.6: Parameter regression Box-and-Whisker plots. Red boxes represent LSQ derived values; blue boxes represent BSP derived estimates across all measurements (volunteers and repetitions). Left column: BSP prior mean values (μ_p , $p = D, F$ and D^*) and means/medians of LSQ pixel-wise (LSQ_{median} and LSQ_{mean}) and region-of interest averaged (LSQ_{median}^{ROI} and LSQ_{mean}^{ROI}) magnitude derived estimates. Note the logarithmic y-scale of the D^* estimates plot. Middle column: parameter estimate variability is displayed as $3.9 \times$ prior standard deviations from the BSP estimation ($3.9 \times \Sigma_{pp}^{1/2}$, $p = D, F$ and D^*), as width of the 95% interval of the LSQ estimates and $3.9 \times$ standard deviation over each region-of-interest of the LSQ estimates (scaled by 3.9 to approximate the 95% interval assuming a Gaussian distribution). Right column: parameter uncertainty displayed as median of estimated standard deviation under the posterior distribution (σ_p , $p = D, F$ and D^*).

For reproducibility analysis, medians across the left ventricular myocardium/region-of-interest were considered because of the large amount

82

of outliers for LSQ fitting. Figure 6.7 shows the Bland-Altman analysis of two consecutive scans within one session. Mean biases (LSQ/BSP) of $+0.02/-0.05 \cdot 10^{-3} \text{ mm}^2/\text{s}$ for D , $-0.58/+0.51\%$ for F and $+26.28/-1.56 \cdot 10^{-3} \text{ mm}^2/\text{s}$ for D^* were found. The Bland-Altman coefficients of repeatability are (LSQ/BSP): $0.22/0.11 \cdot 10^{-3} \text{ mm}^2/\text{s}$ for D , $5.74/5.54\%$ for F and $422.80/11.93 \cdot 10^{-3} \text{ mm}^2/\text{s}$ for D^* .

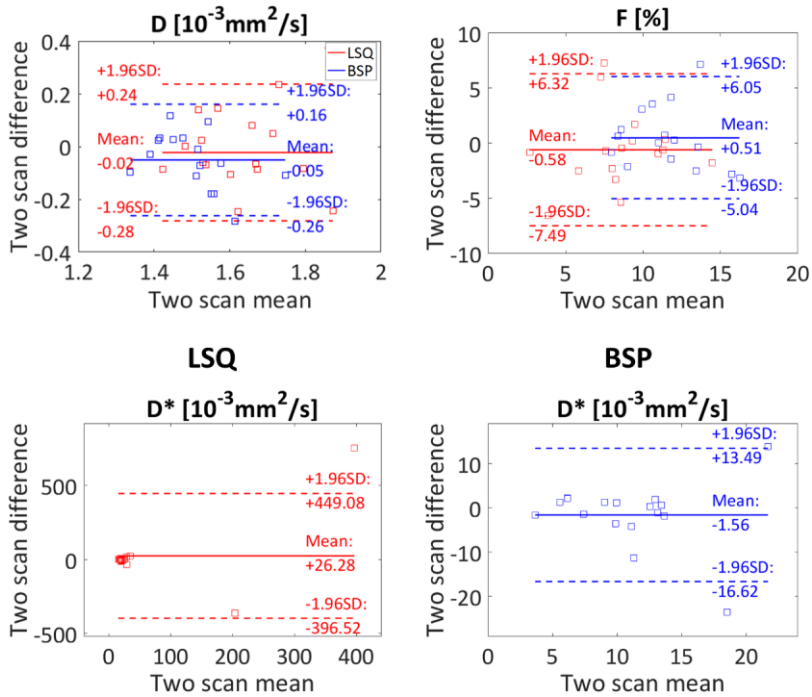


Figure 6.7: Bland-Altman analysis. Bland-Altman plots showing intra-subject reproducibility of the medians across the regions-of-interest of two consecutive scan sessions for both LSQ and BSP. Medians were chosen to reduce the influence of the high ratio of LSQ outliers. Note the different plot ranges of D^* for LSQ and BSP

Figure 6.8 shows a summary over all measurement estimates. The upper row displays medians across the regions-of-interests for both sessions. As in Figure 6.6, the estimates of D were found to be higher for LSQ compared to BSP. The medians of the LSQ/BSP estimates are covering ranges of $0.61/0.51 \cdot 10^{-3} \text{ mm}^2/\text{s}$ for D , $14.79/10.27\%$ for F , $763.37/27.42 \cdot 10^{-3} \text{ mm}^2/\text{s}$ for D^* . The lower row of

Figure 6.8 reports all measurements by displaying the means across all voxels within the region-of-interest and the corresponding standard deviations. The mean values of the IVIM parameters are (LSQ/BSP) $1.63 \pm 0.28 / 1.51 \pm 0.14 \cdot 10^{-3} \text{ mm}^2/\text{s}$ for D , $13.13 \pm 19.81 / 13.11 \pm 5.95\%$ for F and $201.50 \pm 313.20 / 13.11 \pm 14.53 \cdot 10^{-3} \text{ mm}^2/\text{s}$ for D^* . The estimates for all IVIM parameters from the two inference procedures are significantly different ($p < 0.05$) from each other using the Wilcoxon signed-rank test. Both mean D and F are within 10% relative difference, but the mean estimates of D^* are one order of magnitude different from each other. This is again due to the high number of outliers produced by the LSQ method. The standard deviations of all three IVIM parameters are consistently lower for BSP compared to LSQ.

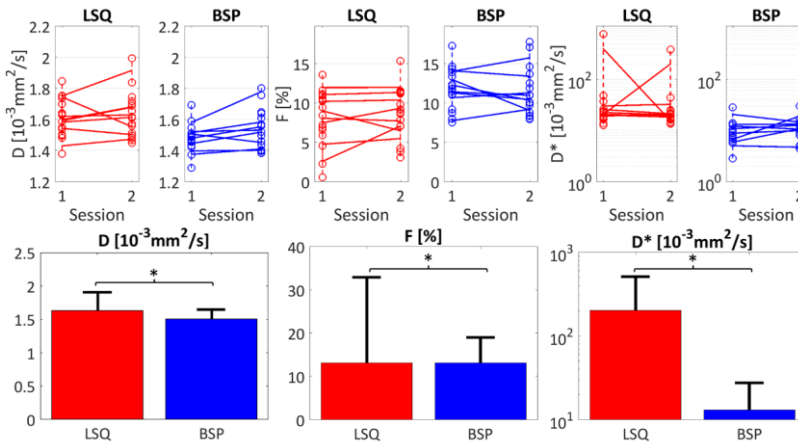


Figure 6.8: Summary. Top row: medians across the regions-of-interest for the two sessions and scans (connected by dashed lines). The means of the medians of the two intra-session repetitions are connected by solid lines for the two sessions. The BSP estimates are clustered closer together and cover a smaller range compared to the LSQ derived estimates. Bottom row: means and standard deviations of all estimates across all volunteers and repetitions. The standard deviations are consistently smaller for BSP. The parameter estimates of the two methods are significantly different (*, $p < 0.05$). Note the logarithmic y-axes for D^* .

Potential scan time reduction was investigated by retrospectively skipping diffusion encoding gradient directions. The reduced SNR due to data subsampling leads to a mean absolute error across all voxels of all measurements of $0.25 / 0.14 \cdot 10^{-3} \text{ mm}^2/\text{s}$ (D), $11.38 / 4.67\%$ (F) and

185.38/15.82·10⁻³ mm²/s (D^*) for LSQ/BSP if only three instead of all six directions are used as shown in Figure 6.9.

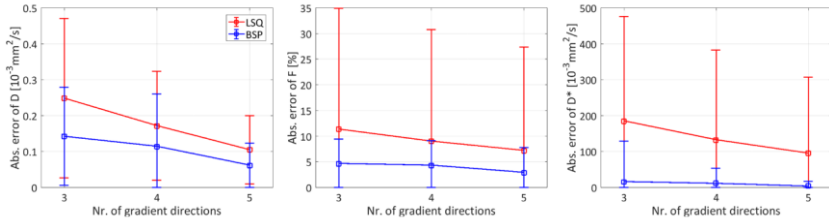


Figure 6.9: Data subsampling. Absolute pixel-wise parameter estimation error for both LSQ and BSP methods versus number of used diffusion encoding gradient directions. Boxes indicate mean values across all voxels of all measurements; error bars are displaying corresponding standard deviations

The LSQ and BSP estimates were further compared by a regression analysis of the median estimates across the corresponding regions-of-interest as shown in Figure 6.10. The diffusion coefficient exhibits an approximately linear correlation between the two methods with LSQ tending to higher values. For the perfusion parameters there is no clear linear correlation. Especially D^* exhibits outliers. The Kullback-Leibler divergences $D_{KL}(\text{LSQ}||\text{BSP})$ of the BSP parameter estimates from the LSQ estimates are summarized for all measurements in Figure 6.10. The median divergences and standard deviations were: 15±11/16±11/14±10 bit for $D / F / D^*$ respectively.

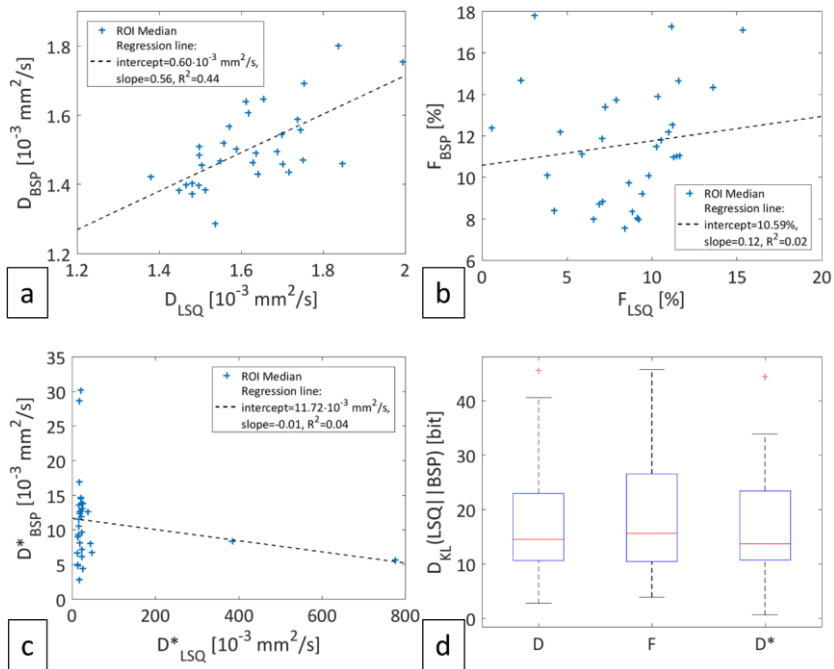


Figure 6.10: Regression lines & Kullback-Leibler divergences. The plots a, b and c display the medians across the corresponding regions-of-interest (ROI) of all measurements together with regression lines. Respective coefficients are shown in the legends. The plot d summarizes the Kullback-Leibler divergences of the BSP estimates from the LSQ estimates of all measurements

The infarcted septal region in an animal model exhibits reduced blood flow in a conventional contrast enhanced first pass perfusion scan as well as reduced IVIM perfusion parameters for both regression methods. The BSP derived maps do not contain outliers and hence allow a clearer delineation of the infarcted area compared to LSQ. Further details can be found in Appendix 2 (Chapter 6.8).

6.5 Discussion

In the present work, Bayesian shrinkage prior inference has been implemented and compared to segmented least-squares fitting for IVIM parameter mapping in the in-vivo human heart.

Robust data acquisition was possible using a second-order motion-compensated diffusion weighted spin-echo sequence (Stoeck et al. 2016) triggered to early systole. Using a trigger delay of 25% peak systole is advantageous because of increased coronary flow compared to peak contraction. Moreover, a large part of systole is potentially available for IVIM acquisitions as shown in (Stoeck et al. 2016): trigger delays in the range of 15-77/79% peak systole at the apex/base allow for robust diffusion data acquisition. In addition, imaging in systole has the advantage of a relatively thick myocardium compared to the voxel size.

Using motion-compensated diffusion gradients may lead to a reduced sensitivity to blood circulation and myocardial perfusion (Wetscherek et al. 2015). However, deviations from a mono-exponential diffusion model at lower b -values due to perfusion were observed in all measurements indicating sufficient sensitivity to microcirculation and perfusion. Balancing motion-induced signal loss due to cardiac bulk motion while achieving optimal sensitivity to perfusion is however a subject deserving further attention.

Computer simulations revealed minimum SNR thresholds of 30-60 for relative errors in terms of bias and variation of 20% each, depending on the perfusion regime for BSP while the LSQ method required a minimum SNR of at least 200. The increase in bias in F for the SNR range of 125-175 using LSQ is suspected to be an artefact of the segmented fit, which leads to an error propagation of D and S_{int} into the estimation of the perfusion parameters. Furthermore, we note that Federau and colleagues also reported a similar increase in bias in F in Figure 1 of (Federau et al. 2015) using a segmented approach; albeit in the SNR range of approx. 20-40 with simulated IVIM parameters which are commonly found in the brain ($D=0.7\cdot 10^{-3} \text{ mm}^2\text{s}^{-1}$, $F=4\%$ and $D^*=17\cdot 10^{-3} \text{ mm}^2\text{s}^{-1}$). Even though the relative bias in F in the considered SNR range is below about 10%, the segmented fit might benefit from a joint parameter estimation (potentially using two regimes of mono- and bi-exponential decay) in this regard. While these simulation results are indicative, several factors confounding in-vivo measurements have not been taken into account in the simulations including residual motion artifacts and partial voluming with hyperintense blood signal and epicardial fat (While 2017). These effects would lead to a broadening of the parameter histograms. Accordingly, the width of

the prior is increased by the presence of a large number of affected voxels. The shrinking procedure in these cases is less effective.

In-vivo, BSP analysis resulted in IVIM parameter maps with considerably smaller intra-myocardial standard deviations relative to LSQ. Both variability and estimation uncertainty in terms of standard deviation under the posterior were greatly reduced with BSP compared to LSQ (Figure 6.6), indicating the benefit of taking into account prior knowledge. The setting of arbitrary fit constraints was obsolete in the BSP procedure. In addition, BSP regression was aided by the prior which led to the elimination of outliers on or close to the fit boundaries.

An effective spatial denoising of the parameters can be achieved because the prior in BSP is chosen to be a unimodal distribution. This prior assumes a population mean of the IVIM parameters for the whole region-of-interest and hence assumes the myocardium of the left ventricle to have a rather homogenous spatial tissue characteristic. If local pathologies such as myocardial infarcts (as for example presented in Appendix 2/Chapter 6.8) and corresponding fibrous tissue with reduced perfusion (von Deuster et al. 2015) are present, a different choice of priors such as a spatial homogeneous prior (Freiman et al. 2013) is deemed more appropriate (While 2017). Alternatively, multimodal priors can be applied to distinguish among different tissue types while still retaining spatial information. Methods using mixture models (Stoneking 2014) of multivariate Gaussians could also be implemented to address this limitation. In contrast to the LSQ approach, which allows data processing on a pixel-by-pixel basis, the BSP method requires pre-segmentation of the data, which renders automation in a post-processing workflow more challenging.

Overall, the in-vivo IVIM parameters measured in this study are in good accordance with recent literature (Froeling et al. 2014; Moulin et al. 2016). The diffusion coefficients D found in this study using LSQ and BSP were within the range of the values found in (Froeling et al. 2014; Moulin et al. 2016). A higher measured diffusivity is indicative of residual motion effects in the data (Stoeck et al. 2017). In addition, the mean diffusivity measured using spin-echo based Diffusion Tensor Imaging (DTI) during early systole (von Deuster et al. 2016b) was within 14% and 6% of the mean measured diffusion coefficient of the present study for LSQ and BSP, respectively. The measured perfusion fraction F was found to be lower compared to data reported in (Froeling et al. 2014). The LSQ and BSP estimation of approx. 13% is close to the 12% found in (Moulin et al. 2016) during diastole. The pseudo-diffusion coefficients D^* of $201.50 \pm 313.20 \cdot 10^{-3} \text{ mm}^2/\text{s}$ (LSQ) and $13.11 \pm 14.53 \cdot 10^{-3} \text{ mm}^2/\text{s}$ (BSP) as measured in the present study are different from previous data

($52.68 \pm 52.61 \cdot 10^{-3} \text{ mm}^2/\text{s}$ (Froeling et al. 2014), $43.6 \pm 9.2 \cdot 10^{-3} \text{ mm}^2/\text{s}$ (Moulin et al. 2016)). However, D^* usually contains the highest number of outliers and the mean across the region-of-interest is therefore prone to be heavily influenced by the choice of the actual value of the box-constraints. If the medians across the region-of-interest are considered, it is shown that the majority of the LSQ estimates gather in the range of 20 to $50 \cdot 10^{-3} \text{ mm}^2/\text{s}$. Moreover, data in Figure 6.6 indicates that mean estimates of D^* are considerably influenced by outliers with median parameter values close to the ones found using the BSP method.

The IVIM perfusion parameters in an infarcted animal model (see also Appendix 2) show good accordance with the perfusion defect visible in the contrast enhanced perfusion scan, especially considering the blood flow related (Federau et al. 2014; Federau et al. 2015) product $F \times D^*$ of the BSP derived estimates. However, the extension of the infarct indicated by IVIM appears smaller compared to the darkened area of the contrast enhanced perfusion scan. This might be due to residual motion and/or partial voluming which can yield elevated IVIM parameter estimates.

All SNR measurements were obtained from a single signal average. Thereby confounding factors due to image registration and phase correction for averaging of complex data were avoided. The in-vivo SNR was above the 20% parameter error threshold found in simulations. The scan of ca. 18 min for a heart rate of 60 bpm for this study was in-between previous scanning times of 15 min (Froeling et al. 2014) and 20 min (Moulin et al. 2016). Optimizations of the experiment design in terms of b-value distribution (Lemke et al. 2011), higher static field strength and improved gradient performance to reduce echo times may allow to reduce parameter estimation error and scan time.

By design, Bayesian approaches exploiting information across the region-of-interest can be used to examine distributed rather than focal pathologies of the myocardium. Accordingly, potential applications relate to microvascular obstruction and educed and/or delayed perfusion of the myocardium in hypertrophic cardiomyopathy and diabetes (Fang et al. 2004; Ismail et al. 2014).

6.6 Conclusion

Bayesian IVIM parameter mapping yields improved parameter maps relative to conventional segmented least-squares fitting in the human heart. In conjunction with motion compensated diffusion weighted spin-echo sequences, robust parameter estimation can be achieved providing a tissue perfusion surrogate without contrast agent application. Further in-vivo studies

are now warranted to assess the performance of the method in relevant patient populations.

6.7 Appendix 1

6.7.1 Hierarchical Bayesian modelling

The Bayesian inference procedure (Orton et al. 2014) is summarized as follows. Using the IVIM model

$$y_n = S_0 \left[F \cdot \exp(-b_n D^*) + (1-F) \cdot \exp(-b_n D) \right] + \eta_n, \quad (6.5)$$

where y_n is a data point measured at the n-th b-value b_n with error term η_n of Gaussian distribution with variance σ_s^2 , the data likelihood reads:

$$p(\mathbf{y} | D, F, D^*; S_0, \sigma_s^2) = (2\pi\sigma_s^2)^{-N/2} \exp \left[-\frac{1}{2\sigma_s^2} \sum_{n=1}^N (y_n - S_0 g_n)^2 \right] \quad (6.6)$$

where $\mathbf{y} = (y_1, y_2, \dots, y_N)^T$, $g_n = F \cdot \exp(-b_n D^*) + (1-F) \cdot \exp(-b_n D)$ and N =number of b-values.

From a Bayesian perspective, nuisance parameters which are of no interest can be marginalized out. Here, the nuisance parameters S_0 and σ_s^2 are integrated out by using a conjugate Normal-Inverse-Gamma prior distribution

$$p(S_0, \sigma_s^2) = N(S_0 | \mathbf{0}, \delta^2 \sigma_s^2 / (\mathbf{g}^T \mathbf{g})) \cdot IG(\sigma_s^2 | \alpha, \beta) \quad (6.7)$$

with $\mathbf{g} = (g_1, g_2, \dots, g_N)^T$ and integration over the domain of definition:

$$p(\mathbf{y} | D, F, D^*) = \int_0^\infty \int_{-\infty}^\infty p(S_0, \sigma_s^2) p(\mathbf{y} | D, F, D^*; S_0, \sigma_s^2) dS_0 d\sigma_s^2 \quad (6.8)$$

The choice of prior allows for an analytic evaluation of Equation(6.8). The influence of the prior for the marginalization procedure is diminished by taking the limits of the variance of the Normal distribution $\delta \rightarrow \infty$ and shape and scale parameters of the Inverse Gamma distribution $\alpha, \beta \rightarrow \mathbf{0}$ which encodes

a complete lack of prior information. Ignoring proportionality constants which do not depend on the IVIM parameters and are hence not necessary for parameter inference, the marginalized likelihood becomes:

$$p(\mathbf{y} | D, F, D^*) \propto \left[\mathbf{y}^T \mathbf{y} - (\mathbf{y}^T \mathbf{g})^2 / (\mathbf{g}^T \mathbf{g}) \right]^{-N/2} \quad (6.9)$$

In order to take advantage of the histogram structure of IVIM parameters, a hierarchical prior structure is adopted. First, a multivariate Gaussian is applied to the transformed IVIM parameters. Those transformations are mapping the domain of definition to the field of real numbers:

$$\begin{aligned} d &= \log(D) \\ f &= \text{logit}(F) = \log(F) - \log(1-F) \\ d^* &= \log(D^*) \end{aligned} \quad (6.10)$$

The multivariate Normal distribution considers heterogeneity across the region-of-interest and models correlations between the parameters via the covariance matrix Σ_{μ} :

$$p(\boldsymbol{\theta}_i | \boldsymbol{\mu}, \Sigma_{\mu}) = \left| 2\pi \Sigma_{\mu} \right|^{-1/2} \exp \left[-\frac{1}{2} (\boldsymbol{\theta}_i - \boldsymbol{\mu})^T \Sigma_{\mu}^{-1} (\boldsymbol{\theta}_i - \boldsymbol{\mu}) \right] \quad (6.11)$$

The mean across the region-of-interest of the parameter $\boldsymbol{\theta}_i = (d_i, f_i, d_i^*)$ of voxel i is $\boldsymbol{\mu} = (\mu_d, \mu_f, \mu_{d^*})$. Jeffreys' prior (Jeffreys 1946) is used for the hyper-parameters $\boldsymbol{\mu}$ and Σ_{μ} :

$$p(\boldsymbol{\mu}, \Sigma_{\mu}) = \left| I(\Sigma_{\mu}) \right|^{1/2} = \left| \Sigma_{\mu} \right|^{-1/2} \quad (6.12)$$

This prior describes a high probability for a large determinant of the Fisher Information $I(\Sigma_{\mu})$ and hence in the considered case of a multivariate Normal distribution for a small determinant of the parameter covariance matrix Σ_{μ} in the region-of-interest. Therefore, a “shrinking” of parameter estimates towards the mean of the distribution can typically be observed. The posterior is then given by

$$p(\boldsymbol{\theta}_{1:M}, \boldsymbol{\mu}, \Sigma_{\boldsymbol{\mu}} | \mathbf{y}_{1:M}) = \frac{p(\boldsymbol{\mu}, \Sigma_{\boldsymbol{\mu}}) \prod_{i=1}^M p(\mathbf{y}_i | \boldsymbol{\theta}_i) p(\boldsymbol{\theta}_i)}{p(\mathbf{y}_{1:M})}. \quad (6.13)$$

The total number of voxels considered here is M . The parameter independent data evidence $p(\mathbf{y}_{1:M})$, is not required for the inference procedure. Expectation values under the posterior in Equation (6.13) are calculated for example as

$$\hat{d}_i = \int d_i p(\boldsymbol{\theta}_{1:M}, \boldsymbol{\mu}, \Sigma_{\boldsymbol{\mu}} | \mathbf{y}_{1:M}) d\boldsymbol{\theta}_{1:M} d\Sigma_{\boldsymbol{\mu}} d\boldsymbol{\mu} \quad (6.14)$$

and analogously for other parameters or quantities.

In order to determine variance under the posterior as uncertainty measure for the LSQ method, a flat prior according to the box constraints in Equation (6.4) is chosen instead of the hierarchical prior structure (Orton et al. 2014).

6.7.2 Markov chain Monte Carlo (MCMC) implementation

The integration in Equation (6.14) cannot be performed analytically and therefore a MCMC-based numerical approach is implemented (Orton et al. 2014). The expectation value of a parameter (for example d) is approximated by using N_s samples $d_i^{(j)}$ from a Markov chain output:

$$\hat{d}_i = \frac{1}{N_s} \sum_{j=1}^{N_s} d_i^{(j)} \quad (6.15)$$

6.8 Appendix 2

6.8.1 Infarcted porcine heart

Both LSQ and BSP approaches were compared in an animal model of acute myocardial infarction. Obtained diffusion weighted data from a single female pig (65 kg, heart rate 68 1/s) using second-order motion compensated diffusion gradients (Stoeck et al. 2016) were evaluated. The imaging parameters were: in-plane resolution: $2.4 \times 2.4 \text{ mm}^2$, slice thickness: 10 mm, one apical slice, field-of-view (FOV): $230 \times 120 \text{ mm}^2$, acquired k-space lines: 49, TR/TE: 2 R-R/93 ms, trigger delay 50% peak systole, flip angle: 90° , 8 signal averages and 6 diffusion encoding directions (Jones et al. 1999). The 15 optimized diffusion encoding strengths were taken from (Lemke et al. 2011) with a maximum b-value of 740 s/mm^2 . The apical myocardial infarct was induced by a permanent distal ligation

of the left anterior descending (LAD) coronary artery. The animal was anesthetized by a constant dose of Propofol (1.0 ml/kg/min) during surgery and the scan. The experiment was performed in adherence to the Swiss law of Animal Protection and approved by the Zurich cantonal veterinary office.

The IVIM parameter maps are shown together with dynamic contrast enhanced (DCE) first pass perfusion images in Figure 6.11. The infarcted area can be delineated in the septal area (red arrow). The LSQ and BSP derived diffusion coefficients D are similar across the whole LV. The perfusion fraction F is reduced in the septal area for both methods, with outliers present for LSQ. The pseudo-diffusion coefficient D^* is also clearly reduced in this area for BSP but shows insensible high values for LSQ due to the optimization reaching the fit constraints. If the blood flow related (Federau et al. 2014; Federau et al. 2015) product of $F \times D^*$ is considered, the LSQ derived product does not allow to delineate the infarcted region due to many outliers. In contrast, the septal region in the BSP derived map shows reduced IVIM perfusion parameters.

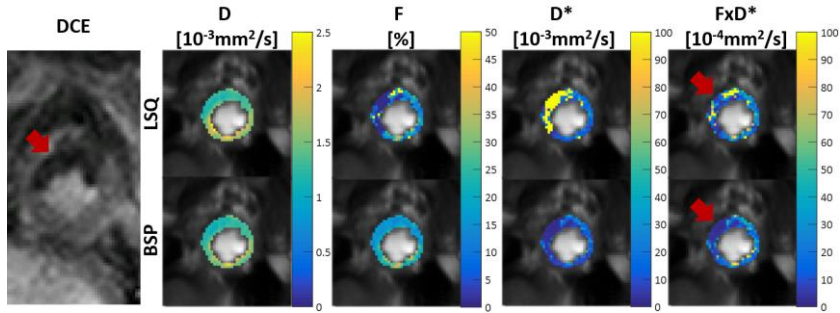


Figure 6.11: Infarcted porcine heart. Animal sub study: Dynamic contrast enhanced (DCE) first pass imaging shows a myocardial infarct in the septal area (red arrow). Corresponding IVIM parameter maps in the same slice position reveal a reduction in perfusion related parameters in the septal region. The LSQ approach suffers from many outliers, while the BSP approach shows low parameter variability (red arrows).

Chapter 7

On probing intravoxel incoherent motion in the heart – spin-echo versus stimulated-echo diffusion-weighted imaging³

7.1 Introduction

In the presence of diffusion encoding gradients, perfusion of tissue leads to a modulation of the MR signal. The influence of perfusion on the MR signal is commonly described by the Intravoxel Incoherent Motion (IVIM) concept (Le Bihan et al. 1986; Le Bihan 2008) which models perfusion as a pseudo-diffusion process on the macroscopic scale. To this end, an isotropic random orientation of the microvasculature of the capillary network is assumed (Le Bihan et al. 1988; Le Bihan and Turner 1992) resulting in a Gaussian stochastic process. Similar to water self-diffusion, perfusion is described to cause a mono-exponential MR signal decay with increasing diffusion weighting. Therefore, two diffusion compartments are assumed to model perfusion and diffusion. The perfusion fraction depends on the amount of vasculature in a given voxel relative to the water contained in the extravascular space. The pseudo-diffusion coefficient describes blood flow through the capillaries as a diffusion-like process and hence it relates to blood flow velocity, change of capillary direction and mean capillary segment length. Considering both diffusion and perfusion, the IVIM model results in a bi-exponential model of the image magnitude as a function of diffusion weighting. The model has frequently been used to fit data acquired in a variety of anatomical regions including abdomen (Yamada et al. 1999; Luciani et al. 2008; Lemke et al. 2009; Patel et al. 2010; Notohamiprodjo et al. 2015), heart (Froeling et al. 2014; von Deuster et al. 2015; Moulin et al. 2016; Spinner et al. 2017) and brain (Federau et al. 2012; Federau et al. 2014; Federau et al. 2017).

Beyond the original IVIM model (Le Bihan et al. 1986), various extensions have been proposed. For example, anisotropy of Gaussian distributions may be modeled as a tensor as in diffusion tensor imaging (DTI) (Abdullah et al. 2016).

³ Published in: Spinner GR, Stoeck CT, Mathez L, von Deuster C, Federau C, Kozerke S (2019) *On Probing Intravoxel Incoherent Motion in the Heart – Spin-Echo versus Stimulated-Echo Diffusion-Weighted Imaging*. *Magnetic Resonance in Medicine* (early view). doi: 10.1002/mrm.27777

Alternatively, anisotropy may be modelled using von Mises (also called Fisher-axial) distributions to describe the spatial orientation of the vasculature around a main direction, i.e. the dispersion of the zenith angle of the capillary segments (Karampinos et al. 2010). Further, the stochastic process assumed in the IVIM model was shown to deviate from a Gaussian distribution within a voxel if only a few capillary segments are traversed (Wetscherek et al. 2015) and that the usage of gradient shapes which compensate higher-order moments leads to a reduced signal attenuation due to perfusion (Wetscherek et al. 2015; Moulin et al. 2019).

Considering experimental data, both ex-vivo and in-vivo IVIM studies have been performed in the heart. Canine hearts were studied in-vivo, under adenosine administration and post mortem (Callot et al. 2003), using the stimulated echo acquisition mode (STEAM). It was shown that the measured perfusion parameters depend on the diffusion encoding gradient direction, they increase during adenosine administration and they approach noise levels post-mortem. Human hearts were studied (Delattre et al. 2012; Moulin et al. 2016) with spin-echo (SE) sequences triggered to a range of diastolic time points with subsequent filtering and maximum intensity projection through time (PCATMIP) (Pai et al. 2011; Moulin et al. 2016). In-vivo human data was also obtained using second-order motion-compensated SE-DWI triggered to systole with consecutive hierarchical Bayesian IVIM parameter estimation (Spinner et al. 2017). Patient data were also reported using SE-DWI in diastole (Mou et al. 2017) demonstrating differences of the pseudo-diffusion coefficient between patients and healthy volunteers. Infarcted pig hearts were studied in-vivo and post mortem (von Deuster et al. 2015) using second-order motion-compensated SE-DWI in systole. Reduced perfusion parameters were detected in infarcted areas in-vivo. Finally, re-perfused guinea pig hearts were successfully studied using the aforementioned SE-DWI tensor approach (Abdullah et al. 2016).

Despite all advances, reliable and reproducible IVIM data acquisition in the in-vivo heart remains challenging due to the inherently small influence of perfusion onto the total signal as well as residual bulk motion and cardiac strain effects. While the original isotropic IVIM model (Le Bihan et al. 1986) has been used to fit in-vivo cardiac data, its validity in the heart has never been proven. The myocardium exhibits an anisotropic muscle fiber microstructure (Mekkaoui et al. 2017) with a significant fraction of capillaries being aligned with myofiber aggregates (Kaneko et al. 2011) and hence resultant perfusion anisotropy. In addition, diffusion encoding durations on the order of 100ms as used with in-vivo SE-DWI may prompt concerns regarding sufficient signal attenuation being achieved while traversing only a few capillary segments (Le Bihan et al. 1988).

Finally, the IVIM model is a non-linear model of two diffusion compartments where the relative weight of the pseudo-diffusion compartment is about one tenth of the dominant diffusion compartment. Echocardiographic data has revealed a volume fraction of blood in myocardium of $12.6 \pm 1.8\%$ healthy individuals at rest (Indermühle et al. 2006), which is confirmed by IVIM-derived perfusion fractions of $12.2 \pm 1.3\%$ (Moulin et al. 2016) and $13.1 \pm 6.00\%$ (Spinner et al. 2017). Accordingly, parameter fitting of low SNR data may lead to potential bias and variation (Spinner et al. 2017) because of the intrinsic model non-linearity and the relatively weak contribution of the perfusion compartment to total signal attenuation.

The objective of the present work was to model the stochastic process of cardiac perfusion using realistic data of myocardium and to simulate the MR signal for SE and STEAM based diffusion-encoding gradient schemes as used for in-vivo cardiac DWI/DTI. Numeric simulations yield the IVIM encoding efficiency of the various schemes and reveal potential systematic biases due to fitting at different noise settings. Using perfused porcine hearts, the simulations are experimentally validated and the detection sensitivity of ischemia due to transient coronary occlusion is demonstrated.

7.2 Theory

7.2.1 IVIM model

The IVIM model (Le Bihan et al. 1986) assumes tissue perfusion to attenuate the MR signal magnitude depending on the diffusion weighting vector $\mathbf{b} = \mathbf{e}_g b$ with unit vector \mathbf{e}_g in gradient direction and diffusion encoding strength b :

$$\frac{S(\mathbf{b})}{S_0} = f \cdot F_p(\mathbf{b}) + (1-f) \cdot F_D(\mathbf{b}) \quad (7.1)$$

with magnitude $S(\mathbf{b})$, non-diffusion weighted magnitude S_0 , perfusion fraction f , perfusion-related signal modulation $F_p(\mathbf{b})$ and diffusion-related signal modulation $F_D(\mathbf{b})$. In the classical IVIM model (Le Bihan et al. 1986), these modulations are mono-exponential decays with different scalar decay coefficients each: $F_p(\mathbf{b}) = \exp(-bD^*)$ and $F_D(\mathbf{b}) = \exp(-bD)$.

7.2.2 Normalized phase distributions

In general, the signal modulation due to perfusion $F_p(\mathbf{b})$ can be expressed as the following expectation value with spin phase ϕ :

$$F_p = \langle \exp(i\phi) \rangle = \int_{-\infty}^{\infty} \rho(\phi) \exp(i\phi) d\phi \quad (7.2)$$

The intravoxel phase dispersion $\rho(\phi)$ due to perfusion as stated in Equation (7.2) is described in the following using normalized phases (Wetscherek et al. 2015). They allow to derive phase distributions for various blood flow velocities, b-values and diffusion encoding times by scaling. Therefore, the number of computationally expensive simulation runs can be reduced.

The phase accumulated by transverse magnetization moving along trajectory $\mathbf{x}(t)$ during encoding time T with gradient waveform \mathbf{g} reads:

$$\phi = \gamma \int_0^T \mathbf{x}(t) \cdot \mathbf{g}(t) dt = -\gamma \int_0^T \left(\int_0^t \mathbf{g}(t') dt' \right) \cdot \mathbf{v}(t) dt \quad (7.3)$$

The right-hand side of Equation (7.3) is calculated using integration by parts, $\mathbf{x}(t) = \mathbf{x}_0 + \int_0^t \mathbf{v}(t') dt'$ with $\mathbf{v}(t) = \frac{d}{dt} \mathbf{x}(t)$ and by assuming a vanishing net area of the diffusion encoding waveform $\mathbf{g}(t)$ (“rephasing condition”).

In order to circumvent separate simulation runs for each gradient setting (e.g. b-value), a normalized phase (Wetscherek et al. 2015) is derived after factoring out variables to allow scaling of (normalized) phase distributions. Introducing the gradient shape decomposition $\mathbf{g}(t) = \mathbf{e}_g g h(t/T)$, gradient strength g , gradient unit direction \mathbf{e}_g and normalized waveform $h(t/T)$ and using the definition of the b-value $b = \int_0^T \left(\gamma \int_0^t \mathbf{g}(t') dt' \right)^2 dt$, one can find the relation

$b = \gamma^2 g^2 T^3 \cdot a^2$. The normalized b-value $a = \sqrt{\int_0^1 m_0(s)^2 ds}$ contains the normalized 0th gradient moment $m_0(s) = \int_0^s h(s') ds'$ with normalized time

$s = t/T$. These quantities can be plugged into Equation (7.3) together with the assumption of straight capillary segments, such that an integral over time can be decomposed and written as sum over several integrals along the traversed segments:

$$\phi = -v\sqrt{bT} \cdot \frac{1}{a} \cdot \sum_{k=1}^N \mathbf{e}_g \cdot \mathbf{e}_{x_k} \cdot \int_{s_{k-1}}^{s_k} m_0(s) ds \quad (7.4)$$

where the definitions $\mathbf{v}_k = v\mathbf{e}_{x_k}$ (velocity unit directions of individual segments are denoted \mathbf{e}_{x_k}) and $s_0 = 0$ were used together with a maximum upper integral bound of one. A normalized phase φ can then be defined from Equation (7.4) which depends only on the gradient shape, spatial orientation and length distribution of the simulated capillary segments:

$$\phi = v\sqrt{bT} \cdot \varphi \quad (7.5)$$

The perfusion-induced signal modulation F_p in Equation (7.2) can also be formulated in terms of the normalized phase φ by using change-of-variable in the distribution function $\rho(\phi) = \rho(\phi(\varphi))$ and the corresponding substitution in the integral to arrive at:

$$F_p = \int_{-\infty}^{\infty} \rho(\varphi) \exp(iv\sqrt{bT} \cdot \varphi) d\varphi \quad (7.6)$$

From Equation (7.6), the magnitude $|F_p|$ and phase $\angle F_p$ can be derived.

7.2.3 Gaussian phase approximation

The signal attenuation can be approximated by the Gaussian phase approximation (GPA, (Wetscherek et al. 2015)) corrected for a net phase $\langle \varphi \rangle$:

$$|F_p| = \left| \left\langle \exp(iv\sqrt{bT}\varphi) \right\rangle \right| \approx \exp \left[-bTv^2 \frac{1}{2} \left\langle (\varphi - \langle \varphi \rangle)^2 \right\rangle \right] \quad (7.7)$$

From Equation (7.7), an effective pseudo-diffusion coefficient $D_{eff}^* = Tv^2 \frac{1}{2} \left\langle (\varphi - \langle \varphi \rangle)^2 \right\rangle$ can be identified. This coefficient allows to approximate the perfusion-induced signal attenuation by a simple mono-exponential decay, similar to the original IVIM model (Le Bihan et al. 1986).

7.3 Methods

7.3.1 Cardiac capillary structure

The original IVIM model assumes that the orientations of all M segments $\{\mathbf{e}_k\}_M$ are isotropically distributed. The capillaries in the heart are, however, largely aligned with the muscle fibers (Kaneko et al. 2011). Accordingly, we modeled the anisotropy using a von Mises distribution of the zenith angles of the capillary segments (Mathieu et al. 1983; Poole and Mathieu-Costello 1990) as follows:

$$p(\theta | \mu_\theta, \kappa) = \frac{1}{2\pi I_0(\kappa)} \cdot \exp[\kappa \cos(\theta - \mu_\theta)] \quad (7.8)$$

with mean μ_θ , concentration parameter κ (zero corresponds to a uniform distribution, i.e. isotropy, large values correspond to high anisotropy) and Bessel function of 0th order $I_0(\kappa)$. The azimuth angles \mathcal{G}_k were modeled with a uniform distribution between zero and 2π . These distributions have also been used to model the anisotropy in the intravoxel partially coherent motion model (Karampinos et al. 2010).

The capillary segment length distribution was modelled using a Weibull distribution (Kaneko et al. 2011):

$$p(l | a, b) = \frac{b}{a} \left(\frac{l}{a}\right)^{b-1} \exp\left[-\left(\frac{l}{a}\right)^b\right] \quad (7.9)$$

with shape and scale parameters a and b .

The starting point of individual spins on the initial segment was chosen to be a uniform distribution between zero and one. Figure 7.1 summarizes and illustrates the simulation approach.

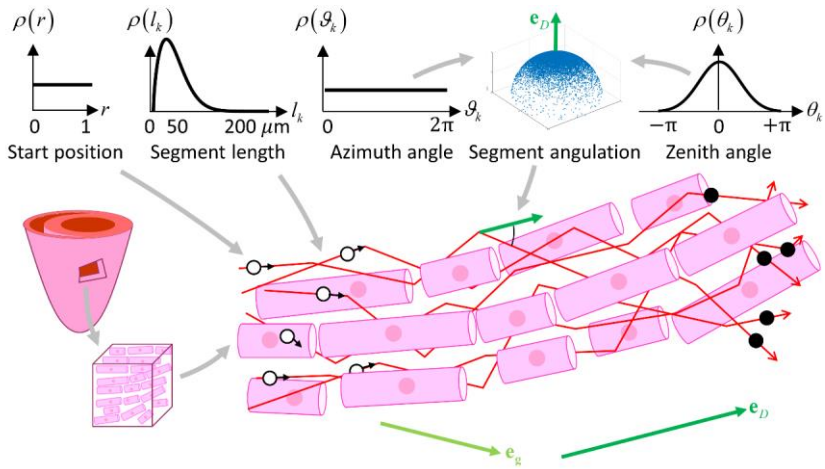


Figure 7.1: Illustration of the perfusion simulation in the myocardium. The capillary segments (red) follow the myocytes (purple cylinders). The starting positions (black open circles, velocity vector indicates direction) are uniformly distributed on the initial segment, the segment length follows a Weibull distribution and the segment angulation is parameterized using the azimuth and zenith angles: the first follows a uniform distribution while the latter is described using a von Mises distribution. The endpoints on the last segment are denoted as black filled circles. The myocyte direction as derived from the diffusion measurement is indicated by the eigenvector \mathbf{e}_D as dark green arrow. The (arbitrarily chosen) encoding gradient direction (vector \mathbf{e}_g) is indicated as light green arrow.

7.3.2 Diffusion encoding gradients

Four different diffusion encoding gradient waveforms were simulated: Stejskal-Tanner SE-DWI (Stejskal and Tanner 1965) without motion compensation and referred to as M0; SE-DWI with first-order motion-compensated gradients (M1) (Gamper et al. 2007); SE-DWI with second-order motion compensated gradients (M2) (Stoeck et al. 2016); and STEAM-DWI (Edelman et al. 1994). Figure 7.2 displays all (normalized) gradient waveforms along with the respective 0th gradient moments and their integrals. In all cases, gradient slopes were idealized.

The timing of the gradient waveforms for equal b-value were as follows: total encoding time T 105.30 ms (T_{SE}) for SE-DWI, 1363.64 ms (T_{STEAM}) for STEAM, gradient lobe duration $\delta = 10.40/21.25/15.04/3.40$ ms, gap duration 100

84.50/20.30/15.04/1360.20 ms for SE-M0/SE-M1/SE-M2/STEAM. Note that for SE-M2 the second lobe is twice as long as the first lobe and the gap duration is equal to the lobe duration.

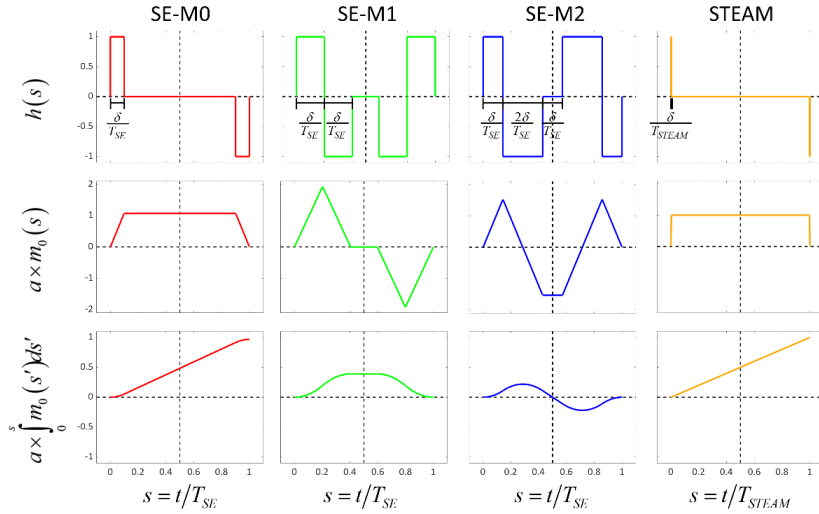


Figure 7.2: Gradient shapes, 0th moments and integrals of the 0th moment. Normalized effective gradient shapes of Stejskal-Tanner SE-DWI (M0, red), first-order motion-compensated SE-DWI (M1, green), second-order motion-compensated SE-DWI (M2, blue) and STEAM-DWI (orange). The normalized time on the x-axis corresponds to the timing used in the simulations and ex-vivo studies. The bottom row shows the integral of the 0th gradient moment (multiplied by the normalized b-value) which is used for generation of phase distributions.

7.3.3 Simulations

To efficiently sample from the distributions in Equations (7.8) and (7.9), numerical inverse transform sampling was performed i.e. the probability distribution functions (pdfs) were evaluated at 10^4 points, their respective cumulative distribution functions (cdfs) determined and linear interpolation was performed during sampling for values in between the evaluated data points. The Weibull distribution in Equation (7.9) is defined for all positive values. In order to enable efficient numerical sampling as explained above, the cdf was truncated at a probability of 0.999. Note that the zenith angle distribution, which is used for sampling, contains an additional sine factor given the use of spherical coordinates (Karampinos et al. 2010). The zenith angle concentration parameter was set to $\kappa=3.25$ (Mathieu et al. 1983; Poole and

Mathieu-Costello 1990). The maximum zenith angle was 0.5240π to represent dominant forward flow with about 6% reverse flow given the relative frequency of the “hairpin” capillary type in myocardium (Kassab and Fung 1994). Due to the rotational symmetry, the gradient azimuth angle was set to zero. Therefore, the enclosed angle of the gradient and main capillary direction (without loss of generality chosen to be along the z-axis, i.e. zenith and azimuth angle of zero) equals the gradient zenith angle. Mean/standard deviation of capillary segment lengths was set to $\mu_l / \sigma_l = 60/40 \mu\text{m}$ (Kaneko et al. 2011) and converted to Weibull shape and scale parameters using approximations (Justus et al. 1978). The capillary flow velocity was set to 0.5 mm/s (Fibich et al. 1993; Callot et al. 2003) and the number of simulated spins was 10^5 .

The simulated parameters ranges were: $\mu_l = 20, 40, 60, 80, 100 \mu\text{m}$, $\sigma_l = 10, 25, 40, 55, 70 \mu\text{m}$; $T_{SE} = 21.06, 63.18, 105.30, 147.42, 189.54 \text{ ms}$, $T_{STEAM} = 272.73, 818.18, 1363.64, 1909.09, 2454.55 \text{ ms}$, $v = 0.1, 0.25, 0.5, 1, 2.5, 5 \text{ mm/s}$, $\kappa = 0, 0.5, 1, 2.5, 3.25, 5, 7.5, 10$.

7.3.4 Ex-vivo data acquisition

A porcine heart was harvested from a female pig (6 months old, weight 60 kg) immediately after cardiac arrest. The animal was euthanized in deep anesthesia with a lethal dose of potassium chloride (100 mg/kg body weight). The heart was subsequently prepared by inserting plastic tubes through the coronary ostia of the aorta into the left and right coronary arteries. The tubes were fixated and sealed by winding rubber bands around the tissue surrounding the plastic tubes. The latter were attached to a connecting tube leading out of the scanner room to connect to a peristaltic pump. The trigger output of the pump was connected to the ECG device of the MRI scanner. The closed fluid circuit was filled with 0.9% NaCl solution. A reservoir was put beneath the heart, which itself was suspended above the fluid level using wire straps which were run through parts of the tissue on top of the heart (i.e. pulmonary artery) and fixated to a plastic container with duct tape. The box including the heart along with a two-channel phased array was placed inside a clinical 1.5T MR system (Philips Healthcare, Best, the Netherlands). Occlusion of the left circumflex (LCX) coronary artery was achieved by pushing the cannulating tube further into the left anterior descending (LAD) artery, thereby sealing the LCX coronary artery branch.

Upon activation of the peristaltic pump (44 rpm, 340 ml/min flow), survey and coil calibration scans were obtained. All DWI acquisitions were acquired according to following schedule: pump activation + 5min waiting time, DWI

scan during perfusion, pump deactivation + 5min waiting time followed by a no-flow baseline scan.

The 2D DWI scan parameters were: FOV=230x110 mm², spatial resolution=2.5x2.5x10 mm³, 43 EPI lines acquired in a single-shot, Local-Look reduced FOV for single-slice acquisition (Buecker et al. 1998), TR=3x60/44 s=4090.91 ms (corresponding to 3 revolutions of the peristaltic pump), TE=148.40/44.65 ms for SE/STEAM, total encoding time $T_{SE} / T_{STEAM} = 105.30 / 1363.64$ ms, spectral pre-saturation with inversion recovery (SPIR) fat suppression and cardiac triggering, b-values=10, 25, 50, 100, 150, 200, 250, 300, 400, 600, 800 and 1000 s/mm². Six optimized (Jones et al. 1999) gradient directions were acquired in both parallel and anti-parallel direction. This allowed for the assessment of bulk flow via phase contrast in order to measure coherent flow in addition to incoherent flow and intermediate regimes. Complex division of the images acquired with inverted gradient waveforms and images obtained with non-inverted waveforms images yielded flow-related phase information while nulling unwanted background phase effects. 2 signal averages were collected, equally distributed across the measurement time. For the occlusion experiment, separate coil sensitivity maps and flow scans were acquired. The parameters were the same as above apart from: TR=1x60/44 s=1363.64 ms (corresponding to 1 revolution of the peristaltic pump), 1 signal average.

Data were reconstructed and processed using MRecon (GyroTools, Winterthur, Switzerland). SNR was calculated voxel-wise using noise samples from calibration pre-scans of each sequence (Nordmeyer-Massner et al. 2009).

7.3.5 Parameter mapping

For IVIM parameter mapping, the two-compartment IVIM tensor model was used (Abdullah et al. 2016). Both diffusion and perfusion are accordingly modeled as diffusion-like Gaussian processes with anisotropy expressed in 3x3 tensors. The model can hence be understood as an extension to DTI and is applicable especially in the case of Normal phase distributions. In contrast to the original scalar IVIM model (Le Bihan et al. 1986), it allows to model anisotropy. Accordingly, diffusion and perfusion were modeled as mono-exponential decays using the diffusion tensor \underline{D} and pseudo-diffusion tensor \underline{D}^* :

$$S(b, \mathbf{e}_g) = S_0 \left[f \cdot \exp(-b \mathbf{e}_g^T \underline{D}^* \mathbf{e}_g) + (1-f) \cdot \exp(-b \mathbf{e}_g^T \underline{D} \mathbf{e}_g) \right], \quad (7.10)$$

where $S(\mathbf{b}, \mathbf{e}_g)$ denotes the measured signal as a function of b-value and gradient direction \mathbf{e}_g , S_0 the signal without diffusion weighting ($b=0$ s/mm²) and f the perfusion fraction. A segmented least-squares approach (Notohamiprodjo et al. 2015; Spinner et al. 2017) was used to fit the logarithm of the measured signal assuming the contribution of the perfusion to reach a maximum of $f/(1-f)$ at $b=0$ s/mm² while becoming negligible for b-values $b \gg b_{\text{split}}$. Accordingly, high b-values ($b \geq b_{\text{split}}=600$ s/mm²) were fitted to a mono-exponential diffusion-only model according to:

$$\log(S(\mathbf{b}, \mathbf{e}_g)) \approx \log(S_{\text{Diff}}(\mathbf{b}, \mathbf{e}_g)) = \log(S_{\text{int}}^{\text{Diff}}) - \mathbf{b} \mathbf{e}_g^T \underline{D} \mathbf{e}_g \quad (7.11)$$

In the second step of the segmented regression, the perfusion related parameters f and \underline{D}^* were estimated using b-values $b < b_{\text{split}}=600$ s/mm², the predetermined diffusion tensor \underline{D} and the mono-exponential intercept $S_{\text{int}}^{\text{Diff}} = S_0(1-f)$. The latter two quantities were used for diffusion signal prediction as stated in Equation (6.2) which was subtracted from the logarithm of the total signal $S(\mathbf{b}, \mathbf{e}_g)$:

$$\begin{aligned} \log(S_{\text{Perf}}(\mathbf{b}, \mathbf{e}_g)) &= \log(S(\mathbf{b}, \mathbf{e}_g)) - \log(S_{\text{Diff}}(\mathbf{b}, \mathbf{e}_g)) \\ &= \log(S_{\text{int}}^{\text{Perf}}) - \mathbf{b} \mathbf{e}_g^T \underline{D}^* \mathbf{e}_g \end{aligned} \quad (7.12)$$

with $S_{\text{int}}^{\text{Perf}} = S_0 f$, yielding the perfusion fraction via $f = S_{\text{int}}^{\text{Perf}} / (S_{\text{int}}^{\text{Diff}} + S_{\text{int}}^{\text{Perf}})$. This approach avoids using images without diffusion weighting ($b=0$ s/mm²) which have different contrast due to the presence of spoiler gradients contributing to the diffusion and perfusion weighting, especially for STEAM imaging. All acquired directions (6 directions both parallel and anti-parallel, yielding 12 in total) were used for the tensor fit. The linear regression was implemented using the proprietary linear solver algorithm in Matlab (Mathworks, Natick, MA). Only positive data were used in the logarithm and subsequent fitting. Negative parameter estimates and the ones derived from a rank deficient system matrix were set to zero. A reduced subset of the ex-vivo occlusion data was analyzed by considering only 4 b-values (10, 200, 600 and 1000 s/mm²) and only 6 directions without gradient inversion, in order to investigate clinical feasibility of a shortened acquisition protocol.

Numerical simulations were performed based on 10⁵ artificial datasets to investigate false-positive apparent perfusion due to noise in a diffusion-only setting. The gradient directions used were the same as used in the ex-vivo

experiments. SNR values ranged from 5 to 150 in steps of 10 and diffusion eigenvalues were $\lambda_1 = 1.25/1.5/2 \cdot 10^{-3}$ mm²/s, $\lambda_2 = 1.25/1.25/1.25 \cdot 10^{-3}$ mm²/s and $\lambda_3 = 1.25/1.00/0.50 \cdot 10^{-3}$ mm²/s, corresponding to FA values of 0.00/0.20/0.54 and an MD of $1.25 \cdot 10^{-3}$ mm²/s. Estimates of the original scalar IVIM model (Le Bihan et al. 1986) were derived using the logarithm of the trace data, segmentation of the b-values and the same linear solver (Spinner et al. 2018).

7.4 Results

7.4.1 Simulations

In Figure 7.3, the phase distributions $\rho(\varphi)$ of normalized phases φ resulting from SE-DWI are seen to deviate from the zero-mean Gaussian distribution of the IVIM model. SE-M0-DWI results in asymmetric distributions around non-vanishing mean values if the diffusion weighting gradients are not orthogonal to the main direction of the capillaries. SE-M1- and SE-M2-DWI do generate distributions centered at zero mean, but depart from Gaussian distributions. In contrast, STEAM-DWI yields Gaussian distributions, with means larger than zero if the gradients are not orthogonal to the main capillary direction.

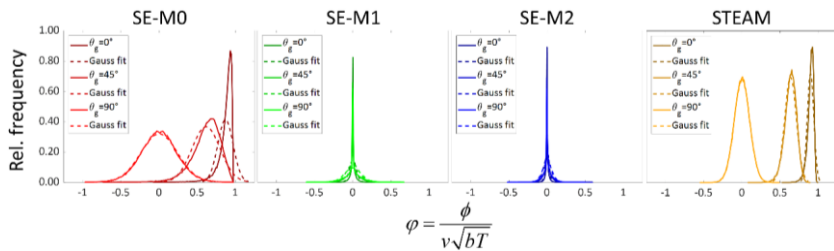


Figure 7.3: Normalized phase distributions. Three gradient (zenith) angles are simulated: parallel to the main capillary direction, at 45° and orthogonal to it. Both SE-M0 and STEAM-DWI sequences exhibit non-vanishing net phases, which increase with decreasing enclosed angles. The motion compensated SE-M1- and SE-M2-DWI sequences yield a mean around zero for all settings. However, the distributions of SE-M1- and SE-M2-DWI deviate from Gaussian distributions, rather approaching Laplacian distributions. In contrast, STEAM-DWI results in the expected Gaussian phases.

The perfusion-induced signal modulations of $|F_p|$ and phase $\angle F_p$ derived from phase distributions $\rho(\varphi)$ are displayed in Figure 7.4. It is seen that the GPA

overestimates signal modulation when using SE-DWI waveforms. In contrast, good GPA correspondence is found for STEAM-DWI. The gradient direction parallel to the main capillary direction yields lowest signal attenuation (all gradient shapes) but maximum phase (SE-M0 and STEAM only), whereas an orthogonal orientation yields maximum magnitude attenuation but no net phase. The magnitude at $b=1000$ s/mm² decreases to 0.48/0.87/0.95/0.18 for SE-M0/SE-M1/SE-M2/STEAM in the case of orthogonal gradients. The maximum phase reached at this b -value is $1.44/0.00/0.00/5.31\pi$ for SE-M0/SE-M1/SE-M2/STEAM in the case of parallel gradients.

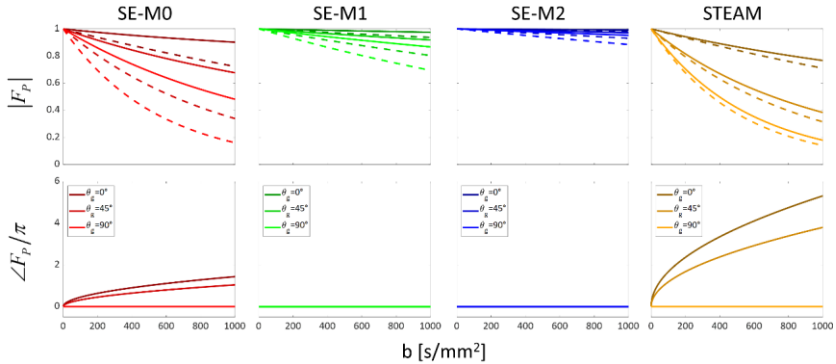


Figure 7.4: Perfusion-induced magnitude and phase modulation. The top row shows absolute values of the signal modulation due to perfusion for three gradient (zenith) angles: parallel to the main fiber direction, at 45° and orthogonal to it (straight lines). The dashed lines are values calculated from a Gaussian Phase Approximation (GPA). The latter is only close to the actual values in case of STEAM. The GPA overestimates the signal attenuation of SE-DWI sequences. The bottom row displays perfusion-induced phase modulation. SE-M1 and SE-M2 do not exhibit relevant phase values across the investigated range of b -values. Both SE-M0 and STEAM produce values of $1.44/5.31\pi$ at 1000 s/mm² if the diffusion weighting gradient is aligned with the main capillary direction.

In Figure 7.5, perfusion-induced magnitude and phases modulations for parameter ranges are analyzed. It is readily seen that SE-M1 and SE-M2 require significantly higher velocities to achieve a desired magnitude signal attenuation when compared to SE-M0 and STEAM. For the investigated SE encoding times of up to 189.54 ms, no SE gradient shape produced a signal attenuation of at least half the signal or more. In contrast, STEAM with the lowest encoding time T_{STEAM} of 272.73 ms (corresponds to a heart rate of about 220 bpm) yields 47% attenuation in one direction. If an isotropic capillary orientation is assumed by

setting the concentration parameter κ to zero and sampling the zenith angle in the interval $[0, 2\pi]$, the magnitudes at $b=500 \text{ s/mm}^2$ are 0.11/0.76/0.91/0.02 for SE-M0/SE-M1/SE-M2/STEAM. If the maximum zenith angle is reduced to 0.5240π (corresponding to unidirectional flow with 6% backflow), the different gradient directions yield different attenuation factors larger or equal to the ones found for the isotropic scenario leading to equal or less signal attenuation. In addition, non-vanishing phase values are generated with SE-M0 and STEAM. These values are highest in case of parallel gradient directions and reach a plateau of about $\max. 1/4\pi$ for $\kappa \geq 5$ for SE-M0/STEAM.

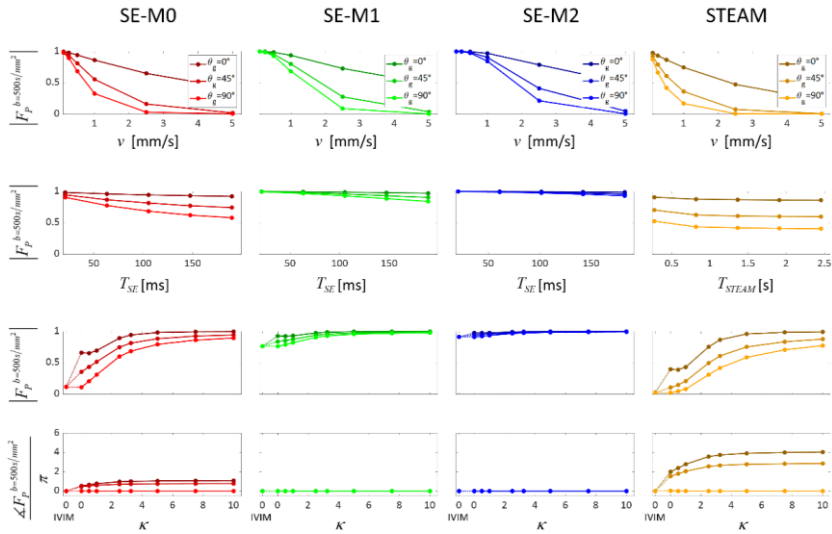


Figure 7.5: Perfusion-induced magnitude and phase modulation. The top row depicts the dependence of signal attenuation at $b=500 \text{ s/mm}^2$ as a function of capillary blood flow velocity v (top row). Velocities below 1 mm/s yield a relatively low attenuation. Longer total encoding times lead to higher signal attenuation (second row). The attenuation decreases with increasing concentration parameter/anisotropy (third row). Both M0-SE and STEAM exhibit net phases if the gradients are non-orthogonal to the main capillary direction (fourth row). The outer left point, marked on the x -axis as “0 IVIM” corresponds to an isotropic capillary segment orientation as assumed in the standard IVIM model.

Gradient lobe durations have a negligible influence on magnitude attenuation and phase generation as shown for SE-M0 and STEAM in Figure 7.10. Also, the

variation of the mean capillary length μ_c and standard deviation σ_c has only a small influence on the magnitude attenuation (Figure 7.11).

7.4.2 Parameter mapping simulations

The MD of the diffusion tensor/scalar diffusion coefficient has a bias lower 10% for $\text{SNR} \geq 15$ and a variation lower 10% for $\text{SNR} \geq 45$ as shown in Figure 7.6. The scalar model shows similar performance in the isotropic case, but exhibits bias with increasing anisotropy. The bias at the highest investigated SNR of 145 is vanishing for the given precision of two digits in all cases apart from the scalar estimates in the anisotropic scenarios, which are $1.24/1.13 \cdot 10^{-3} \text{ mm}^2/\text{s}$ for FA 0.20/0.54. The variation at this SNR is $0.03 \cdot 10^{-3} \text{ mm}^2/\text{s}$ for all FAs.

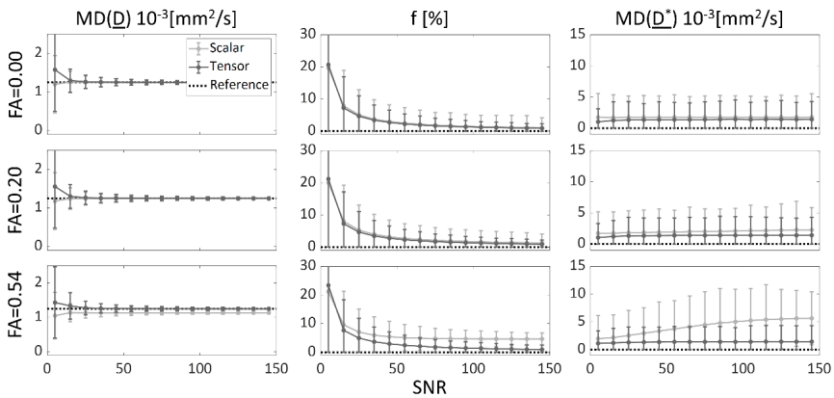


Figure 7.6: Parameter fitting for a diffusion only simulation. Solid lines are estimates from scalar and tensor model fits, the dashed lines correspond to reference values of a diffusion-only scenario (MD of $1.25 \cdot 10^{-3} \text{ mm}^2/\text{s}$) with zero perfusion. Three FAs of 0.00/0.20/0.54 are simulated. A false-positive non-vanishing apparent perfusion can be observed for low SNR (perfusion fraction) and in case of using a segmented model, especially a scalar model in a scenario of anisotropic diffusion (pseudo-diffusion coefficient).

The false-positive detected perfusion fraction falls below 5% (absolute) for all FAs investigated if SNR is equal or larger 25 (tensor fit) or 65 (scalar fit). The SNR thresholds to reach a standard deviation below 5% (absolute) for all FAs investigated are 25 (tensor fit) and 55 (scalar fit). The scalar method exhibits a residual bias which remains present up to the highest $\text{SNR}=145$ investigated in the anisotropic case: the perfusion fraction remains at 5% for a FA of 0.54.

The erroneous non-vanishing MD of the pseudo-diffusion tensor remains virtually constant between $1.02\text{-}1.44\cdot 10^{-3}$ mm²/s within the interval of investigated SNRs, while the scalar estimates are at least $1.73\cdot 10^{-3}$ mm²/s in the isotropic case and reach a plateau of $5.64\cdot 10^{-3}$ mm²/s for FA=0.54. The standard deviations of the tensor estimates also remain virtually constant between $1.52\text{-}1.84\cdot 10^{-3}$ mm²/s. The standard deviations of the scalar estimates are 3.84 to $4.76\cdot 10^{-3}$ mm²/s.

7.4.3 Ex-vivo data

Figure 7.7 summarizes the results of the perfused porcine heart. Magnitude images with STEAM reveal noticeable differences between no-flow baseline and perfusion and hence exhibit observable perfusion sensitivity. In contrast, the SE scans show only minute differences between baseline and perfusion which are further decreased with increasing order of motion compensation. All scans show additional signal attenuation due to water self-diffusion, which is weakest in the STEAM baseline scenario. The superposition of the perfusion influence yields signal attenuations of the STEAM perfusion setting comparable to the SE scans. Interestingly, all scans - including no-flow baseline - show deviations from a purely mono-exponential decay. The influence of different Hamming filter strengths to account for Gibbs ringing especially of the fluid pool is demonstrated in supplemental Figure 7.12. Ringing-like artifacts are visible in the perfusion related maps of the myocardium, especially for unfiltered or weakly filtered images. The SNR values of the $b=0$ s/mm² single-shot images were $55.47\pm 14.37/59.00\pm 15.82/52.42\pm 13.48/13.21\pm 3.35$ for SE-M0/SE-M1/SE-M2/STEAM in the myocardium of the left ventricle.

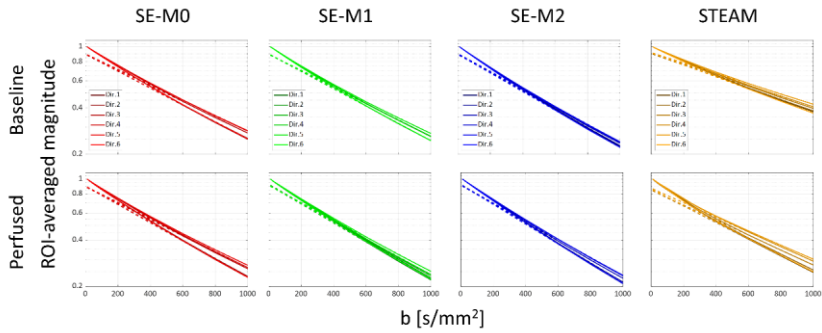


Figure 7.7: Perfused heart experiment. The ROI-average image magnitude of all acquired diffusion encoding directions as function of b -value for SE-M0/SE-M1/SE-M2 and STEAM for both perfused and no-flow states; the dashed lines represent the diffusion-only fits from high b -values ($b \geq 600$ s/mm²) for each direction. Parallel and anti-parallel directions have been averaged.

Figure 7.8 plots magnitude and phase differences between parallel and anti-parallel gradient encoding directions to depict phase-contrast effects in larger vasculature such as epicardial vessels. Figure 7.8 also contains maps of MD and FA for \underline{D} and \underline{D}^* along with a map of perfusion fraction f for STEAM.

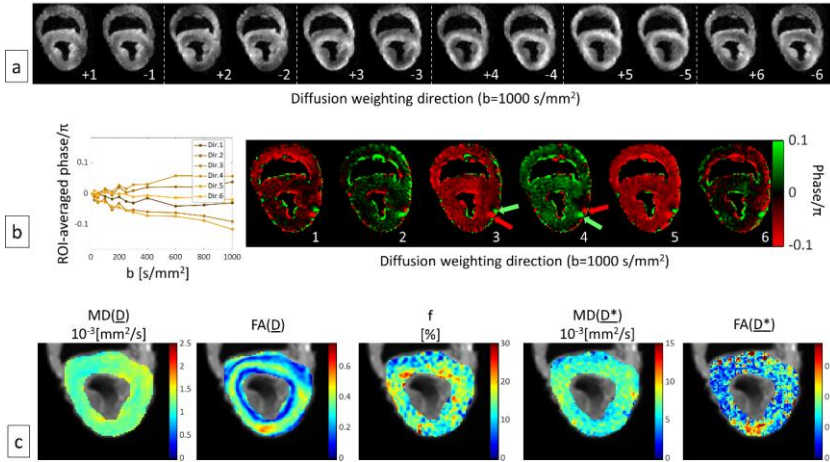


Figure 7.8: Perfused heart experiment using STEAM. Top row: magnitude images of all parallel (+) and anti-parallel (-) gradient directions at the highest investigated b -value (a). Middle row: average phase derived from subtracting the anti-parallel from the parallel gradient direction as a function of b -value and as maps for $b=1000$ s/mm² with arrows indicating two prominent arterial and venous vessels of the LCX branch (b). Bottom row: tensor metrics in terms of MD and FA maps for \underline{D} and \underline{D}^* along with a map of perfusion fraction f (c).

Table 7.1 summarizes MDs of \underline{D} and \underline{D}^* along with perfusion fraction f for all sequence types. For all sequences, higher MDs of \underline{D} and \underline{D}^* are detected for the perfused case versus no-flow baseline. The perfusion fraction for SE-M0/SE-M1/SE-M2 is lower during perfusion compared to no-flow baseline. In contrast, the perfusion fraction in STEAM is about 50% (relative) higher during perfusion compared to baseline. The variation of the MD of the pseudo-diffusion tensor for the two scenarios is within 6% for SE scans. Moreover, the MD of the pseudo-diffusion tensor is lower in the perfusion scans for both SE-M1 and SE-M2. STEAM generates an increase of about 42% in MD of the pseudo-diffusion tensor and 129% in $f \cdot \text{MD}(\underline{D}^*)$ during perfusion when compared to baseline.

Seq.	Meas.	MD(<u>D</u>)	FA(<u>D</u>)	f	MD(<u>D</u> *)	FA(<u>D</u> *)	f·MD(<u>D</u> *)
		10 ⁻³ [mm ² /s]		[%]	10 ⁻³ [mm ² /s]		[%] · 10 ⁻³ [mm ² /s]
SE-M0	Baseline	1.24 ± 0.13	0.19 ± 0.08	10.78 ± 1.85	5.60 ± 0.55	0.13 ± 0.09	60.68 ± 12.53
	Perfusion	1.32 ± 0.11	0.19 ± 0.08	10.72 ± 2.83	5.70 ± 0.84	0.19 ± 0.14	62.30 ± 21.22
SE-M1	Baseline	1.27 ± 0.11	0.15 ± 0.07	10.97 ± 3.91	5.00 ± 1.55	0.22 ± 0.20	57.52 ± 26.79
	Perfusion	1.39 ± 0.10	0.13 ± 0.06	8.74 ± 3.66	4.73 ± 1.65	0.24 ± 0.21	43.79 ± 23.01
SE-M2	Baseline	1.36 ± 0.15	0.11 ± 0.05	11.81 ± 2.15	5.77 ± 0.67	0.11 ± 0.07	68.11 ± 14.18
	Perfusion	1.44 ± 0.11	0.13 ± 0.06	9.42 ± 1.83	5.52 ± 0.63	0.12 ± 0.09	52.31 ± 12.09
STEAM	Baseline	0.87 ± 0.14	0.26 ± 0.11	8.12 ± 3.73	4.45 ± 1.60	0.32 ± 0.23	38.80 ± 22.59
	Perfusion	1.21 ± 0.12	0.27 ± 0.12	13.60 ± 4.48	6.33 ± 1.47	0.29 ± 0.18	89.02 ± 37.35

Table 7.1: Ex-vivo IVIM parameters as mean ± standard deviation for the different DWI sequences (seq.) and measurements (meas.).

In supplemental Figure 7.13, measurement reproducibility of the ex-vivo experiments is provided using Bland-Altman plots. The means and standard deviations of the difference of the two repetitions are -0.02/0.80/0.19 and 0.02/2.72/0.83 for MD(D) / f / MD(D*) given in 10⁻³mm²/s / % / 10⁻³mm²/s.

Figure 7.9 summarizes STEAM results of the coronary occlusion experiment. Reduced MDs of D and D* along with f are seen corresponding to the LCX territory for both the full and a reduced dataset. Phase-contrast maps derived from STEAM reveal flow through larger epicardial vessels. Histograms of the IVIM parameters in the infarct and remote regions (manually segmented based on the perfusion fraction map derived from the full dataset) together with IVIM parameter maps from a reduced dataset are shown in supplemental Figure 7.14.

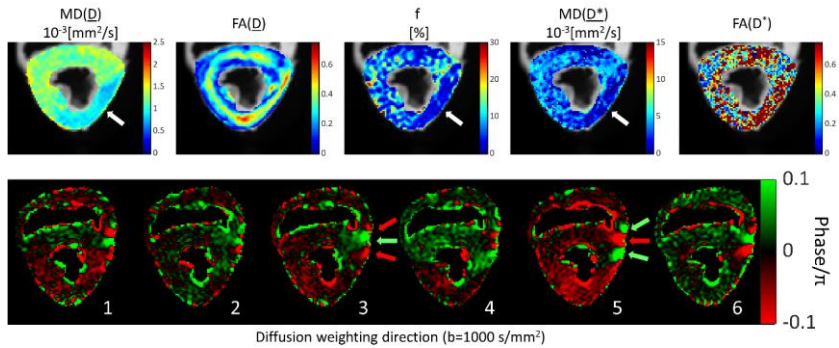


Figure 7.9: Perfused heart experiment with occlusion of the left circumflex artery (LCX) using STEAM. Reduced $MD(\underline{D})$, f and $MD(\underline{D}^*)$ are seen in the ischemic LCX territory (white arrows). Phase maps from phase-contrast STEAM confirm no flow in the LCX but perfusion in interventricular vessels (green & red arrows).

7.5 Discussion

In the present work, computer simulations and experimental imaging have been used to assess and compare the IVIM encoding efficiency of SE and STEAM based cardiac DWI/DTI to investigate perfusion in the heart. For typical properties of the capillary network in the myocardium and typical scan settings with b -values below 1000 s/mm^2 , SE sequences exhibit a low perfusion sensitivity, which decreases further if motion-compensated diffusion gradients are employed. In contrast, STEAM provides sufficient magnitude contrast to detect changes in myocardial perfusion as demonstrated during experimental coronary occlusion of a perfused heart. It was shown that the diffusion encoding STEAM sequence allows for phase-contrast by using gradient reversal. Therefore, probing of the whole motion spectrum of blood flow is possible: incoherent intravoxel motion in the myocardial capillaries, largely coherent flow in epicardial vessels and intermediate regimes. The present study has also demonstrated that Gaussian phase approximation only holds for STEAM sequences, while careful considerations of the validity of the Gaussian assumptions are required with SE.

Using simulations, the present study has shown that low SNR data yields parameter biases both with the original scalar IVIM model (Spinner et al. 2017; While 2017) and with the IVIM tensor model. To this end, elevated perfusion fractions (tensor & scalar fit) result even in a perfusion-free scenario. To prevent such false-positive findings, effective SNR should at least be 25 when

using the IVIM tensor model, which was achieved here given two signal averages and using both gradient signs. The SNR found in this study are in line with literature for SE/STEAM (von Deuster et al. 2016b), where STEAM was also found to be disadvantageous in this regard. Furthermore, images are confounded by partial volume effects due to low spatial resolution and consequential signal leakage caused by Gibbs ringing. We attribute parts of the non-vanishing false positive perfusion estimates in the no-flow baseline data to this aspect.

It should be emphasized that an anisotropic IVIM model is recommended in the heart given the anisotropic nature of the capillary networks (Kaneko et al. 2011) in accordance to the fiber aggregate architecture of the myocardium (Stoeck et al. 2014; Nguyen et al. 2014; Stoeck et al. 2016; NIELLES-Vallespin et al. 2017; Scott et al. 2018). The tensor model presented here is applicable if sufficient encoding gradient directions and SNR as stated above are available. An alternative to the IVIM tensor model is the IVPCM model (Karampinos et al. 2010), which parameterizes anisotropy with only one parameter (concentration of the von Mises distribution). Further investigations into IVIM can also consider the T_1 and T_2 relaxation effects to account for the different contributions of the compartments for different sequences and their respective timing parameters (Lemke et al. 2010; Moulin et al. 2016).

An ex-vivo porcine heart was used as a substitute in order to control all relevant parameters. In general, cardiac studies in pigs translate well to humans because of the similar structure, shape and size of the organ. It should, however, be noted that ex-vivo tissue may suffer from degradation in the form of cell death and cessation of active transport, which can potentially alter the diffusive and perfusion properties. Here we nevertheless found good agreement between ex-vivo and in-vivo SE-M2 DTI (47), indicating largely unchanged diffusion properties. In addition, exchange between the intra-vascular and extra-vascular compartments take place in-vivo, which also affects the perfusion contribution of the signal. Cardiac STEAM encodes over two consecutive heart-beats and is therefore more affected by such effects compared to SE with a relatively short intra-heartbeat encoding time. Future studies may incorporate a kinetic model (Sourbron and Buckley 2012), in order to assess the effect of water exchange. STEAM has been successfully used for IVIM in an animal model (Callot et al. 2003), indicating that perfusion detection is achievable despite the presence of exchange between compartments. The iso-osmolar saline solution used for perfusion in our studies differs from blood by its temperature, composition and different diffusion properties (46). The diffusion and perfusion parameters of an in-vivo measurement can therefore differ from the ex-vivo values found in this study.

In the ex-vivo measurements it was noted that the mean diffusivities increased by 2/10% (baseline) for first and second-order gradient moment compensation compared to SE-M0, which was also found in simulations of the SE-M0 and SE-M2 gradient waveforms (Rose et al. 2019). Detailed data analysis revealed that this increase is primarily driven by increased measured diffusivity along the secondary and tertiary eigenvectors while diffusivity along the primary eigenvector agreed well. This observation may be explained by motional narrowing in the presence of diffusion boundaries orthogonal to the main capillary axes i.e. along the secondary and tertiary eigenvectors.

The IVIM perfusion fraction $f = \text{MBV}/f_w$ represents the relative compartment weight of flowing blood with myocardial blood volume (MBV [ml/g]) and MR-detectable water fraction (f_w). It therefore indicates the vessel density and size. The perfusion fraction was found to be elevated in the vicinity of the interventricular vessels in the ex-vivo perfusion experiment and was reduced to values close to zero in ischemic areas. The pseudo-diffusion coefficient or tensor respectively from Equation (7.12), which is $D^* = \langle l \rangle \langle v \rangle / 6$ in the IVIM model (Le Bihan and Turner 1992) with mean capillary length $\langle l \rangle$ and mean velocity $\langle v \rangle$ depends on the number of capillary branches traversed. It was also found to be increased around the LV-RV intersections ex-vivo and reduced to values around zero in ischemic regions. Further relations of the IVIM parameters to physiological perfusion quantities such as mean transit time (MTT [s]) and myocardial blood flow (MBF [ml/min/g]) are: $\text{MTT} = L \langle l \rangle / 6 D^*$ and $\text{MBF} = (6 f_w / L \langle l \rangle) f D^*$ with total capillary length L (Le Bihan and Turner 1992). These relations potentially allow to derive perfusion parameters from IVIM surrogates. Of note, the IVIM perfusion tensor/coefficients as introduced here also require correction for the diffusivity of the perfusion fluid (Funck et al. 2018) if true perfusion quantification is aimed at.

The maximum investigated b-value of 1000 s/mm^2 is difficult to achieve in-vivo. However, as it was shown in simulations and ex-vivo here, the perfusion-related signal of STEAM is still relevant for typical in-vivo b-values of about 500 s/mm^2 .

In a segmented fit, this yielded elevated mean diffusivities that can influence the perfusion parameter estimates. This fit artifact can be addressed by a separation of the two compartments by acquiring several high b-value images where diffusion is dominant in conjunction with a non-segmented iterative non-linear fit procedure. Hence, by using non-linear iterative solvers instead of taking the logarithm of the data as used here, improvements of the parameter estimation procedure may be achieved – at the expense of longer computation

time. As stated above, parts of the residual biases seen in our study likely result from data segmentation, which could also be improved by a variable threshold (Wurnig et al. 2015). Moreover, a hierarchical Bayesian model (Orton et al. 2014; Spinner et al. 2017) with a Gaussian mixture prior to account for the different tissue types present can potentially improve parameter estimation.

In addition, phase values derived from data acquired with standard diffusion gradient and inverted gradient waveforms can be used to aid parameter estimation. The accuracy of phase estimates can potentially benefit from common phase-contrast background phase correction methods (Giese et al. 2012; Busch et al. 2017).

7.6 Conclusion

Given the short diffusion encoding time of typical spin-echo based DWI/DTI sequences, a very limited sensitivity to myocardial perfusion is present. In combination with motion-compensated diffusion gradients as required for in-vivo cardiac DWI/DTI, the low perfusion sensitivity decreases further. This renders the extraction of meaningful IVIM parameters by using cardiac spin-echo DWI/DTI very challenging, especially under resting conditions. In contrast, stimulated-echo based DWI/DTI yields detectable differences between no-flow and perfused myocardium, potentially allowing to identify regional perfusion changes based on IVIM parameters in the in-vivo human heart.

7.7 Appendix

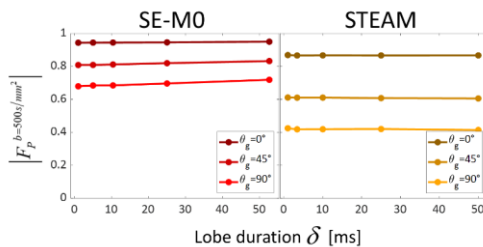


Figure 7.10: Magnitude attenuation vs. gradient lobe duration for SE-MO and STEAM. Three different gradient directions are shown: parallel to main fiber direction, 45° offset and orthogonal to it. The maximum shown gradient lobe duration of SE-MO is the maximum value for the given total encoding time of 105.30 ms for SE-MO (1363.64 ms for STEAM).

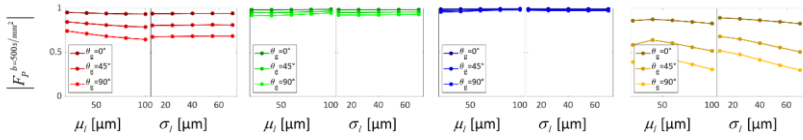


Figure 7.11: Magnitude attenuation vs. mean and standard deviation of the capillary segment length for SE-M0/SE-M1/SE-M2 and STEAM. Their dependence is negligible over the investigated intervals.

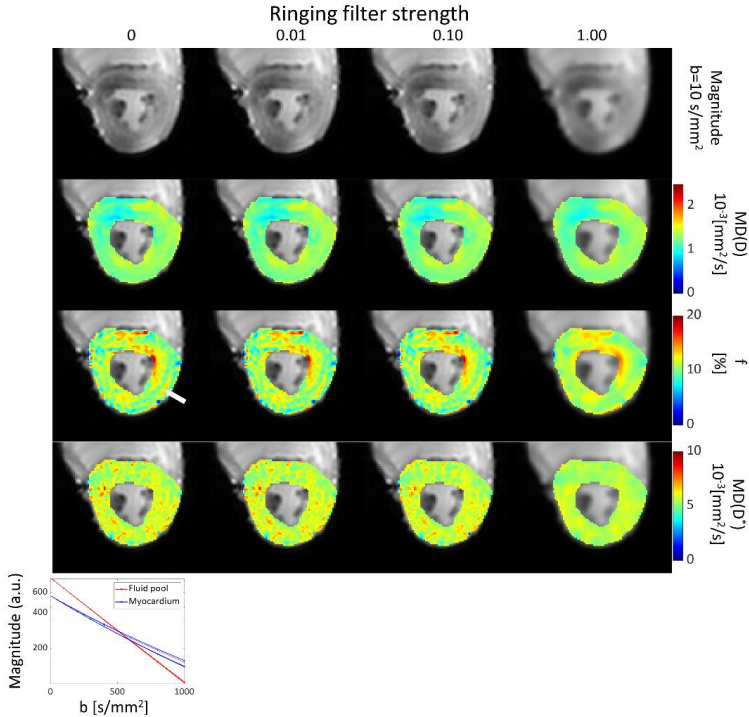


Figure 7.12: Magnitude and IVIM parameter maps for different Gibbs ringing filter strengths. A Hamming filter strength of 0 means that no filter is applied while a strength of 1 reduces the values at the border of k -space to 0 (likewise 0.5 corresponds to 50% reduction). Ringing-like artifacts are visible in the perfusion fraction for filter strengths below 1 (white arrow). The ROI-average magnitudes (all gradient directions) versus b -value in the myocardium and fluid pool show the different diffusive behaviors, which can lead to falsely detected apparent perfusion if the two compartments are mixed.

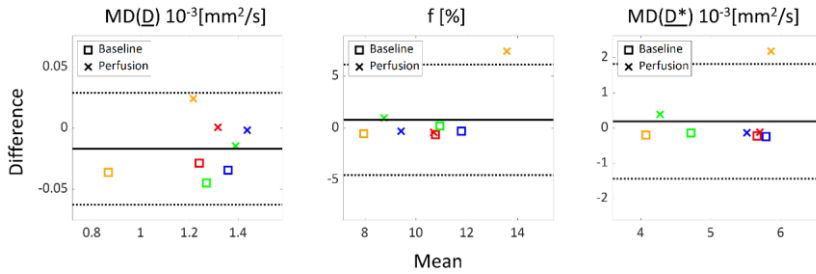


Figure 7.13: Bland-Altman plots of ex-vivo repeat experiments. The solid lines display the mean of the two signal averages of all data points, the dashed lines represent the $\text{mean} \pm 1.96$ -standard deviation. Red/green/blue/orange markers indicate SE-M0/SE-M1/SE-M2/STEAM.

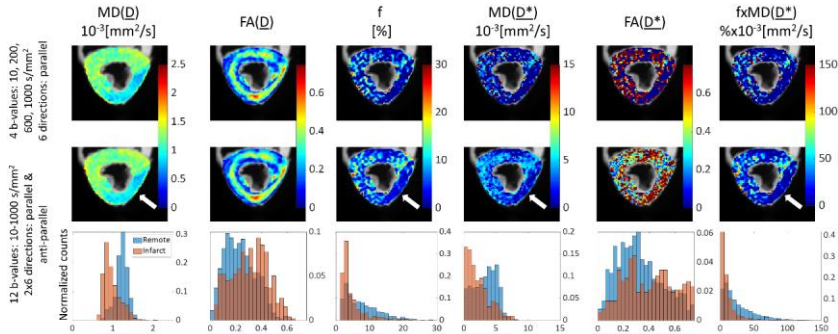


Figure 7.14: Perfused heart experiment with occlusion of the left circumflex artery (LCX) using STEAM with full and reduced set of DWIs. Reduced $\text{MD}(\underline{D})$, f and $\text{MD}(\underline{D}^*)$ are seen in the ischemic LCX territory (white arrows) for both the full (12 b-values, parallel & anti-parallel diffusion encoding directions) and the reduced dataset (4 b-values, parallel diffusion encoding direction only). The corresponding histograms (bar height equals counts divided by total number of voxels in respective region-of-interest) of $\text{MD}(\underline{D})$, f and $\text{MD}(\underline{D}^*)$ for the full dataset confirm the observations of reduced IVIM parameters in the infarcted region compared to the remote part.

Chapter 8

Summary

IVIM imaging is a powerful non-invasive contrast agent free tool to estimate tissue perfusion and hence it has the potential to serve as an alternative to conventional contrast agent enhanced methods. Such a tool may find numerous applications in diagnosis and treatment monitoring in many of the most prevalent pathologies: CVDs, cancer and dementia to name a few.

In this thesis, major limitations of IVIM imaging such as the long image readouts, parameter estimation uncertainty and questions concerning model foundations have been addressed. First, a method for accelerated IVIM imaging has been presented in the brain. Second, improved IVIM parameter estimation in the heart has been shown in simulations and in-vivo. Finally, an investigation of the IVIM model in the heart beyond its original assumptions has been proposed in theory, simulations and using ex-vivo cardiac data.

8.1 Discussion

The accelerated IVIM technique in Chapter 5 has demonstrated for the first time that undersampling beyond the limits of parallel imaging and successful IVIM parameter estimation from such data is possible. More specifically, an undersampling factor of 6 is achievable, where conventional methods allowed only up to about net 3-fold undersampling. This is particularly useful for brain IVIM scans, because of the large field-of-view and the required resolution. The proposed k-b PCA approach exploits signal correlations in space and along the many diffusion weighted images with different diffusion strengths and directions as needed for IVIM. As it has been shown, a few lines in the k-space center for the regularization of the optimization procedure are sufficient to regularize the image reconstruction task. Optimization was performed with linear LSQ methods where parameter tuning has not been found to be a critical issue. In addition, the amount of data provided in a standard IVIM acquisition is more than sufficient for reconstruction. The deployment of the method on a clinical 3T scanner demonstrated that typical single-shot EPI artifacts such as geometric deformations, signal smearing and build-up could be reduced to the level of standard morphological imaging. The resulting IVIM parameter maps were qualitatively similar to conventional fully sampled reference acquisitions.

Conventionally, IVIM parameter estimation is performed without prior knowledge using a MLE, respectively LSQ procedure. The proposed Bayesian

hierarchical approach takes into consideration the relatively homogeneous perfusion properties of the myocardium. While still providing parameters on a voxel-wise basis, this approach regularizes parameter estimation with information from other voxels in the region-of-interest. While the approach results in smooth parameter maps without outliers, the detection of perfusion defects was still possible. Moreover, the Bayesian approach provides measures of estimation uncertainty depending on input data. Since this method no longer performs point estimation, conventional optimization methods are no longer adequate. To this end, the dedicated MCMC sampler has been optimized to handle vectorized data.

In the third project, the origin and nature of perfusion-induced signal modulations in DWI experiments were studied. The specific structure of capillaries was addressed in Monte Carlo simulations. The full temporal evolution of commonly used diffusion weighted gradient waveforms as in cardiac DWI/DTI was considered. The simulations revealed that higher-order motion compensation of diffusion encoding gradient waveforms reduces perfusion sensitivity. On the other hand, long encoding times as present with STEAM allow for sufficient perfusion sensitivity. The capillary anisotropy translates to both magnitude and phase variation depending on gradient orientation and strength. Ex-vivo data from a porcine heart confirmed these findings. Hence, deviations from the standard IVIM model need to be addressed. In addition, diffusion weighting gradient waveforms exhibit different perfusion sensitivities. These results indicate that assumptions of the IVIM model can be violated with standard DWI/DTI approaches. Hence, the model simplifications might be inadequate to capture the complex interaction of motion encoding gradients and flowing blood in the microvasculature in particular IVIM imaging settings and a more complex signal model is required.

8.2 Outlook

Beyond the data shown in this work, scan acceleration using the proposed k-b PCA method can be used to address EPI artifacts in particular at very high magnetic field strengths, which hold potential for a wide range of neurological imaging applications. On the other hand, k-b PCA could also be used to obtain finer resolution. This would be of great benefit for acute stroke patients for example. They routinely undergo DWI to determine the extension of the edema besides perfusion measurement. The determination of the volume of the tissue-at-risk (also called “penumbra”) is of great importance, because volume thresholds in guidelines determine the decision to treat via an early intervention. Therefore, IVIM could provide both DWI and perfusion estimation to determine the volume of the tissue which can be salvaged. In addition,

diagnosis of other neurological pathologies, such as cancer for example, would benefit from an increased resolution.

The requirement of fully sampled training data in k-b PCA limits scan acceleration, but also provides valuable information for autocalibration of parallel imaging. This can be beneficial if the method is translated to the in-vivo heart. Residual motion of the heart often occurs even after applying various motion compensation strategies to tackle breathing and contractile motion. This poses a problem for SENSE reconstructions, because the previously acquired coil sensitivity maps might be misaligned relative to the acquired data. Autocalibration methods derive such maps from the k-space center of every image. Moreover, such fully sampled low-resolution data provides valuable phase and magnitude information, which can be used in subsequent registration procedures, which are required once the method is translated to the heart. Using k-b PCA in the heart together with reduced field-of-view techniques, the ambitious goal of a single-shot 3D whole heart acquisition might become feasible.

The Bayesian approach to parameter estimation in Chapter 6 proves that prior knowledge can greatly improve parameter estimation of difficult inversion problems. From a technical point of view, MCMC sampling could be deployed in dedicated statistics software such as BUGS-like programs, JAGS or STAN or Google's TensorFlow Probability. This allows to harvest the progresses made in the field of statistical computing. Faster parameter fitting and enhanced Markov chain monitoring would result. Such software also allows for relatively easy modifications or implementation of other models. In this thesis, a mono-modal Gaussian prior was used for a rather homogeneous region-of-interest. A double- or multi-modal prior in the form of a Gaussian mixture model for example could potentially better handle other relevant data: large myocardial infarcts for example exhibit severely reduced or suspended perfusion, which propagates into the measured IVIM perfusion surrogates. Hence, the sum of two Gaussians could be considered, with one mode at zero perfusion. Likewise, a tri-modal prior in the brain can be proposed due to the presence of white matter, gray matter and CSF areas. In general, the number of components of a mixture model can be considered a random variable itself. Hence, a prior such as a Dirichlet distribution for example could be used for the number of components in the mixture to allow for automatic clustering during parameter estimation. Another potential use for complex multi-hierarchical and multivariate models is the combined processing of multimodal data (IVIM, T_1 mapping, T_2 mapping etc.) to enhance diagnostic certainty. Bayesian methods can handle such tasks in a natural manner. If speed is of utmost importance, for example in real-time applications, variational Bayes methods are an

alternative to MCMC, albeit at the cost of lengthy derivations of the necessary equations.

The investigation into the IVIM model itself in Chapter 7 has shown that its assumptions and idealizations are not justifiable in all imaging situations. Even though SE-based diffusion-weighted imaging has proven to be a reliable, robust and successful tool to probe the cardiac microstructure via DTI, its usability for IVIM is limited. While higher-order motion compensation reduces the sensitivity towards myocardial strain it also reduces the perfusion sensitivity. The classical Stejskal-Tanner sequence without higher order motion compensation but with dedicated post-processing has been successfully used for IVIM in diastole. Systolic imaging on the other hand is prohibited with this sequence because of the rapid cardiac contraction. Still, the achievable echo times are around or below 100 ms in diastole, which allows only for very few directional changes of the flowing blood. In addition, such long echo times are accompanied with considerable signal loss due to transversal relaxation. STEAM on the other hand provides suitable diffusion/mixing times, which is sufficient even for elevated heart rates. Signal loss because of longitudinal relaxation is not as severe as with long echo times in a SE experiment. However, STEAM requires breath holding and gating of breathing motion to achieve reproducible motion states of the heart between two consecutive heartbeats which in turn results in reduced scan efficiency compared to SE. Nevertheless, STEAM is preferred over SE for cardiac IVIM to achieve sufficient perfusion sensitivity. Next to appropriate data acquisition, the capillary anisotropy should be considered in the interpretation of cardiac IVIM data. Hence, besides magnitude information, also phase should be taken into account. The presented results also indicate that any IVIM parameter depends on the sequence used and its timing, which challenges comparability of different measurements with divergent settings. Furthermore, it is conceivable, that IVIM imaging of other organs also need further investigation in terms of the validity of the IVIM model. This has already been studied for pancreas and liver for example. However, IVIM imaging has also been performed in many other organs such as the brain, kidneys, prostate etc. Besides the issues of short diffusion time and velocity encoding versus displacement encoding, the microvasculature in many organs is known to be anisotropic.

Bibliography

- Abdullah OM, Gomez AD, Merchant S, Heidinger M, Poelzing S, Hsu EW (2016) *Orientation dependence of microcirculation-induced diffusion signal in anisotropic tissues*. *Magnetic Resonance in Medicine* 76(4):1252–1262. doi: 10.1002/mrm.25980
- Al-Saadi N, Nagel E, Gross M, Bornstedt A, Schnackenburg B, Klein C, Klimek W, Oswald H, Fleck E (2000) *Noninvasive detection of myocardial ischemia from perfusion reserve based on cardiovascular magnetic resonance*. *Circulation* 101(12):1379–83. doi: 10.1161/01.CIR.101.12.1379
- Aletras AH, Ding S, Balaban RS, Wen H (1999) *DENSE: Displacement Encoding with Stimulated Echoes in Cardiac Functional MRI*. *Journal of Magnetic Resonance* 137(1):247–252. doi: 10.1006/jmre.1998.1676
- Aliotta E, Moulin K, Ennis DB (2018) *Eddy current-nulled convex optimized diffusion encoding (EN-CODE) for distortion-free diffusion tensor imaging with short echo times*. *Magnetic Resonance in Medicine* 79(2):663–672. doi: 10.1002/mrm.26709
- Aliotta E, Wu HH, Ennis DB (2017) *Convex optimized diffusion encoding (CODE) gradient waveforms for minimum echo time and bulk motion-compensated diffusion-weighted MRI*. *Magnetic Resonance in Medicine* 77(2):717–729. doi: 10.1002/mrm.26166
- Althoefer C, Kaiser H-J, Dörr R, Feinendegen C, Beilin I, Uebis R, Buell U (1992) *Fluorine-18 deoxyglucose PET for assessment of viable myocardium in perfusion defects in 99mTc-MIBI SPET: a comparative study in patients with coronary artery disease*. *European Journal of Nuclear Medicine* 19(5):334–342. doi: 10.1007/BF00177055
- Bammer R, Keeling SL, Augustin M, Pruessmann KP, Wolf R, Stollberger R, Hartung HP, Fazekas F (2001) *Improved diffusion-weighted single-shot echo-planar imaging (EPI) in stroke using sensitivity encoding (SENSE)*. *Magnetic Resonance in Medicine* 46(3):548–554. doi: 10.1002/mrm.1226
- Basser PJ, Mattiello J, LeBihan D (1994) *MR diffusion tensor spectroscopy and imaging*. *Biophysical Journal* 66(1):259–67. doi: 10.1016/S0006-3495(94)80775-1
- Berger JO, Bernardo JM, Sun D (2009) *The formal definition of reference priors*. *Annals of Statistics* 37(2):905–938. doi: 10.1214/07-AOS587

- Binter C, Knobloch V, Manka R, Sigfridsson A, Kozerke S (2013) *Bayesian multipoint velocity encoding for concurrent flow and turbulence mapping*. *Magnetic Resonance in Medicine* 69(5):1337–45. doi: 10.1002/mrm.24370
- Bishop C (2006) *Pattern Recognition and Machine Learning*. Springer New York
- Bloch F (1946) *Nuclear Induction*. *Physical Review* 70(7–8):460–474. doi: 10.1103/PhysRev.70.460
- Buecker A, Adam G, Neuerburg JM, Glowinski A, van Vaals JJ, Guenther RW (1998) *MR-guided biopsy using a T2-weighted single-shot zoom imaging sequence (Local Look technique)*. *Journal of Magnetic Resonance Imaging* 8(4):955–9
- Busch J, Giese D, Kozerke S (2017) *Image-based background phase error correction in 4D flow MRI revisited*. *Journal of Magnetic Resonance Imaging* 46(5):1516–1525. doi: 10.1002/jmri.25668
- Callaghan PT, Jolley KW, Lelievre J (1979) *Diffusion of water in the endosperm tissue of wheat grains as studied by pulsed field gradient nuclear magnetic resonance*. *Biophysical Journal* 28(1):133–141. doi: 10.1016/S0006-3495(79)85164-4
- Callot V, Bennett E, Decking UKM, Balaban RS, Wen H (2003) *In vivo study of microcirculation in canine myocardium using the IVIM method*. *Magnetic Resonance in Medicine* 50(3):531–540. doi: 10.1002/mrm.10568
- Candes EJ, Romberg J, Tao T (2006) *Robust Uncertainty Principles : Exact Signal Frequency Information*. *IEEE Transactions on Information Theory* 52(2):489–509. doi: 10.1109/TIT.2005.862083
- Carpenter B, Gelman A, Hoffman MD, Lee D, Goodrich B, Betancourt M, Brubaker M, Guo J, Li P, Riddell A (2017) *Stan: A probabilistic programming language*. *Journal of Statistical Software* 76(1):1–32. doi: 10.18637/jss.v076.i01
- Chan TF, Vese L a. (2001) *Active contours without edges*. *IEEE Transactions on Image Processing* 10(2):266–277. doi: 10.1109/83.902291
- Cleveland GG, Chang DC, Hazlewood CF, Rorschach HE (1976) *Nuclear magnetic resonance measurement of skeletal muscle: anisotropy of the diffusion coefficient of the intracellular water*. *Biophysical Journal* 16(9):1043–53. doi: 10.1016/S0006-3495(76)85754-2
- Daubechies I (1988) *Orthonormal bases of compactly supported wavelets*. *Communications on Pure and Applied Mathematics* 41(7):909–996. doi:

10.1002/cpa.3160410705

- Delattre BM a, Viallon M, Wei H, Zhu YM, Feiweier T, Pai VM, Wen H, Croisille P (2012) *In vivo cardiac diffusion-weighted magnetic resonance imaging: quantification of normal perfusion and diffusion coefficients with intravoxel incoherent motion imaging*. Investigative Radiology 47(11):662–70. doi: 10.1097/RLI.0b013e31826ef901
- Deux J-F, Maatouk M, Vignaud A, Luciani A, Lenczner G, Mayer J, Lim P, Dubois-Randé J-L, Kobeiter H, Rahmouni A (2011) *Diffusion-weighted echo planar imaging in patients with recent myocardial infarction*. European Radiology 21(1):46–53. doi: 10.1007/s00330-010-1912-6
- Dillon J V., Langmore I, Tran D, Brevdo E, Vasudevan S, Moore D, Patton B, Alemi A, Hoffman M, Saurous RA (2017) *TensorFlow Distributions*. arxiv.org/abs/171110604
- Edelman RR, Gaa J, Wedeen VJ, Loh E, Hare JM, Prasad P, Li W (1994) *In vivo measurement of water diffusion in the human heart*. Magnetic Resonance in Medicine 32(3):423–8. doi: 10.1002/mrm.1910320320
- Einstein A (1905) *Über die von der molekularkinetischen Theorie der Wärme geforderte Bewegung von in ruhenden Flüssigkeiten suspendierten Teilchen*. Annalen Der Physik 322(8):549–560. doi: 10.1002/andp.19053220806
- Ernst RR (1966) *Application of Fourier transform spectroscopy to magnetic resonance*. Review of Scientific Instruments 37(1):93–102. doi: 10.1063/1.1719961
- Fang ZY, Prins JB, Marwick TH (2004) *Diabetic cardiomyopathy: evidence, mechanisms, and therapeutic implications*. Endocrine Reviews 25(4):543–567. doi: 10.1210/er.2003-0012
- Farzaneh F, Riederer SJ, Pelc NJ (1990) *Analysis of T2 limitations and off-resonance effects on spatial resolution and artifacts in echo-planar imaging*. Magnetic Resonance in Medicine 14(1):123–39. doi: 10.1002/mrm.1910140112
- Federau C, Cerny M, Roux M, Mosimann PJ, Maeder P, Meuli R, Wintermark M (2017) *IVIM perfusion fraction is prognostic for survival in brain glioma*. Clinical Neuroradiology 27(4):485–492. doi: 10.1007/s00062-016-0510-7
- Federau C, Maeder P, O'Brien K, Browaeys P, Meuli R, Hagmann P (2012) *Quantitative measurement of brain perfusion with intravoxel incoherent motion MR imaging*. Radiology 265(3):874–81. doi: 10.1148/radiol.12120584

- Federau C, O'Brien K, Birbaumer A, Meuli R, Hagmann P, Maeder P (2015) *Functional mapping of the human visual cortex with intravoxel incoherent motion MRI*. *PLoS One* 10(2):e0117706. doi: 10.1371/journal.pone.0117706
- Federau C, O'Brien K, Meuli R, Hagmann P, Maeder P (2014) *Measuring brain perfusion with intravoxel incoherent motion (IVIM): initial clinical experience*. *Journal of Magnetic Resonance Imaging* 39(3):624–632. doi: 10.1002/jmri.24195
- Feinberg DA, Hale JD, Watts JC, Kaufman L, Mark A (1986) *Halving MR imaging time by conjugation: demonstration at 3.5 kG*. *Radiology* 161(2):527–531. doi: 10.1148/radiology.161.2.3763926
- Feinberg DA, Hoenninger JC, Crooks LE, Kaufman L, Watts JC, Arakawa M (1985) *Inner volume MR imaging: technical concepts and their application*. *Radiology* 156(3):743–747. doi: 10.1148/radiology.156.3.4023236
- Fibich G, Lanir Y, Liron N (1993) *Mathematical model of blood flow in a coronary capillary*. *The American Journal of Physiology* 265(5 Pt 2):H1829-40. doi: 10.1152/ajpheart.1993.265.5.H1829
- Fischer SE, Stuber M, Scheidegger MB, Boesiger P (1995) *Limitations of stimulated echo acquisition mode (steam) techniques in cardiac applications*. *Magnetic Resonance in Medicine* 34(1):80–91. doi: 10.1002/mrm.1910340113
- Frahm J, Merboldt KD, Hänicke W, Haase A (1985) *Stimulated echo imaging*. *Journal of Magnetic Resonance* (1969) 64(1):81–93. doi: 10.1016/0022-2364(85)90033-2
- Freiman M, Perez-Rossello JM, Callahan MJ, Voss SD, Ecklund K, Mulkern R V., Warfield SK (2013) *Reliable estimation of incoherent motion parametric maps from diffusion-weighted MRI using fusion bootstrap moves*. *Medical Image Analysis* 17(3):325–336. doi: 10.1016/j.media.2012.12.001
- Froeling M, Strijkers GJ, Nederveen AJ, Chamuleau S a, Luijten PR (2014) *Feasibility of in vivo whole heart DTI and IVIM with a 15 minute acquisition protocol*. *Journal of Cardiovascular Magnetic Resonance* 16(Suppl 1):O15. doi: 10.1186/1532-429X-16-S1-O15
- Funck C, Laun FB, Wetscherek A (2018) *Characterization of the diffusion coefficient of blood*. *Magnetic Resonance in Medicine* 79(5):2752–2758. doi: 10.1002/mrm.26919
- Gamper U, Boesiger P, Kozerke S (2007) *Diffusion imaging of the in vivo heart using spin echoes--considerations on bulk motion sensitivity*. *Magnetic*

- Resonance in Medicine 57(2):331–7. doi: 10.1002/mrm.21127
- Gao JH, Miller I, Lai S, Xiong J, Fox PT (1996) *Quantitative assessment of blood inflow effects in functional MRI signals*. Magnetic Resonance in Medicine 36(2):314–319. doi: 10.1002/mrm.1910360219
- Gibson RS, Watson DD, Taylor GJ, Crosby IK, Wellons HL, Holt ND, Beller GA (1983) *Prospective assessment of regional myocardial perfusion before and after coronary revascularization surgery by Quantitative Thallium-201 scintigraphy*. Journal of the American College of Cardiology 1(3):804–815. doi: 10.1016/S0735-1097(83)80194-6
- Giese D, Haeberlin M, Barmet C, Pruessmann KP, Schaeffter T, Kozerke S (2012) *Analysis and correction of background velocity offsets in phase-contrast flow measurements using magnetic field monitoring*. Magnetic Resonance in Medicine 67(5):1294–1302. doi: 10.1002/mrm.23111
- Griswold M a., Jakob PM, Heidemann RM, Nittka M, Jellus V, Wang J, Kiefer B, Haase A (2002) *Generalized Autocalibrating Partially Parallel Acquisitions (GRAPPA)*. Magnetic Resonance in Medicine 47(6):1202–1210. doi: 10.1002/mrm.10171
- Gudbjartsson H, Patz S (1995) *The rician distribution of noisy mri data*. Magnetic Resonance in Medicine 34(6):910–914. doi: 10.1002/mrm.1910340618
- Gulani V, Calamante F, Shellock FG, Kanal E, Reeder SB (2017) *Gadolinium deposition in the brain: summary of evidence and recommendations*. The Lancet Neurology 16(7):564–570. doi: 10.1016/S1474-4422(17)30158-8
- Haacke EM, Lindskog ED, Lin W (1991) *A fast, iterative, partial-fourier technique capable of local phase recovery*. Journal of Magnetic Resonance (1969) 92(1):126–145. doi: 10.1016/0022-2364(91)90253-P
- Huang C, Graff CG, Clarkson EW, Bilgin A, Altbach MI (2012) *T2 mapping from highly undersampled data by reconstruction of principal component coefficient maps using compressed sensing*. Magnetic Resonance in Medicine 67(5):1355–1366. doi: 10.1002/mrm.23128
- Huang H-M, Shih Y-Y, Lin C (2016) *Formation of parametric images using mixed-effects models: a feasibility study*. NMR in Biomedicine 29(3):239–247. doi: 10.1002/nbm.3453
- Huizinga W, Poot DHJHJ, Guyader J-M, Klaassen R, Coolen BFF, van Kranenburg M, van Geuns RJMJM, Uitterdijk A, Polfliet M, Vandemeulebroucke J, Leemans A, Niessen WJJ, Klein S (2016) *PCA-based groupwise image registration for quantitative MRI*. Medical Image Analysis 29(January 2016):65–78. doi: 10.1016/j.media.2015.12.004

- Indermühle A, Vogel R, Meier P, Wirth S, Stoop R, Mohaupt MG, Seiler C (2006) *The relative myocardial blood volume differentiates between hypertensive heart disease and athlete's heart in humans*. *European Heart Journal* 27(13):1571–1578. doi: 10.1093/eurheartj/ehl024
- Ismail TF, Hsu L-Y, Greve AM, Gonçalves C, Jabbour A, Gulati A, Hewins B, Mistry N, Wage R, Roughton M, Ferreira PF, Gatehouse P, Firmin D, O'Hanlon R, Pennell DJ, Prasad SK, Arai AE (2014) *Coronary microvascular ischemia in hypertrophic cardiomyopathy - a pixel-wise quantitative cardiovascular magnetic resonance perfusion study*. *Journal of Cardiovascular Magnetic Resonance* 16(1):1–10. doi: 10.1186/s12968-014-0049-1
- Jauch EC, Saver JL, Adams HP, Bruno A, Connors JJB, Demaerschalk BM, Khatri P, McMullan PW, Qureshi AI, Rosenfield K, Scott PA, Summers DR, Wang DZ, Wintermark M, Yonas H (2013) *Guidelines for the early management of patients with acute ischemic stroke: A guideline for healthcare professionals from the American Heart Association/American Stroke Association*. *Stroke* 44(3):870–947. doi: 10.1161/STR.0b013e318284056a
- Jeffreys H (1946) *An invariant form for the prior probability in estimation problems*. *Proceedings of the Royal Society of London Series A, Mathematical and Physical Sciences* 186(1007):453–61. doi: 10.1098/rspa.1946.0056
- Jones DK, Horsfield MA, Simmons A (1999) *Optimal strategies for measuring diffusion in anisotropic systems by magnetic resonance imaging*. *Magnetic Resonance in Medicine* 42(3):515–525. doi: 10.1002/(SICI)1522-2594(199909)42:3<515::AID-MRM14>3.0.CO;2-Q
- Jung H, Sung K, Nayak KS, Kim EY, Ye JC (2009) *K-t FOCUSS: A general compressed sensing framework for high resolution dynamic MRI*. *Magnetic Resonance in Medicine* 61(1):103–116. doi: 10.1002/mrm.21757
- Justus CG, Hargraves WR, Mikhail A, Graber D (1978) *Methods for Estimating Wind Speed Frequency Distributions*. *Journal of Applied Meteorology* 17(3):350–353. doi: 10.1175/1520-0450(1978)017<0350:MFEWSF>2.0.CO;2
- Kaneko N, Matsuda R, Toda M, Shimamoto K (2011) *Three-dimensional reconstruction of the human capillary network and the intramyocardial micronecrosis*. *American Journal of Physiology Heart and Circulatory Physiology* 300(3):H754–H761. doi: 10.1152/ajpheart.00486.2010

- Karampinos DC, King KF, Sutton BP, Georgiadis JG (2010) *Intravoxel partially coherent motion technique: Characterization of the anisotropy of skeletal muscle microvasculature*. Journal of Magnetic Resonance Imaging 31(4):942–953. doi: 10.1002/jmri.22100
- Kassab GS, Fung YC (1994) *Topology and dimensions of pig coronary capillary network*. The American Journal of Physiology 267(1 Pt 2):H319-25. doi: 10.1152/ajpheart.1994.267.1.H319
- Kiselev VG (2017) *Fundamentals of diffusion MRI physics*. NMR in Biomedicine 30(3):e3602. doi: 10.1002/nbm.3602
- Knobloch V, Binter C, Kurtcuoglu V, Kozerke S (2014) *Arterial, venous, and cerebrospinal fluid flow: simultaneous assessment with Bayesian multipoint velocity-encoded MR imaging*. Radiology 270(2):566–73. doi: 10.1148/radiol.13130840
- Knoll F, Raya JG, Halloran RO, Baete S, Sigmund E, Bammer R, Block T, Otazo R, Sodickson DK (2015) *A model-based reconstruction for undersampled radial spin-echo DTI with variational penalties on the diffusion tensor*. NMR in Biomedicine 28(3):353–366. doi: 10.1002/nbm.3258
- Laissy J-P, Gaxotte V, Ironde-laissy E, Klein I, Ribet A, Bendriss A, Chillon S, Schouman-Claeys E, Steg PG, Serfaty J-M (2013) *Cardiac diffusion-weighted MR imaging in recent, subacute, and chronic myocardial infarction: a pilot study*. Journal of Magnetic Resonance Imaging 38(6):1377–1387. doi: 10.1002/jmri.24125
- Le Bihan D (1988) *Intravoxel incoherent motion imaging using steady-state free precession*. Magnetic Resonance in Medicine 7(3):346–51. doi: 10.1002/mrm.1910070312
- Le Bihan D (2008) *Intravoxel incoherent motion perfusion MR imaging: a wake-up call*. Radiology 249(3):748–752. doi: 10.1148/radiol.2493081301
- Le Bihan D, Breton E (1985) *Imagerie de diffusion in-vivo par résonance magnétique nucléaire*. Comptes-Rendus de l'Académie Des Sciences 93(5):27–34
- Le Bihan D, Breton E, Lallemand D, Aubin ML, Vignaud J, Laval-Jeantet M (1988) *Separation of diffusion and perfusion in intravoxel incoherent motion MR imaging*. Radiology 168(2):497–505. doi: 10.1148/radiology.168.2.3393671
- Le Bihan D, Breton E, Lallemand D, Grenier P, Cabanis E, Laval-Jeantet M (1986) *MR imaging of intravoxel incoherent motions: application to diffusion and perfusion in neurologic disorders*. Radiology 161(2):401–407. doi: 129

10.1148/radiology.161.2.3763909

- Le Bihan D, Turner R (1992) *The capillary network: a link between IVIM and classical perfusion*. *Magnetic Resonance in Medicine* 27(1):171–178. doi: 10.1002/mrm.1910270116
- Lemke A, Laun FB, Klau M, Re TJ, Simon D, Delorme S, Schad LR, Stieltjes B (2009) *Differentiation of Pancreas Carcinoma From Healthy Pancreatic Tissue Using Multiple b-Values*. *Investigative Radiology* 44(12):769–775. doi: 10.1097/RLI.0b013e3181b62271
- Lemke A, Laun FB, Simon D, Stieltjes B, Schad LR (2010) *An in vivo verification of the intravoxel incoherent motion effect in diffusion-weighted imaging of the abdomen*. *Magnetic Resonance in Medicine* 64(6):1580–1585. doi: 10.1002/mrm.22565
- Lemke A, Stieltjes B, Schad LR, Laun FB (2011) *Toward an optimal distribution of b values for intravoxel incoherent motion imaging*. *Magnetic Resonance Imaging* 29(6):766–776. doi: 10.1016/j.mri.2011.03.004
- Liang Z (2007) *Spatiotemporal imaging with partially separable functions*. 4th IEEE International Symposium on Biomedical Imaging: From Nano to Macro 988–991. doi: 10.1109/ISBI.2007.357020
- Luciani A, Vignaud A, Cavet M, Nhieu JT Van, Mallat A, Ruel L, Laurent A, Deux J-F, Brugieres P, Rahmouni A, Tran Van Nhieu J, Mallat A, Ruel L, Laurent A, Deux J-F, Brugieres P, Rahmouni A (2008) *Liver cirrhosis: intravoxel incoherent motion MR imaging—pilot study*. *Radiology* 249(3):891–899. doi: 10.1148/radiol.2493080080
- Lunn D, Spiegelhalter D, Thomas A, Best N (2009) *The BUGS project: Evolution, critique and future directions*. *Statistics in Medicine* 28(25):3049–3067. doi: 10.1002/sim.3680
- Lunn DJ, Thomas A, Best N, Spiegelhalter D (2000) *WinBUGS - A Bayesian modelling framework: Concepts, structure, and extensibility*. *Statistics and Computing* 10(4):325–337. doi: 10.1023/A:1008929526011
- Lustig M, Donoho D, Pauly JM (2007) *Sparse MRI: The application of compressed sensing for rapid MR imaging*. *Magnetic Resonance in Medicine* 58(6):1182–95. doi: 10.1002/mrm.21391
- Lustig M, Donoho DL, Santos JM, Pauly JM (2008) *Compressed Sensing MRI*. *IEEE Signal Processing Magazine* 25(2):72–82. doi: 10.1109/MSP.2007.914728
- Lustig M, Pauly JM (2010) *SPIRiT: Iterative self-consistent parallel imaging*

- reconstruction from arbitrary k-space*. *Magnetic Resonance in Medicine* 64(2):457–71. doi: 10.1002/mrm.22428
- Lustig M, Santos JM, Donoho D, Pauly JM (2006) *k-t SPARSE: high frame rate dynamic MRI exploiting spatio-temporal sparsity*. In: *Proc. Intl. Soc. Mag. Reson. Med.* p 2420
- Madore B, Glover GH, Pelc NJ (1999) *Unaliasing by fourier-encoding the overlaps using the temporal dimension (UNFOLD), applied to cardiac imaging and fMRI*. *Magnetic Resonance in Medicine* 42(5):813–28. doi: 10.1002/(SICI)1522-2594(199911)42:5<813::AID-MRM1>3.0.CO;2-S
- Manka R, Paetsch I, Kozerke S, Moccetti M, Hoffmann R, Schroeder J, Reith S, Schnackenburg B, Gaemperli O, Wissmann L, Wyss CA, Kaufmann PA, Corti R, Boesiger P, Marx N, Lüscher TF, Jahnke C (2012) *Whole-heart dynamic three-dimensional magnetic resonance perfusion imaging for the detection of coronary artery disease defined by fractional flow reserve: Determination of volumetric myocardial ischaemic burden and coronary lesion location*. *European Heart Journal* 33(16):2016–2024. doi: 10.1093/eurheartj/ehs170
- Mathieu O, Cruz-Orive L -M, Hoppeler H, Weibel ER (1983) *Estimating length density and quantifying anisotropy in skeletal muscle capillaries*. *Journal of Microscopy* 131(2):131–146. doi: 10.1111/j.1365-2818.1983.tb04240.x
- Mekkaoui C, Reese TG, Jackowski MP, Bhat H, Sosnovik DE (2017) *Diffusion MRI in the heart*. *NMR in Biomedicine* 30(3):e3426. doi: 10.1002/nbm.3426
- Mendis S, Puska P, Norrving B (2011) *Global Atlas on Cardiovascular disease prevention and control*
- Messroghli DR, Plein S, Higgins DM, Walters K, Jones TR, Ridgway JP, Sivananthan MU (2006) *Human myocardium: single-breath-hold MR T1 mapping with high spatial resolution--reproducibility study*. *Radiology* 238(3):1004–1012. doi: 10.1148/radiol.2382041903
- Meyer CH, Pauly JM, Macovski A, Nishimura DG (1990) *Simultaneous spatial and spectral selective excitation*. *Magnetic Resonance in Medicine* 15(2):287–304. doi: 10.1002/mrm.1910150211
- Moran PR (1982) *A flow velocity zeugmatographic interlace for NMR imaging in humans*. *Magnetic Resonance Imaging* 1(4):197–203. doi: 10.1016/0730-725X(82)90170-9
- Mou A, Zhang C, Li M, Jin F, Song Q, Liu A, Li Z (2017) *Evaluation of myocardial microcirculation using intravoxel incoherent motion imaging*. *Journal of*

- Magnetic Resonance Imaging 46(6):1818–1828. doi: 10.1002/jmri.25706
- Moulin K, Aliotta E, Ennis DB (2019) *Effect of flow-encoding strength on intravoxel incoherent motion in the liver*. Magnetic Resonance in Medicine 81(3):1521–1533. doi: 10.1002/mrm.27490
- Moulin KK, Croisille P, Feiweier T, Delattre BMA a, Wei H, Robert B, Beuf O, Viallon M (2016) *In vivo free-breathing DTI and IVIM of the whole human heart using a real-time slice-followed SE-EPI navigator-based sequence: A reproducibility study in healthy volunteers*. Magnetic Resonance in Medicine 76(1):70–82. doi: 10.1002/mrm.25852
- Mozumder M, Beltrachini L, Collier Q, Pozo JM, Frangi AF (2018) *Simultaneous magnetic resonance diffusion and pseudo-diffusion tensor imaging*. Magnetic Resonance in Medicine 79(4):2367–2378. doi: 10.1002/mrm.26840
- Murphy KP (2007) *Conjugate Bayesian analysis of the Gaussian distribution*. <https://www.cs.ubc.ca/~murphyk/Papers/bayesGauss.pdf>
- Nguyen C, Fan Z, Sharif B, He Y, Dharmakumar R, Berman DS, Li D (2014) *In vivo three-dimensional high resolution cardiac diffusion-weighted MRI: a motion compensated diffusion-prepared balanced steady-state free precession approach*. Magnetic Resonance in Medicine 72(5):1257–1267. doi: 10.1002/mrm.25038
- Niellas-Vallespin S, Khalique Z, Ferreira PF, de Silva R, Scott AD, Kilner P, McGill LA, Giannakidis A, Gatehouse PD, Ennis D, Aliotta E, Al-Khalil M, Kellman P, Mazilu D, Balaban RS, Firmin DN, Arai AE, Pennell DJ (2017) *Assessment of Myocardial Microstructural Dynamics by In Vivo Diffusion Tensor Cardiac Magnetic Resonance*. Journal of the American College of Cardiology 69(6):661–676. doi: 10.1016/j.jacc.2016.11.051
- Noll DC, Nishimura DG, Macovski A (1991) *Homodyne Detection in Magnetic Resonance Imaging*. IEEE Transactions on Medical Imaging 10(2):154–163. doi: 10.1109/42.79473
- Nordmeyer-Massner J a., De Zanche N, Pruessmann KP (2009) *Mechanically adjustable coil array for wrist MRI*. Magnetic Resonance in Medicine 61(2):429–438. doi: 10.1002/mrm.21868
- Notohamiprodjo M, Chandarana H, Mikheev A, Rusinek H, Grinstead J, Feiweier T, Raya JG, Lee VS, Sigmund EE (2015) *Combined intravoxel incoherent motion and diffusion tensor imaging of renal diffusion and flow anisotropy*. Magnetic Resonance in Medicine 73(4):1526–1532. doi: 10.1002/mrm.25245

- Ohliger MA, Grant AK, Sodickson DK (2003) *Ultimate Intrinsic Signal-to-Noise Ratio for Parallel MRI: Electromagnetic Field Considerations*. *Magnetic Resonance in Medicine* 50(5):1018–1030. doi: 10.1002/mrm.10597
- Orton MR, Collins DJ, Koh D-M, Leach MO (2014) *Improved intravoxel incoherent motion analysis of diffusion weighted imaging by data driven Bayesian modeling*. *Magnetic Resonance in Medicine* 71:411–420. doi: 10.1002/mrm.24649
- Pai VM, Rapacchi S, Kellman P, Croisille P, Wen H (2011) *PCATMIP: Enhancing signal intensity in diffusion-weighted magnetic resonance imaging*. *Magnetic Resonance in Medicine* 65(6):1611–1619. doi: 10.1002/mrm.22748
- Patel J, Sigmund EE, Rusinek H, Oei M, Babb JS, Taouli B (2010) *Diagnosis of cirrhosis with intravoxel incoherent motion diffusion MRI and dynamic contrast-enhanced MRI alone and in combination: preliminary experience*. *Journal of Magnetic Resonance Imaging* 31(3):589–600. doi: 10.1002/jmri.22081
- Pedersen H, Kozerke S, Ringgaard S, Nehrke K, Won YK (2009) *K-t PCA: Temporally constrained k-t BLAST reconstruction using principal component analysis*. *Magnetic Resonance in Medicine* 62(3):706–716. doi: 10.1002/mrm.22052
- Petzschner FH, Ponce IP, Blaimer M, Jakob PM, Breuer F a (2011) *Fast MR parameter mapping using k-t principal component analysis*. *Magnetic Resonance in Medicine* 66(3):706–16. doi: 10.1002/mrm.22826
- Plummer M (2003) *JAGS: A Program for Analysis of Bayesian Graphical Models using Gibbs Sampling*. In: 3rd International Workshop on Distributed Statistical Computing (DSC 2003); Vienna, Austria
- Poole DC, Mathieu-Costello O (1990) *Analysis of capillary geometry in rat subepicardium and subendocardium*. *American Journal of Physiology - Heart and Circulatory Physiology* 259(1):H204–H210. doi: 10.1152/ajpheart.1990.259.1.H204
- Pruessmann KP, Weiger M, Börnert P, Boesiger P (2001) *Advances in sensitivity encoding with arbitrary k-space trajectories*. *Magnetic Resonance in Medicine* 46:638–651. doi: 10.1002/mrm.1241
- Pruessmann KP, Weiger M, Scheidegger MB, Boesiger P (1999) *SENSE: sensitivity encoding for fast MRI*. *Magnetic Resonance in Medicine* 42(5):952–62. doi: 10.1002/(SICI)1522-2594(199911)42:5<952::AID-MRM16>3.0.CO;2-S

- Puig J, Sánchez-González J, Blasco G, Daunis-I-Estadella P, Federau C, Alberich-Bayarri Á, Biarnes C, Nael K, Essig M, Jain R, Wintermark M, Pedraza S (2016) *Intravoxel Incoherent Motion Metrics as Potential Biomarkers for Survival in Glioblastoma*. *PLoS One* 11(7):e0158887. doi: 10.1371/journal.pone.0158887
- Purvis NL, Gibbs P, Pickles MD, Turnbull LW (2015) *Optimisation of b-value Distribution for Intravoxel Incoherent Motion (IVIM) Imaging of Breast Cancer with Clinical Results*. In: *Proc. Intl. Soc. Mag. Reson. Med.* p 1089
- Rapacchi S, Wen H, Viallon M, Grenier D, Kellman P, Croisille P, Pai VM (2011) *Low b-value diffusion-weighted cardiac magnetic resonance imaging: initial results in humans using an optimal time-window imaging approach*. *Investigative Radiology* 46(12):751–758. doi: 10.1097/RLI.0b013e31822438e8
- Rheinheimer S, Stieltjes B, Schneider F, Simon D, Pahernik S, Kauczor HU, Hallscheidt P (2012) *Investigation of renal lesions by diffusion-weighted magnetic resonance imaging applying intravoxel incoherent motion-derived parameters--initial experience*. *European Journal of Radiology* 81(3):e310-6. doi: 10.1016/j.ejrad.2011.10.016
- Roemer PB, Edelstein WA, Hayes CE, Souza SP, Mueller OM (1990) *The NMR phased array*. *Magnetic Resonance in Medicine* 16(2):192–225. doi: 10.1002/mrm.1910160203
- Rose JN, Nielles-Vallespin S, Ferreira PF, Firmin DN, Scott AD, Doorly DJ (2019) *Novel insights into in-vivo diffusion tensor cardiovascular magnetic resonance using computational modeling and a histology-based virtual microstructure*. *Magnetic Resonance in Medicine* 81(4):2759–2773. doi: 10.1002/mrm.27561
- Ross R (1986) *The pathogenesis of atherosclerosis--an update*. *The New England Journal of Medicine* 314(8):488–500. doi: 10.1056/NEJM198602203140806
- Santelli C, Loecher M, Busch J, Wieben O, Schaeffter T, Kozerke S (2016) *Accelerating 4D flow MRI by exploiting vector field divergence regularization*. *Magnetic Resonance in Medicine* 75(1):115–125. doi: 10.1002/mrm.25563
- Schick F (1997) *SPLICE: Sub-second diffusion-sensitive MR imaging using a modified fast spin-echo acquisition mode*. *Magnetic Resonance in Medicine* 38(4):638–644. doi: 10.1002/mrm.1910380418
- Schieda N, Blachman JI, Costa AF, Glikstein R, Hurrell C, James M, Jabejdar

- Maralani P, Shabana W, Tang A, Tsampalieros A, van der Pol C, Hiremath S (2018) *Gadolinium-Based Contrast Agents in Kidney Disease: Comprehensive Review and Clinical Practice Guideline Issued by the Canadian Association of Radiologists*. Canadian Association of Radiologists Journal 69(2):136–150. doi: 10.1016/j.carj.2017.11.002
- Schmidt JFM, Wissmann L, Manka R, Kozerke S (2014) *Iterative k-t principal component analysis with nonrigid motion correction for dynamic three-dimensional cardiac perfusion imaging*. Magnetic Resonance in Medicine 72(1):68–79. doi: 10.1002/mrm.24894
- Scott AD, Nielles-Vallespin S, Ferreira PF, Khalique Z, Gatehouse PD, Kilner P, Pennell DJ, Firmin DN (2018) *An in-vivo comparison of stimulated-echo and motion compensated spin-echo sequences for 3 T diffusion tensor cardiovascular magnetic resonance at multiple cardiac phases*. Journal of Cardiovascular Magnetic Resonance 20(1):1–15. doi: 10.1186/s12968-017-0425-8
- Scott AD, Nielles-Vallespin S, Ferreira PF, McGill L-A, Pennell DJ, Firmin DN (2016) *The effects of noise in cardiac diffusion tensor imaging and the benefits of averaging complex data*. NMR in Biomedicine 29(5):588–599. doi: 10.1002/nbm.3500
- Sodickson DK, Manning WJ (1997) *Simultaneous acquisition of spatial harmonics (SMASH): Fast imaging with radiofrequency coil arrays*. Magnetic Resonance in Medicine 38(4):591–603. doi: 10.1002/mrm.1910380414
- Sourbron SP, Buckley DL (2012) *Tracer kinetic modelling in MRI: Estimating perfusion and capillary permeability*. Physics in Medicine and Biology 57(2):0–33. doi: 10.1088/0031-9155/57/2/R1
- Spinner GR, Schmidt JFM, von Deuster C, Federau C, Stoeck CT, Kozerke S (2018) *Enhancing intravoxel incoherent motion parameter mapping in the brain using k-b PCA*. NMR in Biomedicine 31(12):e4008. doi: 10.1002/nbm.4008
- Spinner GR, von Deuster C, Tezcan KC, Stoeck CT, Kozerke S (2017) *Bayesian intravoxel incoherent motion parameter mapping in the human heart*. Journal of Cardiovascular Magnetic Resonance 19(1):85. doi: 10.1186/s12968-017-0391-1
- Stejskal EO, Tanner JE (1965) *Spin Diffusion Measurements: Spin Echoes in the Presence of a Time-Dependent Field Gradient*. The Journal of Chemical Physics 42(1):288–292. doi: 10.1063/1.1695690

- Stoeck CT, Kalinowska A, von Deuster C, Harmer J, Chan RW, Niemann M, Manka R, Atkinson D, Sosnovik DE, Mekkaoui C, Kozerke S (2014) *Dual-phase cardiac diffusion tensor imaging with strain correction*. PLoS One 9(9):e107159. doi: 10.1371/journal.pone.0107159
- Stoeck CT, von Deuster C, Genet M, Atkinson D, Kozerke S (2016) *Second-order motion-compensated spin echo diffusion tensor imaging of the human heart*. Magnetic Resonance in Medicine 75(4):1669–1676. doi: 10.1002/mrm.25784
- Stoeck CT, von Deuster C, van Gorkum R, Kozerke S (2017) *Impact of eddy-currents and cardiac motion in DTI of the in-vivo heart - a comparison of second-order motion compensated SE versus STEAM*. In: Proc. Intl. Soc. Mag. Reson. Med.
- Stoneking CJ (2014) *Bayesian inference of Gaussian mixture models with noninformative priors*. arxiv.org/abs/14054895
- Tibshirani R (1996) *Regression Shrinkage and Selection via the Lasso*. Journal of the Royal Statistical Society Series B (Methodological) 58(1):267–288. doi: 10.1111/j.2517-6161.1996.tb02080.x
- Torrey HC (1956) *Bloch Equations with Diffusion Terms*. Physical Review 104(3):563–565. doi: 10.1103/PhysRev.104.563
- Tsao J, Boesiger P, Pruessmann KP (2003) *k-t BLAST and k-t SENSE: dynamic MRI with high frame rate exploiting spatiotemporal correlations*. Magnetic Resonance in Medicine 50(5):1031–42. doi: 10.1002/mrm.10611
- Tuch DS (2004) *Q-ball imaging*. Magnetic Resonance in Medicine 52(6):1358–72. doi: 10.1002/mrm.20279
- Tuch DS, Reese TG, Wiegell MR, Makris N, Belliveau JW, Van Wedeen J (2002) *High angular resolution diffusion imaging reveals intravoxel white matter fiber heterogeneity*. Magnetic Resonance in Medicine 48(4):577–582. doi: 10.1002/mrm.10268
- Uecker M, Lai P, Murphy MJ, Virtue P, Elad M, Pauly JM, Vasanawala SS, Lustig M (2014) *ESPIRiT - An eigenvalue approach to autocalibrating parallel MRI: Where SENSE meets GRAPPA*. Magnetic Resonance in Medicine 71:990–1001. doi: 10.1002/mrm.24751
- van der Vaart AW (1998) *Asymptotic Statistics*. Cambridge University Press, Cambridge
- Vishnevskiy V, Gass T, Szekely G, Tanner C, Goksel O (2017) *Isotropic Total Variation Regularization of Displacements in Parametric Image*

- Registration*. IEEE Transactions on Medical Imaging 36(2):385–395. doi: 10.1109/TMI.2016.2610583
- von Deuster C, Sammut E, Asner L, Nordsletten D, Lamata P, Stoeck CT, Kozerke S, Razavi R (2016a) *Studying Dynamic Myofiber Aggregate Reorientation in Dilated Cardiomyopathy Using In Vivo Magnetic Resonance Diffusion Tensor Imaging*. Circulation Cardiovascular Imaging 9(10):1–10. doi: 10.1161/CIRCIMAGING.116.005018
- von Deuster C, Stoeck CT, Genet M, Atkinson D, Kozerke S (2016b) *Spin echo versus stimulated echo diffusion tensor imaging of the in vivo human heart*. Magnetic Resonance in Medicine 76(3):862–72. doi: 10.1002/mrm.25998
- von Deuster C, Stoeck CT, Wissmann L, Spinner G, Fleischmann T, Emmert MY, Cesarovic N, Kozerke S (2015) *Verification of the intra-voxel incoherent motion (IVIM) model in the porcine heart*. In: Proc. Intl. Soc. Mag. Reson. Med. p 2612
- Warach S, Gaa J, Siewert B, Wielopolski P, Edelman RR (1995) *Acute human stroke studied by whole brain echo planar diffusion-weighted magnetic resonance imaging*. Annals of Neurology 37(2):231–41. doi: 10.1002/ana.410370214
- Wedeen VJ, Hagmann P, Tseng WJ, Reese TG, Weisskoff RM (2005) *Mapping complex tissue architecture with diffusion spectrum magnetic resonance imaging*. Magnetic Resonance in Medicine 54(6):1377–86. doi: 10.1002/mrm.20642
- Welsh CL, DiBella EVR, Adluru G, Hsu EW (2013) *Model-based reconstruction of undersampled diffusion tensor k-space data*. Magnetic Resonance in Medicine 70(2):429–440. doi: 10.1002/mrm.24486
- Welsh CL, DiBella EVR, Hsu EW (2015) *Higher-order motion-compensation for in vivo cardiac diffusion tensor imaging in rats*. IEEE Transactions on Medical Imaging 34(9):1843–1853. doi: 10.1109/TMI.2015.2411571
- Wetscherek A, Stieltjes B, Laun FB (2015) *Flow-compensated intravoxel incoherent motion diffusion imaging*. Magnetic Resonance in Medicine 74(2):410–419. doi: 10.1002/mrm.25410
- While PT (2017) *A comparative simulation study of bayesian fitting approaches to intravoxel incoherent motion modeling in diffusion-weighted MRI*. Magnetic Resonance in Medicine 78(6):2373–2387. doi: 10.1002/mrm.26598
- Wiesinger F, Boesiger P, Pruessmann KP (2004) *Electrodynamics and ultimate*

- SNR in parallel MR imaging*. *Magnetic Resonance in Medicine* 52(2):376–390. doi: 10.1002/mrm.20183
- Wilke N, Jerosch-Herold M, Wang Y, Huang Y, Christensen B V, Stillman AE, Ugurbil K, McDonald K, Wilson RF (1997) *Myocardial perfusion reserve: assessment with multisection, quantitative, first-pass MR imaging*. *Radiology* 204(2):373–84. doi: 10.1148/radiology.204.2.9240523
- Wissmann L, Niemann M, Gotschy A, Manka R, Kozerke S (2015) *Quantitative three-dimensional myocardial perfusion cardiovascular magnetic resonance with accurate two-dimensional arterial input function assessment*. *Journal of Cardiovascular Magnetic Resonance* 17(1):108–119. doi: 10.1186/s12968-015-0212-3
- Wu W-C, Chen Y-F, Tseng H-M, Yang S-C, My P-C (2015) *Caveat of measuring perfusion indexes using intravoxel incoherent motion magnetic resonance imaging in the human brain*. *European Radiology* 25(8):2485–2492. doi: 10.1007/s00330-015-3655-x
- Wurnig MC, Donati OF, Ulbrich E, Filli L, Kenkel D, Thoeny HC, Boss A (2015) *Systematic analysis of the intravoxel incoherent motion threshold separating perfusion and diffusion effects: Proposal of a standardized algorithm*. *Magnetic Resonance in Medicine* 74(5):1414–22. doi: 10.1002/mrm.25506
- Yamada I, Aung W, Himeno Y, Nakagawa T, Shibuya H (1999) *Diffusion coefficients in abdominal organs and hepatic lesions: evaluation with intravoxel incoherent motion echo-planar MR imaging*. *Radiology* 210(3):617–623. doi: 10.1148/radiology.210.3.r99fe17617
- Zhang T, Pauly JM, Levesque IR (2015) *Accelerating parameter mapping with a locally low rank constraint*. *Magnetic Resonance in Medicine* 73(2):655–661. doi: 10.1002/mrm.25161
- Zhao B, Lu W, Hitchens TK, Lam F, Ho C, Liang ZP (2015) *Accelerated MR parameter mapping with low-rank and sparsity constraints*. *Magnetic Resonance in Medicine* 74(2):489–498. doi: 10.1002/mrm.25421
- Zhao F, Noll DC, Nielsen JF, Fessler J a. (2012) *Separate magnitude and phase regularization via compressed sensing*. *IEEE Transactions on Medical Imaging* 31:1713–1723. doi: 10.1109/TMI.2012.2196707
- Zhu Y, Wu Y, Zheng Y, Wu EX, Ying L, Liang D (2012) *A model-based method with joint sparsity constraint for direct diffusion tensor estimation*. In: *Proceedings - International Symposium on Biomedical Imaging*. pp 510–513

List of publications

- 2019** **Spinner GR**, Stoeck CT, Mathez L, von Deuster C, Federau C, Kozerke S. *On Probing Intravoxel Incoherent Motion in the Heart - Spin Echo versus Stimulated Echo Diffusion Weighted Imaging*. *Magnetic Resonance in Medicine* (early view). doi: 10.1002/mrm.27777
- 2018** Wyss M, Manoliu A, Marcon M, **Spinner G**, Lüchinger R, Prüssmann KP, Andreisek G. *Clinical Magnetic Resonance Imaging of the Knee at 7.0 Tesla: Optimization of Fat Suppression*. *Investigative Radiology* 54(3):160-168. doi: 10.1097/RLI.0000000000000523
- 2018** **Spinner GR**, Schmidt JFM, von Deuster C, Federau C, Stoeck CT, Kozerke S. *Enhancing Intravoxel Incoherent Motion Parameter Mapping in the Brain Using k-b PCA*. *NMR in Biomedicine* 31(12):e4008. doi: 10.1002/nbm.4008
- 2017** **Spinner GR**, von Deuster C, Tezcan KC, Stoeck CT, Kozerke S. *Bayesian intravoxel incoherent motion parameter mapping in the human heart*. *Journal of Cardiovascular Magnetic Resonance* 19(1):85. doi: 10.1186/s12968-017-0391-1
- 2016** Kuhn FP, **Spinner G**, Del Grande F, Wyss M, Piccirelli M, Erni S, Pfister P, Ho M, BR Sah, Filli L, Ettl DA, Gallo LM, Andreisek G, Manoliu A. *MR imaging of the temporomandibular joint: comparison between acquisitions at 7.0 T using dielectric pads and 3.0 T*. *Dentomaxillofacial Radiology* 46(1):20160280. doi: 10.1259/dmfr.20160280
- 2016** Manoliu A, **Spinner G**, Wyss M, Filli L, Erni S, Ettl DA, Ukbrich EJ, Kuhn FP, Gallo LM, Andreisek G. *Comparison of a 32-channel head coil and a 2-channel surface coil for MR imaging of the temporomandibular joint at 3.0 T*. *Dentomaxillofacial Radiology* 45(4):20150420. doi: 10.1259/dmfr.20150420
- 2015** Manoliu A, **Spinner G**, Wyss M, Ettl DA, Nanz D, Kuhn FP, Gallo LM, Andreisek G. *Magnetic resonance imaging of the temporomandibular joint at 7.0 T using high-permittivity dielectric pads: a feasibility study*. *Investigative Radiology* 50(12):843-849. doi: 10.1097/RLI.0000000000000196
- 2015** Manoliu A, **Spinner G**, Wyss M, Erni S, Ettl DA, Nanz D, Ukbrich EJ, Gallo LM, Andreisek G. *Quantitative and qualitative*

comparison of MR imaging of the temporomandibular joint at 1.5 and 3.0 T using an optimized high-resolution protocol. Dentomaxillofacial Radiology 45(1):20150240. doi: 10.1259/dmfr.20150240

- 2014** Hangauer A, **Spinner G**, Nikodem M, Wysocki G. *High frequency modulation capabilities and quasi single-sideband emission from a quantum cascade laser.* Optics express 22(19):23439-23455. doi: 10.1364/OE.22.023439
- 2013** Hangauer A, **Spinner G**, Nikodem M, Wysocki G. *Chirped laser dispersion spectroscopy using a directly modulated quantum cascade laser.* Applied Physics Letters 103(19):191107-1-191107-4. doi: 10.1063/1.4829036

Conference abstracts and proceedings

- 2019** **Spinner GR**, Stoeck CT, Mathez L, von Deuster C, Federau C, Kozerke S. *On Probing Intravoxel Incoherent Motion in the Heart using Spin Echo versus Stimulated Echo Diffusion Weighted Imaging*. Proceedings of the 28th Meeting of ISMRM, Montreal, Canada.
- 2019** Phi van V, Schmidt F, Mathez L, **Spinner G**, Kozerke S, Federau C. *Simulation of Intravoxel Incoherent Perfusion Signal using a Realistic Capillary Network of a Mouse Brain*. Proceedings of the 28th Meeting of ISMRM, Montreal, Canada.
- 2018** **Spinner G**, Schmidt J, Kozerke S. *Accelerating Intravoxel Incoherent Motion Mapping in the Brain using k-bpp PCA*. Proceedings of the 27th Meeting of ISMRM, Paris, France.
- 2017** von Deuster C, **Spinner G**, van Gorkum Robbert, Stoeck C, Kozerke S. *Free-Breathing Black-Blood Prepared Cardiac Diffusion Tensor Imaging*. Proceedings of the 26th Meeting of ISMRM, Honolulu, USA
- 2017** **Spinner G**, von Deuster C, Oebel S, Stoeck C, Manka R, Kozerke S. *Intravoxel Incoherent Motion Model in the Heart of Patients Under Adenosine Induced Stress*. Proceedings of the 26th Meeting of ISMRM, Honolulu, USA
- 2017** Vishnevskiy V, **Spinner G**, Stoeck C, von Deuster C, Kozerke S. *Non-Rigid Groupwise Registration for Intravoxel Incoherent Motion Imaging of the Heart*. Proceedings of the 26th Meeting of ISMRM, Honolulu, USA
- 2017** **Spinner G**, von Deuster C, Stoeck C, Kozerke S. *Validation of the Intravoxel Incoherent Motion Model in the Healthy Human Heart using Black-Blood Preparation*. Proceedings of the 26th Meeting of ISMRM, Honolulu, USA
- 2016** **Spinner G**, Schmidt J, Kozerke S. *Accelerating Intravoxel Incoherent Motion Imaging of the Brain Using k-PCA*. Proceedings of the 25th Meeting of ISMRM, Singapore

- 2016 **Spinner G**, von Deuster C, Stoeck C, Kozerke S. *Bayesian Intravoxel Incoherent Motion Imaging to Map Perfusion in the Human Heart*. Proceedings of the 25th Meeting of ISMRM, Singapore
- 2016 Wyss M, Manoliu A, **Spinner G**, Marcon M, Luchinger R, Nanz D, Pruessmann K, Andreisek G. *Evaluation of Different Fat Suppression Techniques for Clinical Knee MRI at 7.0 Tesla*. Proceedings of the 25th Meeting of ISMRM, Singapore
- 2016 **Spinner G**, von Deuster C, Stoeck CT, Kozerke S. *Bayesian Intravoxel Incoherent motion Parameter Mapping in the Human Heart*. Proceedings of the 33rd Meeting of ESMRMB, Vienna, Austria
- 2015 Manoliu A, **Spinner G**, Wyss M, Nanz D, Ettl DA, Gallo LM, Andreisek G. *MR Imaging of the Temporomandibular Joint at 7.0 Tesla: A Feasibility Study Using Novel High Permittivity Dielectric Pads*. Proceedings of the 23rd Meeting of ISMRM, Toronto, Canada
- 2015 von Deuster C, Stoeck CT, Wissmann L, **Spinner G**, Fleischmann T, Emmert M, Cesarovic N, Kozerke S. *Verification of the Intra-Voxel Incoherent Motion (IVIM) Model in the Porcine Heart*. Proceedings of the 23rd Meeting of ISMRM, Toronto, Canada
- 2015 **Spinner G**, Schmidt JFM, Kozerke S. *Accelerating Intravoxel Incoherent Motion MRI using k-b PCA*. Proceedings of the 32nd Meeting of ESMRMB, Edinburgh, UK
- 2015 Manoliu A, **Spinner G**, Wyss M, Erni S, Ettl D, Nanz D, Ulbrich EJ, Gallo LM, Andreisek G. *MR imaging of the temporomandibular joint at 7.0 Tesla: A feasibility study using novel high permittivity dielectric pads*. Swiss Congress of Radiology, Basel, Switzerland
- 2013 Hangauer A, **Spinner G**, Nikodem M, Wysocki G. *Direct modulation of quantum cascade lasers for chirped laser dispersion spectroscopy*. Proceedings of Mid-Infrared Coherent Sources, OSA conference. Paris, France
- 2013 Hangauer A, **Spinner G**, Nikodem M, Wysocki G. *High-speed modulation characteristic of a quantum cascade laser*. Proceedings of Lasers and Electro-Optics (CLEO), IEEE conference. San Jose, USA

Acknowledgements

First, I would like to thank Prof. Sebastian Kozerke for kindly giving me the opportunity to pursue my research in his group. He made this thesis possible by providing generous funding and outstanding infrastructure. Moreover, he provided constant guidance and exceptional expertise. In addition, he was very approachable and invested a generous amount of his time in advising my work.

I would also like to thank Prof. Gustav Strijkers for the co-examination of my thesis.

This thesis would also not be possible without the great support from my fellow colleagues. I am especially grateful for the help from the diffusion experts Constantin von Deuster and Christian Stoeck. The former helped me greatly as early as from applying for the position. He then kindly helped me a lot in learning about diffusion imaging, getting familiar with the scanners and PhD-life in general. He was very patient in helping me scanning during countless hours in the MRI basement of the hospital, passing down his knowledge in a very patient and friendly way. Besides that, he was a great, kind and fun roommate during conferences or elsewhere. Christian pioneered cardiac diffusion imaging and hence made my work possible. His pulse programming and general MRI knowledge was of great help to me. Moreover, his almost infinite endurance was greatly appreciated during several all-night scan sessions. In addition, he is a great gym companion, who even provides great advice during some serious bench pressing.

I am especially thankful for all the help I received from the “old guards” during my early PhD years: Verena Knobloch, Christian Binter, Claudio Santelli and Johannes Schmidt. The first two helped me quite a bit with early flow experiments and with getting started in general. Claudio told me about image reconstruction and provided very useful scripts and templates. Johannes taught me (almost) everything there is to know about image reconstruction within an afternoon. I am especially grateful for his code legacy, which was of great use for me and facilitated my work greatly. Besides that, he was always up for a small beer after work. He was happy to share his k-t reconstruction and other knowledge in even some unusual surroundings. Another special thanks goes out to Andrei Manoliu and his clinical input. A fruitful working cooperation ensued. In addition, his unique approach was entertaining and great fun. All the advice and knowledge from the former Gastro MR group, namely Dian Liu and Vlad Ceregan were greatly appreciated.

The help I received from Gyrotools was of great benefit for me. Besides their great software tools and pulse-programming course, their personal support was very valuable. Gérard Crelier helped me with switching from one software release to the other back and forth. Martin Bühner helped me with pulse programming, image reconstruction and MRI technicalities in general. Daniel Giese provided me with some great patch features during my early years.

The medical expertise from Alexander Gotschy, Mareike Gastl and Sabrina Oebel is greatly appreciated. The latter kindly enabled and supervised patient data acquisition for me.

Besides the ones already mentioned, I would like to thank my “scan buddies” who helped me acquiring data: Robbert van Gorkum, Sophie Peereboom, Alexander Penn and Christian Federau. I appreciated the helpful discussions of IVIM with the latter.

I would also like to thank Kerem Teczan and Valery Vishnevskiy for their help with Bayesian statistics and optimization. In addition, I would also like to thank Sudhir Shankar Raman and Prof. Klaas Enno Stephan from the adjacent TNU group for their help in Bayesian statistics. Furthermore, I am thankful for the overview over Bayesian computation software I was given by Malgorzata Roos from the University’s Biostatistics group.

This thesis would have not been possible without the great atmosphere created by the past and present colleagues of the cardio group inside and outside my office, who had to endure my jokes from time to time: Verena Knobloch, Johannes Schmidt, Claudio Santelli, Christian Stoeck, Lukas Wissmann, Julia Busch, Christian Binter, Constantin von Deuster, Dian Liu, Vlad Ceregan, Patrick Wespi, Andrei Manoliu, Markus Niemann, Martin Genet, Alexander Gotschy, Adrian Huber, Grzegorz Kwiatkowski, Jonas Steinhauser, Kerem Teczan, Zsofia Proehle, Sophie Peereboom, Robbert van Gorkum, Beat Schuler, Christian Günthner, Jonas Walheim, Tobias Hoh, Ezgi Berberoglu, Valery Vishnevskiy, Hannes Dillinger, Julia Trächter, Andreas Dounas, Javier Montoya, Johanna Stimm, Patrick Bosshard and Stefano Buoso.

The atmosphere at the institute would have not been the same without our close colleagues from the hardware and spectroscopy groups. Thanks to all of you for creating such a great atmosphere and for making this wild ride enjoyable both during office hours and beyond.

In terms of technical support, I want to thank Urs Sturzenegger and Roger Luechinger for keeping our scanner infrastructure running and providing all sort of related support and solutions even for short-term requests.

Marianne Berg and Isabell Spiess provided great administrative support, finding effective solutions to ETH regulations. In addition, I owe a special thanks to Anne Theresa Schäfer who helped me greatly with handling budget and administration issues of my European Commission funded project and hence went through regulation & bureaucracy hell together with me. Bruno Willi provided great IT support in terms of both software and hardware. Thanks to Beat for being a great gym buddy, providing insight into both being a high school teacher and the inner workings of the Principality of Liechtenstein.

I especially want to express my sincere gratitude towards the EU and Swiss taxpayer who funded my work. I hope at least some of it can be put to good use.

Outside the office, my friends were there to help me unwind and reminded me that a world outside the academic ivory tower exists. I am very grateful for their friendship, company and fun times.

Finally, I would like to thank my family for their support and frequent encouragement. I owe a great debt of gratitude to Florence for supporting me through this journey with her near infinite patience. This would have not been possible without her.